

**Complementarity of Multiple X-Ray Contrasts in  
Characterization of Pulmonary Fibrosis with Grating  
Interferometer Micro-CT**

A THESIS  
SUBMITTED TO THE FACULTY OF  
MAYO CLINIC  
MAYO CLINIC GRADUATE SCHOOL OF BIOMEDICAL SCIENCES  
MAYO CLINIC COLLEGE OF MEDICINE AND SCIENCE

BY  
BRANDON JOHN NELSON

IN PARTIAL FULFILLMENT OF THE REQUIREMENTS  
FOR THE DEGREE OF  
DOCTOR OF PHILOSOPHY IN BIOMEDICAL SCIENCES –  
BIOMEDICAL ENGINEERING AND PHYSIOLOGY

APRIL 2022

## **Copyright Page**

© Brandon John Nelson, April 2022

# ACKNOWLEDGEMENTS

---

I would like to thank a number of people, whose guidance and support was essential in completing this journey. First and foremost, thank you to my mentor Dr. Cynthia McCollough, who has been integral in my growth. I am grateful for your patience and mentorship over the years. I greatly value the example you set of successful team-based science. In addition, I would also like to thank the other members of my thesis advisory committee – Dr. David Holmes III, Dr. Thomas Koenig, Dr. Shuai Leng, and Dr. Daniel Tschumperlin, who helped guide and support me and this thesis project through many challenges.

To the current and past members of the X-Ray Imaging Core: Andrew Vercnocke, Mahya Sheikhzadeh, Jeff Marsh, and Steve Jorgenson, thank you for your support and comradery in building and debugging TWO phase contrast systems.

Thank you to all of my colleagues at the CT Clinical Innovation Center, past and present, who have always shown genuine enthusiasm for this project and have been a joy to work alongside.

Thank you to Dr. Giovanni Ligresti, Dr. Nunzia Caporarello, Jeff Meridew for your patience and support as we worked out how to best prepare samples for the study.

Thank you to Marcus Zuber, Sabine Bremer, and the other members of the Laboratory for Applications of Synchrotron Radiation (LAS) at the Karlsruhe Institute for Technology for training me on the practical methods of x-ray phase contrast imaging.

Thank you to my past mentors, Dr. Eric Hazlett, Dr. Keir Neumann, and Dr. Teresa Gunn who continue to mentor me to this day.

To my friends and classmates Anders Asp, Matthew Brown, Brian McCollough, and April McPherson as well as my other friends and classmates, older and younger, Alex Weston, Jonathan Calvert, Evan Nicolai, John Strikwerda, and everyone else, thank you all for your friendship and sharing the ride with me.

To my friends and family in Minnesota and Montana, even those that no longer live in Minnesota or Montana, thank you for your patience and always being there for me. Thank you to my parents, you have been my rock. And thank you to my partner, Sarah Castro, who has been there since the beginning.

I could not have done it without you all.

### **Funding**

Funding support was provided by the Mayo Clinic Graduate School of Biomedical Sciences and the 2020 Mayo Clinic Team Science Award with Arizona State University.

# ABSTRACT

---

**Background:** Idiopathic pulmonary fibrosis (IPF) is a chronic interstitial lung disease characterized by a progressive deposition of scar tissue in the lung interstitium and a poor prognosis. It is primarily diagnosed using high resolution computed tomography (HRCT) to identify specific disease patterns and to measure the extent of fibrosis burden. Mouse models of pulmonary fibrosis are used to investigate mechanisms and interventions of IPF, and micro-CT is common tool used to noninvasively assess fibrosis burden in these models. The sensitivity of both clinical CT and micro-CT in the detection and quantitative assessment of fibrosis is limited by partial volume effects. Here, the signal from the small tissue structures of the lung become averaged out with the surrounding air signal. X-ray dark-field is a phase-derived property that derives signal from unresolved structures and thus has been the focus of many studies supporting its use for detecting lung diseases. The translation of dark-field to more animal studies and human-scale trials has been accelerated by Talbot-Lau grating interferometry which enables dark-field measurements with standard large focal spot x-ray sources and large detector pixels. However, when measured with these systems dark-field signal magnitude has been shown to depend upon the system spatial resolution relative to the size of structures in the imaged sample. This limits the quantitative value of dark-field as any changes to an imaging system's spatial resolution could also affect the dark-field signal level. Additionally, the grating structures used to measure dark-field signal can contaminate the image with beam hardening artifacts negatively affecting image quality.

**Purpose:** The goal of this thesis is to develop strategies to address these challenges as they impact the visualization and quantitative assessment of fibrosis in the lungs. This work hypothesizes that x-ray dark-field and attenuation, which can be measured simultaneously with grating interferometry, can be used in a complementary fashion to address these quantitative issues with dark-field. To this end, this thesis was organized into three aims. **Aim 1** was to design, build, and evaluate a grating interferometer micro-CT system for *ex vivo* small animal lung imaging. **Aim 2** was to develop, implement, and evaluate correction strategies to address grating-derived beam hardening artifacts. Finally, **Aim 3** was to

develop methods to leverage complementary attenuation and dark-field image information and evaluate their impact on visualizing and quantifying pulmonary fibrosis.

**Methods:** For **Aim 1** a Talbot-Lau grating interferometer micro-CT imaging system was built along with the necessary preprocessing steps for small animal *ex vivo* lung imaging. For **Aim 2** an algorithm correction strategy that accounts for the spatial heterogeneous beam hardening in the interferometer gratings was developed. The method uses signals from the interferometer to encode the spatial heterogeneity of beam hardening in a polynomial correction. The grating-based beam hardening correction was validated using phantom studies in different materials to quantify the reduction in ring and cupping artifacts associated with the beam hardening. The applicability of the approach to lung imaging was then demonstrated with an *ex vivo* lung sample. For **Aim 3** a technique to combine dark-field and attenuation images is introduced. The task-independent image quality of the proposed method, dark-field enhanced attenuation (DFEA), was evaluated with phantom experiments to assess the impact on spatial resolution and contrast enhancement in different materials. Seven *ex vivo* lung models of pulmonary fibrosis were then imaged with the grating interferometer micro-CT to qualitatively and quantitatively assess the impacts of DFEA on characterizing lung structure and pathology. Pulmonary fibrosis extent was defined as tissue area fraction measured via an automatic histogram-based segmentation technique that finds a threshold to separate tissue pixels from air pixels. The performance of DFEA at the task was evaluated relative to a high-spatial resolution dedicated micro-CT system which was assumed to provide a ground-truth measure of tissue fraction.

**Results:** After developing the grating interferometer micro-CT imaging chain the beam hardening correction scheme for grating interferometry was evaluated. In a water phantom, the correction reduced standard deviation from ring artifacts in attenuation CT images by 57% and in dark-field images by 66%. When applied to images of the lungs ring artifacts were substantially removed. Phantom evaluations of the technique to combine dark-field and attenuation information revealed that DFEA improved spatial resolution in terms of better approximating the modulation transfer function (MTF) response for an ideal edge at all spatial frequencies measured. ROI measurements in a phantom of different attenuation

inserts and non-attenuating inserts with different porosity showed that DFEA maintains quantitative accuracy of attenuation coefficients in large attenuating materials while improving contrast with unresolvable structures. Imaging experiments on the *ex vivo* lung samples revealed that DFEA revealed improved definition of small airways and micro-honeycombing in fibrotic loci compared to when viewed with attenuation or dark-field alone. Compared to the attenuation series, DFEA yielded improved estimates of tissue area fractions relative to the dedicated high-resolution micro-CT used as a reference standard.

**Conclusions:** The results presented in this thesis support the hypothesis that x-ray dark-field and attenuation can be used together to improve spatial resolution while maintaining the quantitative value of attenuation coefficients. Techniques to combine these contrasts were presented along with correction strategies to reduce artifacts from the gratings.

# TABLE OF CONTENTS

---

ACKNOWLEDGEMENTS .....	i
ABSTRACT .....	iii
TABLE OF CONTENTS .....	vi
TABLES .....	ix
FIGURES .....	x
Chapter 1 .....	1
1.1 Motivation .....	1
1.2 Research Hypothesis and Specific Aims .....	8
1.3 Overview of Dissertation .....	9
Chapter 2 .....	11
2.1 Introduction .....	11
2.2 X-Rays and Physical Contrast Mechanisms .....	13
2.2.1 X-Ray Wave Propagation Through Matter .....	14
2.2.2 Material Properties Influencing X-Ray Contrast .....	16
2.3 Measuring X-Ray Phase Properties .....	19
2.3.1 Talbot-Lau Grating Interferometry .....	19
2.3.2 Multi-Contrast Signal Retrieval .....	22
2.4 Computed Tomography of X-Ray Contrasts .....	25
2.5 Practical Considerations in X-Ray CT Measurements .....	26
2.5.1 Beam Hardening .....	26
2.5.2 Spatial Resolution .....	27
2.6 Dark-Field from Intra-Pixel Phase Gradients .....	29
2.7 Previous Works on Complementarity of X-Ray Contrasts .....	30
2.8 Conclusions .....	31
Chapter 3 .....	32
3.1 Introduction .....	32
3.2 System Description .....	33
3.2.1 System Geometry .....	34
3.2.2 Talbot-Lau Grating Interferometer Components .....	35
3.3 Data Collection .....	37
3.4 Data Calibration and Preprocessing .....	42
3.5 Image Reconstruction .....	44
3.6 Conclusions .....	48
Chapter 4 .....	49
4.1 Introduction .....	49
4.2 Methods .....	52
4.2.1 EBHC-GI .....	52
4.2.2 Determining the System Spatial Heterogeneity Term $Mk$ .....	54
4.2.3 Sample Preparation .....	57
4.2.4 Data Acquisition and Image Reconstruction .....	58
4.2.5 Evaluation of EBHCI-GI .....	59

4.3	Results .....	59
4.3.1	Determining the System Spatial Heterogeneity Term <i>Mk</i> .....	59
4.3.2	Evaluation of EBHC-GI in Water .....	60
4.3.3	Evaluation in Higher Atomic Number Materials .....	64
4.3.4	Lung Imaging Application .....	67
4.4	Discussion .....	69
4.5	Conclusions .....	71
4.6	Accomplishments .....	72
Chapter 5	.....	73
5.1	Introduction .....	73
5.2	Dark-Field Enhanced Attenuation and Phase: General Approach .....	74
5.3	Influence on Spatial Resolution .....	76
5.3.1	Methods .....	76
5.3.2	Results .....	76
5.4	Influence on Contrast with Unresolved Structures .....	79
5.4.1	Methods .....	81
5.4.2	Results .....	82
5.5	Qualitative Evaluation of DFEA on Lung Imaging .....	84
5.5.1	Methods .....	84
5.5.2	Results .....	85
5.6	Discussion .....	88
5.7	Conclusions .....	89
5.8	Accomplishments .....	89
5.8.1	Conference Presentations .....	89
5.8.2	Conference Proceedings .....	90
Chapter 6	.....	91
6.1	Introduction .....	91
6.2	Methods and Materials .....	92
6.2.1	Dark-Field Enhanced Attenuation .....	92
6.2.2	Sample Preparation .....	92
6.2.3	Image Acquisition .....	92
6.2.4	Fibrosis Quantification and Performance Evaluation .....	93
6.3	Results .....	95
6.4	Discussion .....	101
6.5	Conclusions .....	102
6.6	Accomplishments .....	102
Chapter 7	.....	104
7.1	Summary of Research .....	104
7.2	Future Research Directions .....	106
7.3	Conclusions .....	107
7.4	Accomplishments .....	108
7.4.1	Peer-Reviewed Journal Papers .....	108
7.4.2	Conference Proceedings .....	109
7.4.3	Conference Abstracts .....	109
References	.....	110



## TABLES

---

<b>Table 2.1</b> Reference values of the real and imaginary components of the complex index of refraction. Values available at <a href="https://henke.lbl.gov/optical_constants/pert_form.html">https://henke.lbl.gov/optical_constants/pert_form.html</a> ..	18
<b>Table 3.1</b> Grating specifications.....	37
<b>Table 4.1</b> Beam hardening correction results for water quantified in terms of mean squared error (MSE) from template $t$ and standard deviation (Std dev) within the homogenous water region. ....	64
<b>Table 4.2</b> Beam hardening correction results for silicon quantified in terms of MSE from the template and standard deviation of values within the homogenous silicon region.....	67
Table 6.1 Summary of Bland-Altman results plotted in Figure 6.4. The agreement ratio is defined as the measured tissue area fraction divided by the reference measurement and the 95% limits of agreement correspond to 1.96 times the standard deviation of the agreement ratios from the measured patches.....	100

## FIGURES

---

**Figure 1.1** An overview of the characteristic features of idiopathic pulmonary fibrosis (IPF). The disease is characterized by a buildup of scarring fibrosis increasing the thickness of the interstitium, the structure supporting the network of alveoli and blood vessels, resulting in less efficient gas exchange. Top center: lung diagram featuring a healthy right lung and diseased left lung with idiopathic pulmonary fibrosis. Dashed-line regions of interest focus on a healthy and diseased terminal bronchiole. Compared to the healthy terminal bronchiole, the interstitium surrounding the diseased bronchiole is innervated with fibrocyte cells depositing extracellular matrix stiffening and eventually restructuring the interstitium. This fibrosis stretches open bronchi, leaving them dilated and affecting airflow. The functional impact on gas exchange is demonstrated in a region of interest now from within the terminal bronchiole, focusing on a single alveolar wall where air and blood interface at a thin wall of interstitium. In the diseased bronchiole the scarring increases the thickness of this wall, increasing diffusion distance and reducing the gas exchange rate. Figure adapted from Martinez et al.<sup>4</sup>. ..... 2

**Figure 1.2** High resolution CT images from two patients with IPF symptoms. While images from the upper lung zones in the first patient are free of disease patterns (a), the lower zones show peripheral honeycombing (b, c) confirming the UIP pattern and IPF diagnosis. For the second patient, images of the upper lung zone (d) and lower zone (e, f) reveal dense reticulation in the lower zone, but not clear honeycombing which is necessary to confirm a diagnosis. A biopsy from the lower zone revealed that the dense reticulation was micro-honeycombing, resulting in an IPF diagnosis. Confirming the presence of honeycombing is important as it is a key indicator of irreversible architectural remodeling of the lung. On the contrary, reticulation could be the result of reversible processes such as inflammation or fluid retention in the interstitium and thus has different prognoses and treatment plans. Adapted from Martinez et al.<sup>4</sup>. ..... 3

**Figure 1.3** Example of honeycomb disease pattern revealed in pathology of a lung biopsy. (a) Normal lung anatomy at 10x magnification on pathology microscope shows small airways, alveolar duct, and alveoli. (b) Pathology slide used to confirm IPF diagnoses, acquired at the same magnification, reveals micro-honeycombing, an irreversible remodeling of the lung architecture following advanced fibrosis. Arrow points to an air containing cyst surrounded by remodeled interstitial walls. Adapted from Martinez et al.<sup>4</sup>. ..... 4

**Figure 1.4** Images from a prototype human scale dark-field chest radiograph system, adapted from Willer et al.<sup>34</sup> Conventional x-ray attenuation measurements derive signal from material composition, primarily density and atomic number. Thus, the lungs are largely dark outside of the heart, vessels, and airway walls. In contrast, dark-field is sensitive to small structures and the many repeating microscopic alveoli and airway structures generate bright signal, whereas the larger heart, and blood vessels yield less signal. .... 7

**Figure 2.1** Medical x-rays have a broad spectrum of energies. The smooth portion of the spectrum is generated via Bremsstrahlung, while peaks in the spectrum at higher energies are from characteristic emission. The maximum energy of the spectrum is determined by

the electric potential field, in kV, applied to the x-ray source. Spectrum simulated with Spektr 3.0.<sup>49</sup> ..... 13

**Figure 2.2** Diagram of x-ray plane waves propagating in the positive  $y$  spatial direction through materials with different complex indices of refraction  $n = 1 - \delta + i\beta$ . The topmost waveform propagates through free space ( $\beta = \delta = 0$ ), the uppermost object is made of material with only absorption properties ( $\beta > 0, \delta = 0$ ). The middle object has only phase shifting properties ( $\beta = 0, \delta > 0$ ). Finally, the bottom material contains both properties ( $\beta > 0, \delta > 0$ ). The dotted line before the objects signifies constant phase across the plane wave before interacting with the objects. Wave fronts passing through phase objects travel with a different phase velocity and accrue a phase difference  $\Delta\Phi$ , while wavefronts passing through absorbing materials lose amplitude. The refracted angle  $\alpha$  between the original wavefront and the phase shifted wavefront is illustrated as the angle between their phase fronts. .... 15

**Figure 2.3** Top-down view diagram of a Talbot-Lau grating interferometer. X-rays are represented by arrows pointing normal to their wave front. Following the x-ray path from the source,  $G0$  spatially filters the incoherent x-rays yielding a coherent plane wave. From this plane wave  $G1$  produces a downstream interference pattern. While passing through a pure phase wedge, the wavefront travels at a different phase velocity. In the slanting region of the wedge ( $\partial\Phi/\partial x > 0$ ) refraction changes the propagating direction of the wavefront by angle  $\alpha$ , which then laterally shifts the interference pattern introducing a phase shift  $\phi$  in the measured phase stepping curve (shown as red sinusoid curve). Following phase retrieval, the differential phase in the pixel behind the wedge slant (pixel B) is recovered, while adjacent pixels (A and C) report no differential phase shift. .... 21

**Figure 2.4** Phase stepping diagram showing the measured x-ray intensity at a single pixel as a function of the lateral translation of  $G2$  in the  $x$  direction. Depending on the size of the detector pixel the above curves could be the averaged signal of a few or many adjacent periods (fringes) of the interference pattern measured ideally at the same phase with each acquisition. The solid gray phase step curve (PSC) shows the reference interference pattern with no object in the beam line. By adding an object to the beam line this PSC can undergo a change in offset of  $\Delta a0 = a0, r - a0, s$ , a phase shift of  $\Delta\phi = \phi r - \phi s$ , or a change in amplitude of  $\Delta a1 = a1, s/a1, r$ . .... 23

**Figure 2.5** Phase step diagram demonstrating x-ray dark-field resulting from small-angle x-ray scattering where scatter in an equiangular cone yields equal and opposite phase shifts (demonstrated as blue and red constituent curves  $\Delta\Phi = \pm\pi/5$ ) which interfere reducing the amplitude of the interference pattern before the analyzer grating  $G2$ ..... 25

**Figure 2.6** X-ray dark-field from intra-pixel phase gradients. (a) grating interferometer with a uniform phase object  $\Phi$  with two gradient edges generating a positive phase shift in the interference pattern (blue) and negative phase shift (red). At right of the analyzer grating  $G2$  are the retrieved differential phase and dark-field signals following phase stepping (curves shown in panel (b)) using two different detector configurations, Det. 1 and 2. The first detector features small pixels A, B, and C able to resolve the two gradient edges as positive and negative differential phase impulses  $\pm\Delta\phi$  and zero dark-field (visibility = 1) behind measured behind the gradient edges. The second detector configuration features large pixels D, larger than A, B, and C combined. The larger pixel

D averages the local shifts in the interference pattern caused by the two gradients yielding no measure phase shift but a positive dark-field signal due to a loss in visibility (Eq. 2.15). (b) These retrieved differential phase and dark-field signals can be understood by their measured phase step curves as measured by small pixels A, B, and C from Det. 1 and the large pixel D from Det. 2. Small pixels A and C from Det. 1 located directly behind the gradients in (a) can resolve the positive and negative phase shifts ( $+\Delta\phi$ ,  $-\Delta\phi$ ). However, the large pixel D from Det. 2 in (a) covers both gradients, averaging the gradients and yielding a reduced visibility and thus positive dark-field signal. .... 30

**Figure 3.1** Schematic overview of the Talbot-Lau grating interferometer micro-CT system. The source grating  $G_0$  spatially modulates x rays from a source with a large focal spot.  $G_1$  produces a downstream Talbot carpet sensitive to phase shifts induced by an object in the beam path.  $G_2$  matches the period of the Talbot interference pattern at the detector plane, enabling sampling of the high frequency interference pattern with large detector apertures that can cover several periods of  $G_2$ . A rotating object stage enables tomographic acquisitions by acquiring multi-contrast data at multiple view angles. .... 33

**Figure 3.2** Talbot-Lau grating interferometer micro-CT system photograph with labelled annotations. .... 34

**Figure 3.3** Radiographic geometry of Talbot-Lau grating interferometer system drawn to scale..... 35

**Figure 3.4** Interferometer gratings.  $G_0$  and  $G_1$  are shown in grayscale scanning electron micrograph images.  $G_2$  is displayed in color as visible-light microscope image. .... 37

**Figure 3.5** Experimental phase stepping curve images of an acrylic cylinder with a wooden dowel insert and air-filled inserts. Left: Even numbered reference and object phase stepping acquisition images. Three ROIs A-C cover different regions with different x-ray interaction properties with their measured intensities plotted as a function of  $G_2$  translation distance at right. The ROI frame color matches the respective measurement on the plotted PSC. 39

Figure 3.6 Retrieved contrasts from an x-ray grating interferometer of a cylindrical acrylic phantom with hollow inserts. Left: Attenuation projection. Arrows indicate a wooden insert and air in the empty phantom chambers. Center: differential phase projection. Right: dark-field projection. .... 41

**Figure 3.7** Example visibility map acquired from the experimental Talbot-lau grating interferometer. Grating quality, grating alignment, and acquisition parameters all influence the visibility map..... 42

**Figure 3.8** Measured detector decay recorded immediately after turning off the x-ray source. The decay is modeled as two-part exponential with the line best fit plotted. .... 44

**Figure 3.9** Effect of scintillator decay on CT noise texture. .... 44

**Figure 3.10** Sinogram acquisition of three contrasts over  $\pi$  radian rotation..... 45

**Figure 3.11** Three contrast reconstructions from grating interferometer micro-CT of a cylindrical acrylic phantom with hollow inserts. **Left:** attenuation contrast image. Arrows indicate wooden insert (top row) and air contained in hollow portions of the phantom. **Center:** phase contrast image. **Right:** dark-field images. .... 46

<b>Figure 3.12</b> Line profiles from three x-ray contrast reconstructions covering a wood insert and hollow inserts in an acrylic phantom. <b>Top:</b> attenuation profile. <b>Middle:</b> phase profile. <b>Bottom:</b> dark-field profile. Arrows indicate signal response from different materials in the phantom.....	48
<b>Figure 4.1</b> (a) Projections of attenuation signal through a water-filled tube in the highlighted region of interest, acquired both without and with gratings. (b) Line profiles through both images.....	51
<b>Figure 4.2</b> Reference Fourier coefficient images serve as grating images to show underlying grating structure viewed in all three contrasts.....	55
<b>Figure 4.3</b> Overview of processing steps involved in EBHC-GI. Three contrast calibration projections $qk$ retrieved from phase stepping curves acquired of a calibration object with a known homogenous region are used to fit correction coefficients for each contrast $ck$ that are used to correct future projections of similar materials.....	57
<b>Figure 4.4</b> Imaged samples shown to scale include (a) 1.5 mL snap tube filled with water, (b) QRM micro-CT bar pattern phantom schematic <sup>87</sup> . The inset shows an enlarged view of the chip and the edge-on orientation used to acquire images. The lower 400 $\mu\text{m}$ silicon region was used exclusively in this study. (c) Posterior view of excised mouse lung with heart following fixation and air drying at end-exhalation inflated volume. ....	58
<b>Figure 4.5</b> Pearson correlation coefficient magnitudes $ r $ between sample and air grating projections for both the water and silicon samples. *indicates $P < 0.05$ . ....	60
<b>Figure 4.6</b> Uncorrected reconstructions and artifact-free templates of the water sample for attenuation $A$ , phase $\phi$ , and dark-field $D$ contrasts.....	62
<b>Figure 4.7</b> Water sample reconstructions for each contrast with the original uncorrected axial image (a) shown left of the EBHC-GI corrected slice (b). The image display settings for each contrast are determined from the uncorrected image with a level equal to the image mean and window width of four standard deviations. (c) Line profiles that correspond to the columns of pixels marked in red in (a) and (b) compare original (dashed gray), corrected (solid black), and template (dotted red) line profiles. ....	63
<b>Figure 4.8</b> Silicon tile reconstructions of attenuation, phase, and dark-field contrasts. Uncorrected images (a) are shown to the left of EBHC-GI corrected slices (b). The image display settings for each contrast are determined from the uncorrected image with a level equal to the image mean and window width of four standard deviations. (c) Line profiles that correspond to the columns of pixels marked in red in (a) and (b) compare original (dashed gray), corrected (solid black), and template (dotted red) line profiles. ....	66
<b>Figure 4.9</b> Axial mouse lung reconstructions in prone position show the heart, large airways, and lung parenchyma. Attenuation, phase, and dark-field contrast images are shown both before and after corrections along with a difference image. The display settings are set equal for both corrected and uncorrected sets. ....	68
<b>Figure 5.1</b> Synergistic use of dark-field with attenuation and phase contrast images of a cylindrical solid water phantom. From left to right, dark-field, phase, dark-field enhanced phase (DFEP), attenuation, dark-field enhanced attenuation (DFEA). ....	77

Figure 5.2 Dark-field recovers high spatial frequencies. Left: radially averaged edge spread function profiles from attenuation images of the water cylinder. Right: profiles from the phase images of the water cylinder. Arrows indicate restoration of edge relative to the true profile.....	77
Figure 5.3 Modulation transfer function comparisons between attenuation, phase, and dark-field enhanced phase and attenuation profiles. ....	78
<b>Figure 5.4</b> Using enhancement factor $\alpha$ for variable edge enhancement. <b>Left:</b> Measured MTF curves from attenuation ( $\alpha = 0$ ), and DFEA with increasing enhancement factor $\alpha$ . <b>Right:</b> Bar chart plotting spatial frequencies, reported as line pairs per mm (lp/mm) at which different contrast levels are maintained, corresponding to 50%, 30%, and 10% MTF for attenuation and DFEA $\alpha$ for different values of $\alpha$ .....	79
<b>Figure 5.5</b> Four distinct regions sampled by a CT system with PSF approximated by its pixel size yield a uniform attenuation measurement but can be distinguished by dark-field due to the difference in number of unresolved gradients. In the ground truth row white represents tissue and blacks represents air space in this contrived model of lung. In the attenuation and dark-field rows greater signal is represented in white and null signal by black according to the color bar at left.....	81
<b>Figure 5.6</b> Influence of dark-field contribution ( $\alpha$ ) in materials of different x-ray attenuation and porosity. <b>(a)</b> Phantom with six inserts. Top row shows different attenuating materials while the bottom row shows non-attenuating materials with different porosity. At left is the attenuation image with the dark-field image at right. The middle columns show DFEA images for different values of $\alpha$ . <b>(b)</b> Signal and noise measured in circular regions of interest covering each of the inserts for all six materials for increasing values of $\alpha$ in DFEA. ....	83
<b>Figure 5.7</b> Bleomycin mouse model of idiopathic pulmonary fibrosis. <b>(a)</b> Summary of the bleomycin mouse model of pulmonary fibrosis where bleomycin is administered via the trachea and incubated for 21 days before lung extraction and fixation. <b>(b)</b> Comparison of different routes of fixative administration lung structures shown in ex-vivo micro-CT compared to in-vivo micro-CT. <b>(c)</b> External view of fixed inflated lungs using the instillation method. ....	85
<b>Figure 5.8</b> Comparison of attenuation, dark-field, and dark-field enhanced attenuation (DFEA) projections. Large attenuating structures like the heart (*), esophagus (#), large blood vessels, and fibrosis accumulations around the radiolucent bronchi (arrows) appear bright in the attenuation image and null in the dark-field image.....	86
<b>Figure 5.9</b> Comparison of lung CT cross-sections with DFEA. <b>Left:</b> Attenuation axial CT image cropped around a peribronchial fibrotic lesion. Other relevant anatomy present are the esophagus (#) and major bronchi (orange arrow). <b>Center:</b> Dark-field axial image of the same region. <b>Right:</b> dark-field enhanced attenuation (DFEA) image shown at the same display settings as the original attenuation image at left. Note the absence of streak artifact in the DFEA image, which is present in both the attenuation and dark-field image because it was present in the raw phase step data. ....	87
<b>Figure 5.10</b> Impact of interferometer gratings in lung imaging.....	88

**Figure 6.1** Comparison between attenuation, dark-field, and dark-field enhanced attenuation (DFEA) lung images from a bleomycin mouse model of pulmonary fibrosis. **(a)** Original interferometer attenuation image. Examples of specific anatomy include the esophagus (#), blood vessels (orange arrowhead), and major bronchus (orange arrow). **(b)** original interferometer dark-field image. **(c)** dark-field enhanced attenuation image (DFEA) where the dark-field image (b) is subtracted from the attenuation image (a) after first being scaled by factor  $\alpha = 0.022$ , the measured ratio of water attenuation and phase coefficients. **(d)** increasing this scalar value to  $\alpha = 0.1$  results in a further edge-enhancing effect and further parenchyma contrast enhancement. Image subsets a), c), and d) are all shown at the same display settings of min/max:  $0/0.03 \text{ mm}^{-1}$ , while the dark-field image is shown with display setting min/max:  $-0.1/0.1 \text{ mm}^{-1}$ ..... 96

**Figure 6.2** Histogram comparison of attenuation and dark-field enhanced attenuation (DFEA) against a  $5 \mu\text{m}$  voxel high-resolution “Reference” micro-CT scan. Arrow annotations identify the locations of the air and tissue peaks in the bimodal distribution. .... 97

**Figure 6.3** Comparison of intensity-based threshold segmentation between attenuation (left) and dark-field enhanced attenuation (center) against co-registered reference  $5 \mu\text{m}$  voxel micro-CT (right). **Top:** Representative image patches of all three images are shown at the same display settings, min/max:  $0/0.03 \text{ mm}^{-1}$ . In this patch reticular fibrosis and honeycombing is present around the large airways. **Bottom:** Threshold-based intensity segmentations with thresholds determined automatically via minimum error thresholding applied to the whole volume histogram. Exclusion mask shown in red. .... 98

**Figure 6.4** Bland-Altman plot of tissue area fractions measured on a low resolution  $60 \mu\text{m}$  voxel grating interferometer CT system compared to an approximate ground truth high resolution  $5 \mu\text{m}$  voxel reference micro-CT. The contribution of dark-field enhanced attenuation (DFEA) with greater contribution of dark-field information to improve segmentation accuracy in terms of closeness to the reference scan is shown. The thick dashed black line shows an ideal measurement with no bias from the reference measure for an agreement ratio of 1. Red and blue solid lines correspond to the mean agreement ratios, while the corresponding thin dashed lines are the 95% limits of agreement calculated as  $\pm 1.96$  times the standard deviation of the ratios<sup>117</sup>. .... 100

# CHAPTER 1

---

## Thesis Introduction

### 1.1 Motivation

Idiopathic pulmonary fibrosis (IPF) is a chronic interstitial lung disease characterized by a progressive deposition of scar tissue in the lung interstitium, the support structure of the alveoli and blood vessels, which when thickened reduces gas exchange and breathing function (**Figure 1.1**).<sup>1</sup> IPF presents in patients as cough and breathlessness and a dramatic reduction in quality of life. Prognosis is highly variable with survival time ranging from months to decades and a median survival of 2-3 years<sup>2</sup>. Prevalence increases with age and is more common in males. Current estimates suggest 3 million people are affected worldwide though this number is likely an underestimate as many instances are undercounted due to strict diagnostic requirements<sup>3</sup>.

Diagnosis of IPF is done with high-resolution computed tomography (HRCT) to identify the characteristic usual interstitial pneumonia (UIP) pattern and exclude other potential sources of disease. However, inconclusive imaging findings can delay or miss a diagnosis. As a result there is a median delay of 2.2 years from symptom onset to confirmed IPF diagnosis<sup>2</sup>. There is a critical need, therefore, to develop imaging technologies to identify IPF early and definitively to facilitate earlier and more effective treatment, slowing progression and better preserving lung function.

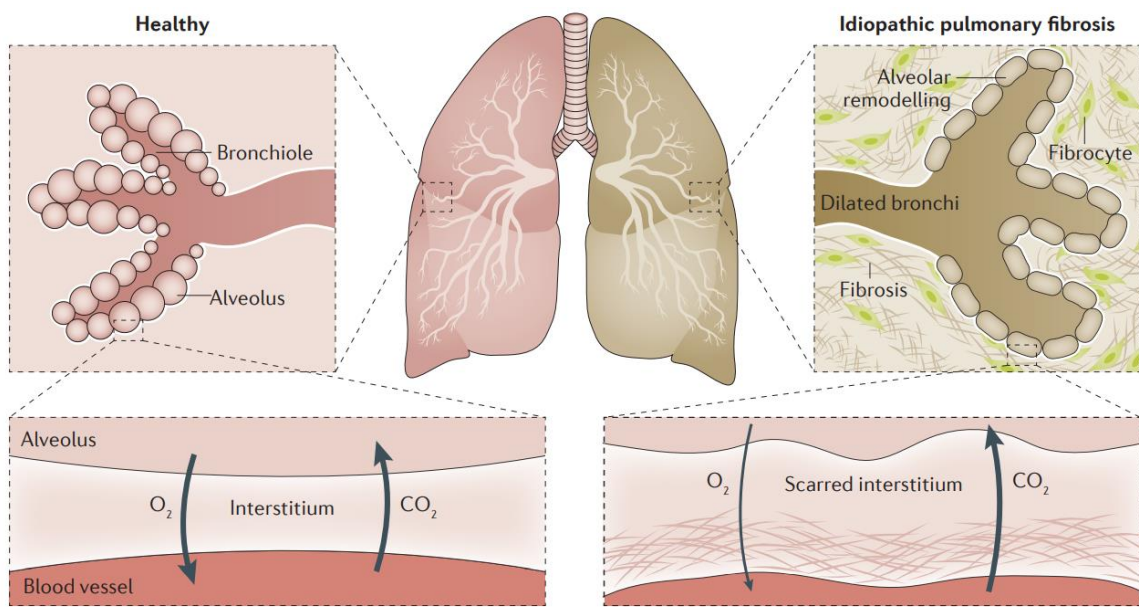


**Figure 1.1** An overview of the characteristic features of idiopathic pulmonary fibrosis (IPF). The disease is characterized by a buildup of scarring fibrosis increasing the thickness of the interstitium, the structure supporting the network of alveoli and blood vessels, resulting in less efficient gas exchange. Top center: lung diagram featuring a healthy right lung and diseased left lung with idiopathic pulmonary fibrosis. Dashed-line regions of interest focus on a healthy and diseased terminal bronchiole. Compared to the healthy terminal bronchiole, the interstitium surrounding the diseased bronchiole is innervated with fibrocyte cells depositing extracellular matrix stiffening and eventually restructuring the interstitium. This fibrosis stretches open bronchi, leaving them dilated and affecting airflow. The functional impact on gas exchange is demonstrated in a region of interest now from within the terminal bronchiole, focusing on a single alveolar wall where air and blood interface at a thin wall of interstitium. In the diseased bronchiole the scarring increases the thickness of this wall, increasing diffusion distance and reducing the gas exchange rate. Figure adapted from Martinez et al.<sup>4</sup>.

Confident identification of the UIP pattern presents a major challenge in early IPF diagnosis. UIP is a structural disease pattern consisting of a predominantly bilateral, peripheral, and basal distribution of reticular fibrosis resulting in traction bronchiectasis and honeycombing in more advanced stages (**Figure 1.2**)<sup>5</sup>. If not fully developed, the UIP disease pattern is indistinguishable in CT from other patterns, such as nonspecific interstitial pneumonia which has a different treatment plan and much improved prognosis. Specifically, if there is no clear sign of honeycombing, diagnostic accuracy drops substantially<sup>1</sup>, as does inter- and intra- observer agreement<sup>6,7</sup>. This is exemplified by the two patients in **Figure 1.2**, both presenting with breathlessness and other symptoms of IPF. In the top row, views of the base of the lung reveal characteristic honeycombing confirming UIP and the IPF diagnosis. However, for the patient shown in the bottom row, the pattern

could not be clearly identified as dense reticulation or honeycombing and a surgical biopsy of the region was required to confirm IPF<sup>4</sup>. Despite the reduced use of lung biopsies since the introduction of HRCT, they continue to be used when HRCT findings are equivocal, even though they come with substantial risk of complications and a wide range of in-hospital mortality of 1.2 - 16%<sup>8</sup>. As the desired outcome of lung biopsy is to confirm the presence of honeycombing structures not resolvable in HRCT (**Figure 1.3**), the ability to detect these small structures in a noninvasive way would benefit IPF patients both with earlier diagnoses and less reliance on biopsy.

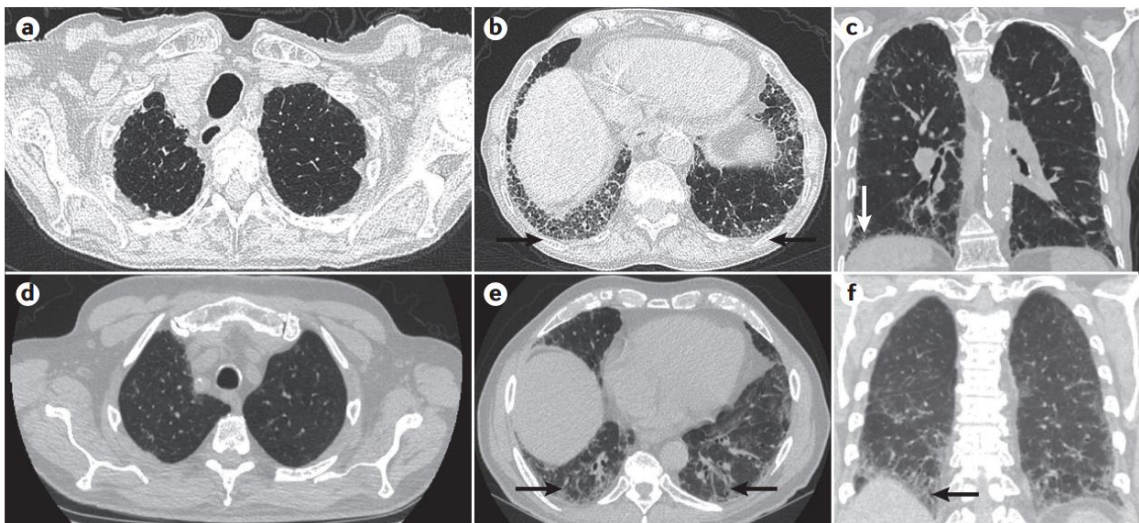


**Figure 1.2** High resolution CT images from two patients with IPF symptoms. While images from the upper lung zones in the first patient are free of disease patterns (**a**), the lower zones show peripheral honeycombing (**b, c**) confirming the UIP pattern and IPF diagnosis. For the second patient, images of the upper lung zone (**d**) and lower zone (**e, f**) reveal dense reticulation in the lower zone, but not clear honeycombing which is necessary to confirm a diagnosis. A biopsy from the lower zone revealed that the dense reticulation was micro-honeycombing, resulting in an IPF diagnosis. Confirming the presence of honeycombing is important as it is a key indicator of irreversible architectural remodeling of the lung. On the contrary, reticulation could be the result of reversible processes such as inflammation or fluid retention in the interstitium and thus has different prognoses and treatment plans. Adapted from Martinez et al.<sup>4</sup>

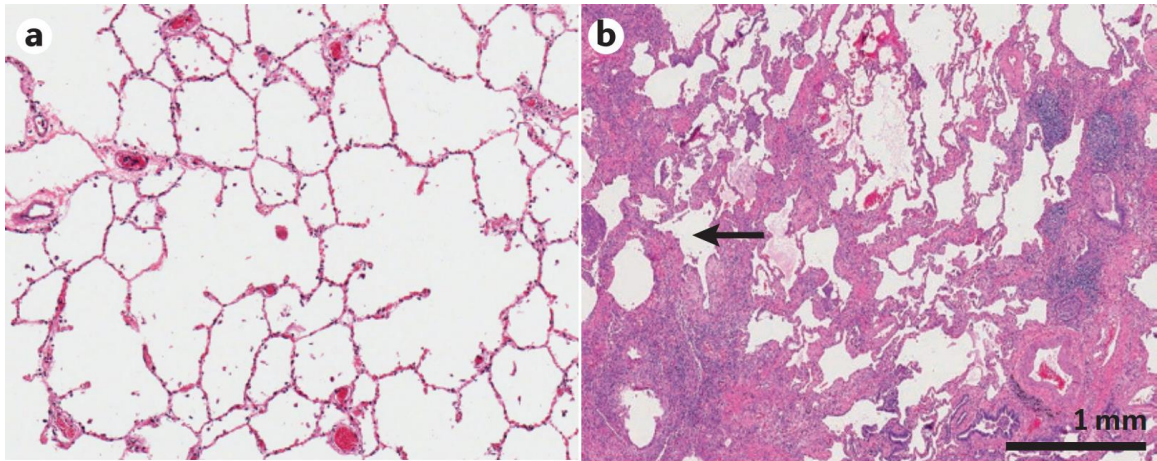


**Figure 1.3** Example of honeycomb disease pattern revealed in pathology of a lung biopsy. **(a)** Normal lung anatomy at 10x magnification on pathology microscope shows small airways, alveolar duct, and alveoli. **(b)** Pathology slide used to confirm IPF diagnoses, acquired at the same magnification, reveals micro-honeycombing, an irreversible remodeling of the lung architecture following advanced fibrosis. Arrow points to an air containing cyst surrounded by remodeled interstitial walls. Adapted from Martinez et al.<sup>4</sup>

Current approaches to earlier and more confident diagnoses of IPF focus on trying to enhance the current “gold standard” of HRCT pattern recognition with more information related to the underlying morphology and function. One solution is the multidisciplinary clinical team approach, where radiologists, pulmonologists, geneticists, and other clinicians work together to augment equivocal HRCT findings with pulmonary function tests and other patient history indicative of IPF, such as age, gender, and genetic background. When integrated in a collaborative effort, this approach has been shown to improve the accuracy and confidence of IPF diagnoses<sup>9</sup>. Weaknesses of this approach include a lack of standardization of diagnostic criteria and lack of availability of such teams at select institutions. Even if more widely adopted, such team-based approaches would all benefit from imaging improvements.

Computer-aided detection algorithms are another approach still that aims to improve existing HRCT diagnostic accuracy and timeliness with automated quantitative measurements of current disease patterns to address issues of reader variability<sup>7,10,11</sup>. Other efforts include identifying new disease patterns and imaging biomarkers based on HRCT data rather than relying on classical patterns derived from histology<sup>1,12</sup>. However, like the clinical team-based approach, these developments in disease pattern identification would

also benefit from more informative image inputs. Photon counting detector CT systems are promising in this regard as they enable HRCT exams with isotropic spatial resolutions as small as 0.2 mm, and are able to resolve the 7-9th generation of airway branches<sup>13</sup>, with early results suggesting improved diagnostic performance in differentiating interstitial lung diseases<sup>14</sup>. Despite this improvement in detector spatial resolution, small airways branch up to 23 generations in humans<sup>15</sup>, which require micron-scale resolution to resolve<sup>16</sup>. However, further improvements in spatial resolution in clinical CT imaging are difficult to achieve. For example, improved resolution is limited by source focal spot size, which must be kept large enough to support high x-ray fluence rates for shorter scan times. This suggests the need for indirect measures, which can be achieved with existing sources and detectors that are more sensitive to changes associated with lung pathology.

To address these spatial resolution limitations, investigations into alternative x-ray interactions have been shown to be more sensitive to small scale structural changes. Advancements in x-ray optics fabrication has enabled measurements of x-ray phase - a wave property of light - at medical x-ray energies and fields of view<sup>17</sup>. Notably, x-ray dark-field is a phase-derived image contrast mechanism shown to generate strong signals in porous materials<sup>18</sup>. Dark-field has been shown to be sensitive to changes in structures orders of magnitude smaller than can be resolved with traditional x-ray attenuation, even using the same source and detectors<sup>19</sup>.

To increase the rate of development many innovations in radiography and CT technology begin in smaller scale micro-CT systems which function as experimental test beds to lay the groundwork for new hardware, acquisition methods, or applications before being translated to full scale systems. Micro-CT systems are also used in biomedical research for both two-dimensional (2D) radiographic as well as quantitative, nondestructive, 3D volumetric assessment of biological specimens ranging from organs to whole small animals.<sup>20</sup> In the study of interstitial lung diseases such as IPF micro-CT is a prevalent tool for both *in vivo* longitudinal monitoring of fibrosis burden as well as *ex vivo* high-resolution structural analysis.

Like clinical CT, spatial resolution in *in vivo* micro-CT is restricted by dose limitations in addition to scan time limits due to the reduced x-ray flux in the smaller sources used. The introduction of respiratory gating minimizes motion blur around the diaphragm, improving spatial resolution and improving sensitivity to small scale changes<sup>21</sup>. In assessing fibrosis burden in the lungs, this has the effect of narrowing the diagnostic window, the minimum resolvable change in fibrosis burden that can be observed over time.

*Ex vivo* scanning removes scan time and dose restrictions and substantially improves sensitivity to fibrosis. Access to 3D volumetric information from the whole lung yields improved sensitivity and reduced bias at estimating fibrosis burden compared to traditional destructive measures including histology and biochemical collagen assays<sup>22</sup>. However, *ex vivo* specimen scanning comes at the cost of a reduced field of view where only a single or partial organ can be imaged at once, often requiring multiple concatenated scans for larger specimens. Furthermore, to maintain sample stability and preserve natural x-ray contrast, lung samples must be fixed and inflated prior to imaging.

For micro-CT imaging, x-ray dark-field presents an opportunity to image micro-structural information in lower resolution *in vivo* scans previously only accessible via high-resolution *ex vivo* specimen scans. Using custom built *in vivo* micro-CT systems, preliminary investigations of dark-field radiography in small animal disease models have shown it to be more sensitive than absorption radiography in detecting several lung pathologies, including emphysema<sup>23-25</sup>, inflammation<sup>26</sup>, pneumothorax<sup>27</sup>, lung cancer<sup>28</sup>, and fibrosis<sup>29</sup>. Other prototype systems have begun to emerge investigating the potential of dark-field CT<sup>30-33</sup>. These early results in animals with micro-CT motivated the development of human scale radiography systems (**Figure 1.4**)<sup>34,35</sup> and full-scale dark-field CT systems built on top of existing rotating gantry CT scanner platforms<sup>36</sup>.

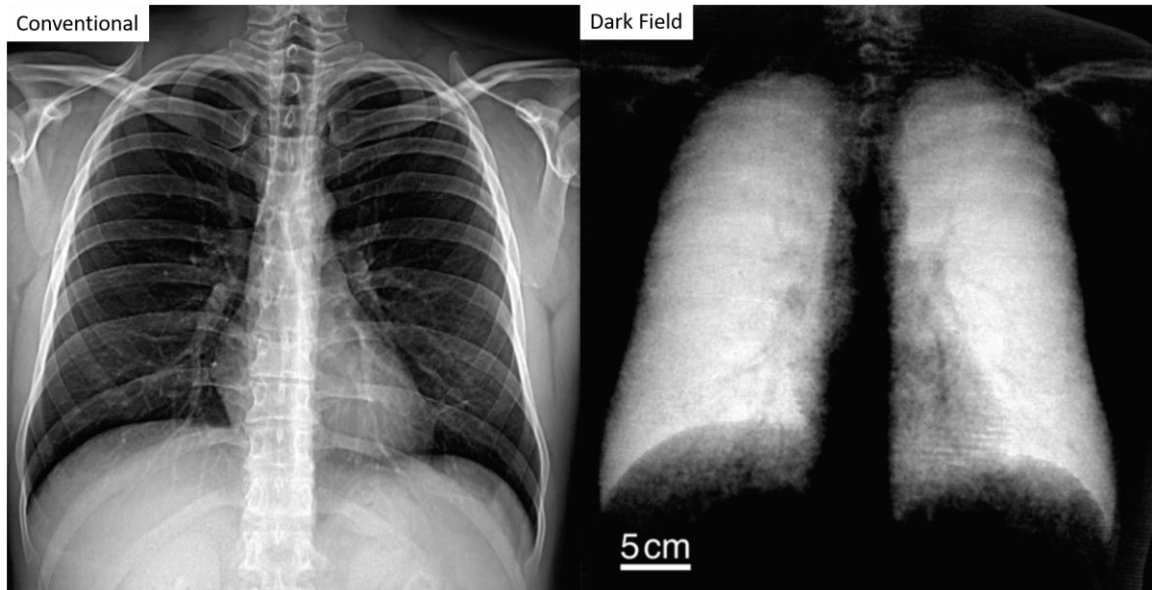


**Figure 1.4** Images from a prototype human scale dark-field chest radiograph system, adapted from Willer et al.<sup>34</sup> Conventional x-ray attenuation measurements derive signal from material composition, primarily density and atomic number. Thus, the lungs are largely dark outside of the heart, vessels, and airway walls. In contrast, dark-field is sensitive to small structures and the many repeating microscopic alveoli and airway structures generate bright signal, whereas the larger heart, and blood vessels yield less signal.

Despite these preliminary successes, many challenges remain in x-ray dark-field lung imaging in both small-scale laboratory and full-scale clinical environments. While originally introduced as being sensitive to x-ray small-angle-scattering<sup>18</sup>, a physical property of material size and composition<sup>37</sup>, further investigations found that dark-field signal is also generated from other sources such as beam hardening<sup>38-40</sup> and sharp edges<sup>41</sup>. This led to a refinement in the current understanding of dark-field measurements in laboratory systems as not only being a function of x-ray small-angle-scattering but also of the x-ray spectrum and system spatial resolution relative to the size of the imaged structures<sup>42</sup>. While previous dark-field lung studies have used dark-field intensity values to make binary disease classifications<sup>23-25,43</sup>, it is unclear how these results would change at a different magnification or spatial resolution, such as would occur if the measurements were repeated at a different magnification or on a different system. While traditional x-ray measurements are also biased by the applied x-ray spectrum and other systemic effects, many of these can be accounted for with calibration and algorithmic corrections, making these results highly reproducible. It is thus critically important to develop similar

calibration and correction schemes to improve the reliability of x-ray dark-field measurements to properly interpret the meaning of such measurements in the context of lung imaging. Such techniques would benefit both preclinical applications of micro-CT as well as lay the groundwork for human scale applications seeking to benefit from the sub-pixel resolution capabilities of x-ray dark-field.

## 1.2 Research Hypothesis and Specific Aims

The goal of this thesis was to develop strategies to address these challenges as they impact the visualization and quantitative assessment of fibrosis in the lungs. The **central hypothesis** of this work is that the dark-field and attenuation contrast mechanisms, which can be measured simultaneously with grating interferometry, can be used synergistically to leverage the strengths of both and compensate for each other's weaknesses. Specifically, the synergistic benefits to be explained are that dark-field contrast has access to higher resolution information important for distinguishing fibrotic disease while attenuation contrast is quantitative in assessing disease extent.

In this thesis work, a Talbot-Lau x-ray grating interferometer was used to measure attenuation and dark-field because this is the most widely used phase-sensitive x-ray imaging technique owing to its compatibility with standard x-ray sources and detectors. Crystal interferometry is another phase sensitive technique able to measure x-ray dark-field but has had limited use in lung imaging due field-of-view limitations associated with the small crystals used. Non-interferometric grating systems are a promising alternative to interferometers in that they are simpler to use and can operate at medical x-ray energies, but offer less contrast resolution and thus have seen limited adoption in lung imaging applications<sup>44</sup>. Additionally, following the first x-ray dark-field clinical trials using a human-scale Talbot-Lau interferometer<sup>34</sup>, it is likely that applications of grating interferometer dark-field lung imaging will continue to gain momentum.

In this thesis project, a Talbot-Lau interferometer was integrated into a micro-CT to obtain cross-sectional image data, and a mouse model of pulmonary fibrosis, common in the study of IPF, was fixed and imaged *ex vivo* to evaluate the complementary use of attenuation and dark-field contrasts. *Ex vivo* imaging enabled imaging repeatedly at multiple resolutions

while eliminating the effects of motion. It also enabled accurate registration and comparison with ground truth measures of lung structure to validate our methods.

To test this hypothesis the following specific aims were proposed:

**Specific Aim 1:** Design, build, and evaluate a grating interferometer micro-CT system for *ex vivo* small animal lung imaging.

**Specific Aim 2:** Develop, implement, and evaluate correction strategies to address grating-derived beam hardening artifacts.

**Specific Aim 3:** Develop methods to leverage complementary attenuation and dark-field image information and evaluate their impact on visualizing and quantifying pulmonary fibrosis.

### **1.3 Overview of Dissertation**

In addressing these objectives, the thesis is structured as follows:

**Chapter 2** introduces the basic physical interactions and image formation steps involved in x-ray dark-field imaging and provides a review of literature.

**Chapter 3** describes the Talbot-Lau grating interferometer micro-CT imaging system built and used in this work.

**Chapter 4** describes methods developed for this thesis to compensate for the effects of grating-derived beam hardening.

**Chapter 5** details the experiments performed to measure attenuation and dark-field signal in a mouse model of pulmonary fibrosis and qualitatively compares the imaging findings.

**Chapter 6** describes a study used to assess detection and quantification accuracy of fibrosis in a mouse model.

**Chapter 7** summarizes the findings and limitations of the performed research, discusses the potential benefits of grating interferometry for evaluation of pulmonary fibrosis, and discusses future directions for this work.

## CHAPTER 2

---

# X-Ray Image Formation and Motivation for Multi-Contrast Complementarity

### 2.1 Introduction

X-rays are a high-energy form of light used in medical imaging for their ability to penetrate the body and form images of the content and composition of the materials inside. X-rays that pass through the body contribute to the detected signal and local differences in signal define image contrast, the information content of the image. Contrast in these images is the result of differences in the physical interaction strength between x-rays and materials encountered and varies between materials and interaction type. Spatial resolution, or the ability to distinguish small adjacent structures, in medical x-ray imaging is determined by the physics of how the x-ray image is acquired and is generally a compromise between several competing factors. The imaging task defines the contrast and spatial resolution requirements which set physical constraints used to optimize the design of an imaging system. X-ray imaging of the chest, particularly for detecting early-stage lung disease, requires both sufficient image contrast and spatial resolution. Chest imaging is the most common application of x-ray imaging due to the prevalence and morbidity of lung diseases and the natural x-ray attenuation contrast between air and tissue. X-ray attenuation contrast refers to the differential removal of x-rays from the beam by different materials. Attenuation contrast is effective in detecting larger localized changes in structural lung health associated with pathological loss or gain of tissue due to the large inherent attenuation differences between water-like tissues of the lungs and the air contained within them. Large attenuation contrast differences in the lung are often associated with substantial disease burden and are more easily detected. However, contrast from attenuation is low when the pathologic change is subtle and diffuse, as is often the case in early-stage lung disease, making these diseases harder to detect.

Hyperattenuating lung diseases cause regional increases in x-ray attenuation that signify fluid buildup, inflammation, or fibrosis. Making a differential diagnosis among hyperattenuating pathologies is challenging and sufficient image contrast and spatial resolution are critical to the radiologist's diagnostic confidence. Interstitial lung diseases, such as idiopathic pulmonary fibrosis (IPF), are a class of hyperattenuating disease that are particularly difficult to diagnosis and quantify. IPF is distinguished by an irregular restructuring of the lung parenchyma forming small air-filled cysts, a pattern that is referred to as honeycombing<sup>45</sup>. The superimposition of anatomy in attenuation radiography dramatically reduces contrast, making planar chest x-rays ineffective at distinguishing interstitial lung diseases<sup>46</sup>. X-ray CT overcomes this superimposition of anatomy improving contrast between tissue and airspaces. However, due to spatial resolution limitations of CT, certain disease patterns like honeycombing are only resolvable after progressing to more advanced stages.

In x-ray CT, x-ray projections are acquired at angles around the patient and reconstructed into 3D volumes structured as cross-sectional slices. Each voxel in the image represents a location in the patient and its magnitude describes the relative amount of x-ray interactions in that region. Attenuation CT offers quantitative benefits for lung imaging because each voxel (3D image element) represents the tissue density within the voxel, which can be used to infer lung function and health<sup>47</sup>. Insufficient spatial resolution in attenuation CT results in adjacent structures in the lung being averaged together, yielding their mean density, reducing their contrast, and potentially obscuring structures necessary to distinguish disease patterns.

X-ray dark-field imaging has potential to provide enhanced signal to unresolvable small structures blurred out in attenuation images. Challenges, however, include artifacts and lack of quantitative information. Notably, x-ray dark-field signal magnitude cannot be as easily interpreted in terms of lung health as attenuation signal can, as it is influenced by systemic factors like spatial resolution<sup>42</sup> and sample orientation<sup>48</sup>. That attenuation loses signal due to systemic blurring processes whereas dark-field gains contrast from these same sources presents an opportunity for synergy. By combining attenuation and dark-field information, the strengths of each can be leveraged while accounting for their weaknesses.

In particular, dark-field's sub-pixel sensitivity poses an opportunity to improve resolution of small features in attenuation images while maintaining quantitative information.

In this chapter, x-ray physical contrast mechanisms and key x-ray imaging factors influencing spatial resolution are introduced to describe the relative strengths and weaknesses of attenuation and dark-field contrast mechanisms as they relate to lung imaging. This discussion motivates the remaining work in this thesis regarding how these contrast mechanisms can be used together.

## 2.2 X-Rays and Physical Contrast Mechanisms

Medical x-rays are produced by striking high speed electrons into a heavy metal target to transfer kinetic energy into electromagnetic radiation. Depending upon the incident kinetic energy of the electron and the proximity of its trajectory to the nucleus of the target atom, a broad spectrum of different energy x-rays are produced as both Bremsstrahlung radiation and characteristic emission peaks (Figure 2.1).

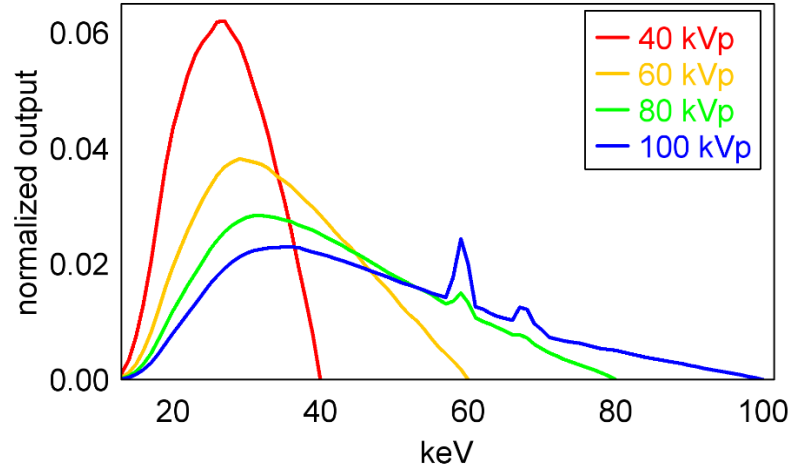


**Figure 2.1** Medical x-rays have a broad spectrum of energies. The smooth portion of the spectrum is generated via Bremsstrahlung, while peaks in the spectrum at higher energies are from characteristic emission. The maximum energy of the spectrum is determined by the electric potential field, in kV, applied to the x-ray source. Spectrum simulated with Spektr 3.0.<sup>49</sup>

Comparing the wavelength of light relative to the size of the matter it interacts with dictates the nature of the interaction. Relatively long wavelengths are better analyzed in terms of

wave behavior, whereas short wavelengths are treated as particles behaving as billiard ball-like projectiles. The wavelength of visible light (700 nm – 400 nm) is considerably longer than the diameter of atoms (0.1 nm), which justifies the classical wave treatment. X-ray wavelengths (0.06 nm – 0.01 nm) are shorter than atomic diameters but considerably larger than the constituent nuclei and electrons. Thus, both wave and particle-like behaviors are exhibited in x-ray interactions.

Treated as electromagnetic waves, x-rays are characterized by their wavelength, amplitude, and phase. Phase (units of radians) describes the point in the wave cycle (e.g., the peak or trough) at a given location in space. Amplitude refers to the strength of the electric field oscillation and relates to the number of photons and intensity (energy per unit time and area) of the x-ray beam. Standard x-ray detectors can only measure intensity. As a result, phase and other wave-specific properties of x-rays are typically omitted in medical imaging discussion. However, by using interferometry, the measure of interference caused by phase differences, these wave-properties can be retrieved for imaging applications. An overview of these wave-interactions and a motivation for their use are summarized in the following sections.

### **2.2.1 X-Ray Wave Propagation Through Matter**

Descriptively, when x-rays penetrate through matter both their amplitude and phase are affected by their interactions with the bound electrons in matter. X-rays drive electrons to oscillate at frequencies inversely proportional to their wavelength. This oscillation of the charged electron results in re-radiation as the x-ray propagates with a phase shift and reduction in amplitude determined by the resonant frequency of the electron. This resonant frequency is determined by electronic bonds with the nucleus and surrounding charged particles. When the x-ray's driving frequency is below this resonant frequency, the driven electron oscillates at the same frequency in phase with the x-ray. When the driving frequency exceeds the resonant frequency, as is often the case in high-energy medical x-rays, the electron oscillation cannot keep pace and there is a phase lag in the propagated wave<sup>50</sup>. When driven near their resonant frequency, electrons can be ejected from the atom rather than re-radiating the x-ray, thereby reducing the x-ray amplitude as energy is ultimately lost to heat in the material. Cumulatively, these phase shift and amplitude

reduction effects can be quantified in terms of the x-ray wavelength  $\lambda$ , its electric field amplitude before  $E_0$  and after  $E$  propagating a distance  $l$  through a given material with complex index of refraction  $n = 1 - \delta + i\beta$ ,

$$E = E_0 \exp\left(-\frac{2\pi i n l}{\lambda}\right) = E_0 \exp\left(\frac{2\pi i \delta l}{\lambda}\right) \exp\left(-\frac{2\pi \beta l}{\lambda}\right). \quad (2.1)$$

Here the real component of the index of refraction  $\delta$  describes the phase shifting properties of the material and  $\beta$  describes the absorption properties. Both  $\beta$  and  $\delta$  vary between different materials and thus can be used as imaging contrast mechanisms. This is demonstrated in **Figure 2.2** with four wave fronts passing through materials of differing  $\delta$  and  $\beta$ . Compared to the x-rays propagating through free space, x-rays passing through  $\beta > 0$  materials lose amplitude, while those passing through  $\delta > 0$  accumulate phase shifts.

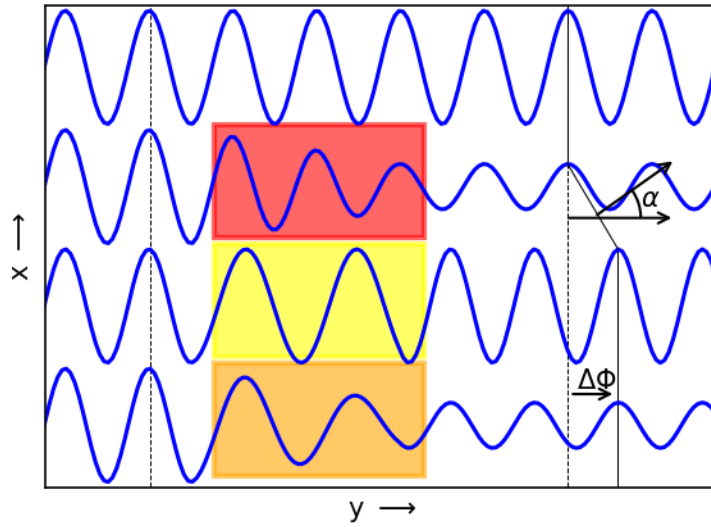


**Figure 2.2** Diagram of x-ray plane waves propagating in the positive  $y$  spatial direction through materials with different complex indices of refraction  $n = 1 - \delta + i\beta$ . The topmost waveform propagates through free space ( $\beta = \delta = 0$ ), the uppermost object is made of material with only absorption properties ( $\beta > 0, \delta = 0$ ). The middle object has only phase shifting properties ( $\beta = 0, \delta > 0$ ). Finally, the bottom material contains both properties ( $\beta > 0, \delta > 0$ ). The dotted line before the objects signifies constant phase across the plane wave before interacting with the objects. Wave fronts passing through phase objects travel with a different phase velocity and accrue a phase difference  $\Delta\Phi$ , while wavefronts passing through absorbing materials lose amplitude. The refracted angle  $\alpha$  between the original wavefront and the phase shifted wavefront is illustrated as the angle between their phase fronts.

Absorption and phase shift accumulate as they propagate through matter according to the Beer-Lambert law. The absorption  $A$  of an object measured at a single x-ray energy can be measured directly by comparing intensity before  $I_0$  and after  $I$  propagating through the object:

$$A(x, z) = \frac{4\pi}{\lambda} \int \beta(x, z, y) dy = -\log\left(\frac{I}{I_0}\right) \quad (2.2)$$

Similarly, the accumulated phase shift  $\Phi$  in each location of the projected plane  $(x, z)$  relates to the  $\delta$  distribution by:

$$\Phi(x, z) = \frac{2\pi}{\lambda} \int \delta(x, z, y) dy. \quad (2.3)$$

As shown in **Figure 2.2**, differential phase shifts at the interface of two materials induce a change in the wavefront's propagation direction known as refraction. The refracted angle  $\alpha$  is given by Snell's law

$$\alpha = \frac{\lambda}{2\pi} \frac{\partial \Phi}{\partial x}. \quad (2.4)$$

Due to the small wavelength of medical x-rays ( $\lambda < 0.1$  nm),  $\alpha$  is typically on the order of microradians, meaning this scattering is predominantly in the forward direction.

### 2.2.2 Material Properties Influencing X-Ray Contrast

The wave description of x-ray interactions predicts the behavior of many x-ray photons acting together. The description specifically separates the absorption and forward scattering components into the real and imaginary components of the index of refraction. These group effects can be described in terms of three individual x-ray particle-like photon-atomic interactions. These include photoelectric absorption, Compton scattering and Thompson scattering.

Photoelectric absorption is the process by which an x-ray photon near the binding energy (resonant frequency) of an inner shell electron is completely absorbed, ejecting the electron. At medical x-ray energies, photoelectric absorption is the primary contributor to  $\beta$  absorption but only accounts for a fraction of the total interactions<sup>51</sup>. The likelihood of

photoelectric absorption increases at lower energies  $E$  and higher atomic numbers  $Z$ , by  $Z^3/E^3$ .

Compton scattering is an inelastic scattering where part of the photon energy is lost to ejecting an outer shell valence electron. Due to electron shielding, the binding energies of these valence electrons are largely independent of the nuclear charge meaning that Compton scattering is not effective for differentiate materials of different  $Z$ . At medical x-ray energies well above valence electron binding energies, the likelihood of Compton scattering is also approximately independent of the incident x-ray energy. Given that photoelectric absorption probability diminishes quickly at higher energies, Compton scattering is the predominant x-ray interaction at medical energies responsible for a greater proportion of interactions at higher energies.

Thompson scattering is an elastic scattering dependent on electron density and distribution where the x-ray is absorbed at an electron's binding energy and re-radiated in a different direction without a loss in energy. As medical x-rays are above most electron binding energies, Thompson scattering is the least likely x-ray interaction. Its probability of interaction scales with atomic number and inversely with energy by approximately  $Z/E$ .

The redirection of x-ray trajectories associated with these elastic and inelastic scattering interactions are the result of phase shifts and collectively contribute to  $\delta$  effects<sup>44</sup>.

As both absorption and scattering can remove x-rays from the beam, these effects are combined in measures of x-ray attenuation. Cumulatively these effects are quantified as the linear attenuation coefficient  $\mu$  which gives x-ray intensity loss per unit distance. In attenuation imaging, scatter can reduce intensity in one detector element by scattering the radiation into an adjacent detector element. This reduces image contrast and is undesirable. For this reason, collimators are used to exclude scatter in attenuation imaging. In this case where scattered radiation is excluded, the terms attenuation and absorption contrast can be used interchangeably as attenuation is assumed to be primarily due to absorption.

However, by ignoring and intentionally excluding these phase effects in attenuation imaging a substantial amount of imaging contrast is left unutilized. Both  $\delta$  and  $\beta$  effects

derive from atomic properties of the imaged material and thus can be utilized as image contrast:

$$\delta = \frac{r_e \lambda^2}{2\pi} \sum_k N_k f_1(Z_k, E) \quad (2.5)$$

$$\beta = \frac{r_e \lambda^2}{2\pi} \sum_k N_k f_2(Z_k, E). \quad (2.6)$$

Here  $r_e$  is the electron radius,  $N_k$  is the atomic density of each element  $k$  in the imaged material, and  $f_1$  and  $f_2$  are the real and imaginary atomic scattering factors for a given element of atomic number  $Z_k$ <sup>52,53</sup>. **Eq. 2.5, 2.6** state that  $\delta$  and  $\beta$  values for a given material measured at an x-ray wavelength  $\lambda$  can be described as the sum of their constituent atomic scattering factors weighted by their respective atomic densities  $N_k$ . Standard values of these atomic scattering factors are available for each element at a wide range of x-ray energies<sup>54</sup>.  $\delta$  and  $\beta$  are reported for several light and heavy materials at 30 keV and 60 keV in **Table 2.1**<sup>55</sup>. At these energies  $\delta$  and  $\beta$  are exceptionally small, the small  $\beta$  component accounts for the high penetration that x-rays are known for. However, in lighter materials with low  $Z$  such as tissues that are mostly water,  $\delta$  is orders of magnitude greater than  $\beta$ , supporting the use of x-ray phase contrast for soft tissue imaging applications at medical x-ray energies<sup>44</sup>.

**Table 2.1** Reference values of the real and imaginary components of the complex index of refraction. Values available at [https://henke.lbl.gov/optical\\_constants/pert\\_form.html](https://henke.lbl.gov/optical_constants/pert_form.html)

Material	30 keV			60 keV		
	$\delta$	$\beta$	$\delta/\beta$	$\delta$	$\beta$	$\delta/\beta$
<b>Water</b>	$2.56 \times 10^{-7}$	$1.06 \times 10^{-10}$	$2.42 \times 10^3$	$6.42 \times 10^{-8}$	$2.93 \times 10^{-11}$	$2.19 \times 10^3$
<b>polyimide</b>	$3.38 \times 10^{-7}$	$1.15 \times 10^{-10}$	$2.94 \times 10^3$	$9.70 \times 10^{-8}$	$5.01 \times 10^{-11}$	$1.94 \times 10^3$
<b>polypropylene</b>	$2.37 \times 10^{-7}$	$7.01 \times 10^{-11}$	$3.38 \times 10^3$	$5.95 \times 10^{-8}$	$2.39 \times 10^{-11}$	$2.49 \times 10^3$
<b>Teflon</b>	$4.87 \times 10^{-7}$	$2.46 \times 10^{-10}$	$1.98 \times 10^3$	$1.22 \times 10^{-7}$	$7.09 \times 10^{-11}$	$1.72 \times 10^3$
<b>Ti</b>	$9.68 \times 10^{-7}$	$7.08 \times 10^{-9}$	$1.37 \times 10^2$	$2.41 \times 10^{-7}$	$5.60 \times 10^{-10}$	$4.30 \times 10^2$
<b>Fe</b>	$1.70 \times 10^{-6}$	$2.01 \times 10^{-8}$	$8.46 \times 10^1$	$4.22 \times 10^{-7}$	$1.54 \times 10^{-10}$	$2.74 \times 10^1$

## 2.3 Measuring X-Ray Phase Properties

While both real and imaginary components of the complex index of refraction can be used for imaging, only the absorptive component can be measured directly by x-ray detectors that are sensitive to light intensity. Phase is measured via interferometry, the process of measuring interference. Interference is the phenomenon where wave amplitude increases or decreases when two or more waveforms of different phase overlap. Common to all interferometers is splitting a beam of light into two or more paths of different propagation distance or index of refraction such that when rejoined an interference pattern of bright and dark intensity fringes forms. By measuring the intensity pattern fringe locations both before and after placing an object in the beam line the shifted location of the fringe pattern can be determined and the change in phase can be retrieved.

### 2.3.1 Talbot-Lau Grating Interferometry

Talbot-Lau grating interferometry is the most common phase measurement technique in medical imaging applications because it enables interferometry with conventional x-ray sources with poor *coherence*<sup>56</sup>. Phase measurements require highly *coherent* x-rays, meaning that their phase fronts stay constant as they propagate (e.g., the waves shown in the top two rows of **Figure 2.2**). When using incoherent waves, phases average out and cannot be retrieved. Conventional sources have both poor temporal coherence due to their broad wavelength spectrum (**Figure 2.1**) as well as poor spatial coherence due to their large focal spot sizes. The Talbot-Lau grating interferometer (**Figure 2.3**) relaxes these coherence requirements by using a spatial comb filter with period  $p_0$ , referred to as an absorption grating. When illuminated by incoherent x-rays, the evenly spaced lamellae, like posts in a fence, block out a portion of the light producing an array of point-like sources. These point sources produce a spatially coherent plane wave according to Huygen's principle<sup>50</sup>. The plane wave produced by this absorption grating, referred to in the system as the source grating (abbreviated  $G_0$ ) is then ready for interferometry.

The next grating in the interferometer is the phase shift grating  $G_1$ , which is substantially thinner than  $G_0$  and induces a regularly spaced phase shift with minimal absorption. The narrow period of the phase shift grating ( $p_1$ ) causes the coherent x-rays to diffract,

spreading slightly and superimposing, yielding a diffraction pattern called a Talbot carpet. Named after its discoverer, Henry Fox Talbot observed in 1836 that coherent light, when passed through a grating, creates an interference pattern that is the repeating image of the grating at regular intervals, called Talbot lengths<sup>57</sup>. Specifically, the phase shift pattern of  $G_1$  repeats at integer Talbot lengths of  $2(p_1)^2/\lambda$ . This becomes useful for imaging phase effects halfway between these Talbot lengths because there is a half-sized *intensity* image of  $G_1$  that is phase sensitive and can be measured by a detector. This intensity pattern is considered phase sensitive because its lateral position is translated in the presence of an object-induced phase shift. These half Talbot lengths are called the Talbot distances  $d_T$  and define the geometry for a given interferometer. Talbot distances are given by

$$d_T = n(p_1)^2/\lambda \quad (2.4)$$

where  $n$  is the integer Talbot order of the system. When an object is placed in an interferometer, such as the wedge in **Figure 2.3**, interfaces, or lateral gradients in phase  $\partial\Phi/\partial x$  refract the x-ray wavefront by angle  $\alpha$  (**Eq. 2.4**). These refracted wavefronts then shift the Talbot carpet laterally a distance of

$$S = \tan(\alpha d) \approx \alpha d. \quad (2.8)$$

The sensitivity of an interferometer defines how much lateral shift in the interference pattern  $S$  results for a given differential phase shift  $\partial\Phi/\partial x$  which increases by imaging at higher Talbot order (**Eq. 2.7**). Increasing sensitivity improves image contrast but poses the risk of phase wrap as phase is a circular measurement bounded by  $(-\pi, \pi)$  radians. When the lateral shift  $S$  of the interference pattern exceeds the period of the pattern, a discontinuity forms as the true phase shift cannot be unambiguously recovered.

An additional consequence of using a grating interferometer to measure phase comes with using medical x-rays with wavelengths  $\lambda < 0.1$  nm ( $E > 12.4$  keV). **Eq. 2.7** states that to keep system geometry compact, the phase grating  $G_1$  must be manufactured with a period of  $p_1 < 10$   $\mu\text{m}$ . This then requires an x-ray detector with a pixel size  $< p_1/3$  to resolve changes in interference pattern. Detectors with such a small pixel size are of limited use in

medical imaging due to their limited field-of-view. However, increasing  $p_1$  to facilitate larger pixels and fields of view dramatically increases the geometry length.

To overcome this issue in resolving the Talbot carpet, a final absorption grating  $G_2$ , called the analyzer grating, is positioned at an  $n$  order Talbot distance (Eq. 2.7) from  $G_1$  and just in front of an x-ray detector<sup>17</sup>. The period of the analyzer grating  $p_2$ , is designed to match the period of the interference pattern at a given Talbot distance at the detector plane:

$$p_2 = M \frac{p_1}{2} \quad (2.9)$$

accounting for the effects of magnification,  $M = (L + d)/L$ , where  $L$  and  $d$  are the inter-grating distances defined in Figure 2.3.

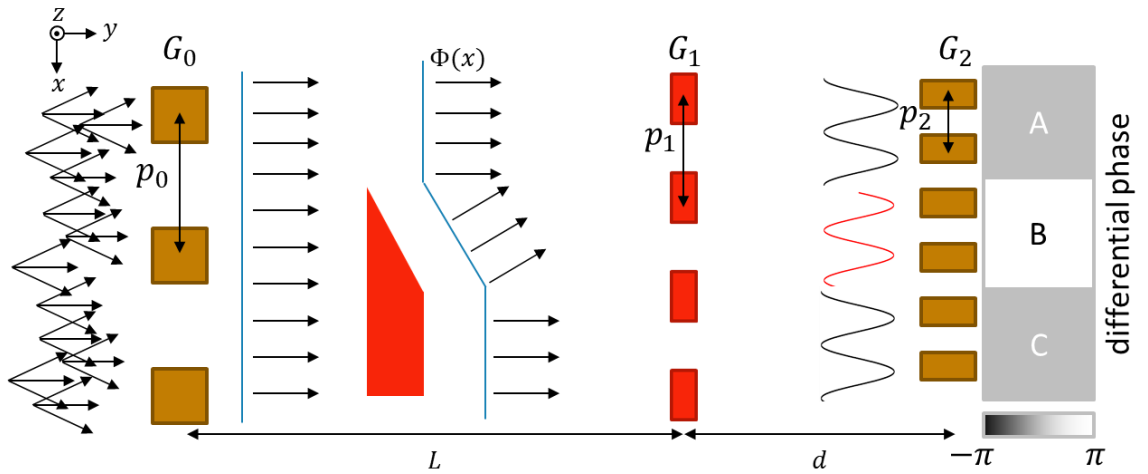


**Figure 2.3** Top-down view diagram of a Talbot-Lau grating interferometer. X-rays are represented by arrows pointing normal to their wave front. Following the x-ray path from the source,  $G_0$  spatially filters the incoherent x-rays yielding a coherent plane wave. From this plane wave  $G_1$  produces a downstream interference pattern. While passing through a pure phase wedge, the wavefront travels at a different phase velocity. In the slanting region of the wedge ( $\partial\Phi/\partial x > 0$ ) refraction changes the propagating direction of the wavefront by angle  $\alpha$ , which then laterally shifts the interference pattern introducing a phase shift  $\phi$  in the measured phase stepping curve (shown as red sinusoid curve). Following phase retrieval, the differential phase in the pixel behind the wedge slant (pixel B) is recovered, while adjacent pixels (A and C) report no differential phase shift.

By placing  $G_2$  in front of a detector and then precisely translating the grating laterally in the  $x$  direction, the local interference pattern can be sampled using larger detector pixels. This process is called phase stepping and is demonstrated in Figure 2.4 to generate a set

of phase step curves (PSCs) for a single pixel (e.g., pixel B in **Figure 2.3**). Here the gray curves represent the intensity pattern measured at the plane of the detector as a function of position over two periods. The colored dots represent the measured PSC signal for each detector acquisition after 10 translation steps of  $G_2$  covering two periods of the interference pattern. The reference PSC shows the interference pattern with no object in the beam line and is approximated as a sinusoid of the form

$$I(x) = a_0 + a_1 \sin\left(\frac{2\pi x}{p_2} - \phi\right) \quad (2.10)$$

### 2.3.2 Multi-Contrast Signal Retrieval

After inserting an object into the interferometer and repeating the phase stepping procedure, the offset  $a_0$ , amplitude  $a_1$ , and phase  $\phi$  can change. By measuring the changes in these sinusoid parameters three image contrasts can be retrieved: attenuation  $A$ , differential phase  $\Delta\phi$ , and dark-field  $D$ . First, comparing the change in phase step curve offset is analogous to comparing intensities in traditional radiography to measure attenuation  $A$  (**Eq. 2.2**). Second, the measured PSC phase difference  $\Delta\phi$  relates to the refracted angle  $\alpha$  by

$$\Delta\phi = 2\pi\alpha \frac{d}{p_2}. \quad (2.11)$$

Combined with **Eq. 2.4**, the measured PSC phase can then be related back to the x-ray phase shift in the sampled object

$$\Delta\phi = \frac{\lambda d}{p_2} \frac{\partial\Phi}{\partial x}. \quad (2.12)$$

Given that a detector pixel period could cover several periods of  $G_2$ , **Eqs. 2.11, 2.12** assume the x-ray phase shift to vary slowly such that each opening in  $G_2$  is sampling the interference pattern at the same phase in the cycle. Consequences of when this assumption does not hold are discussed in **Section 2.6**. Further implementation details of how these parameters are estimated and the three contrasts are retrieved are presented in **Chapter 3**.

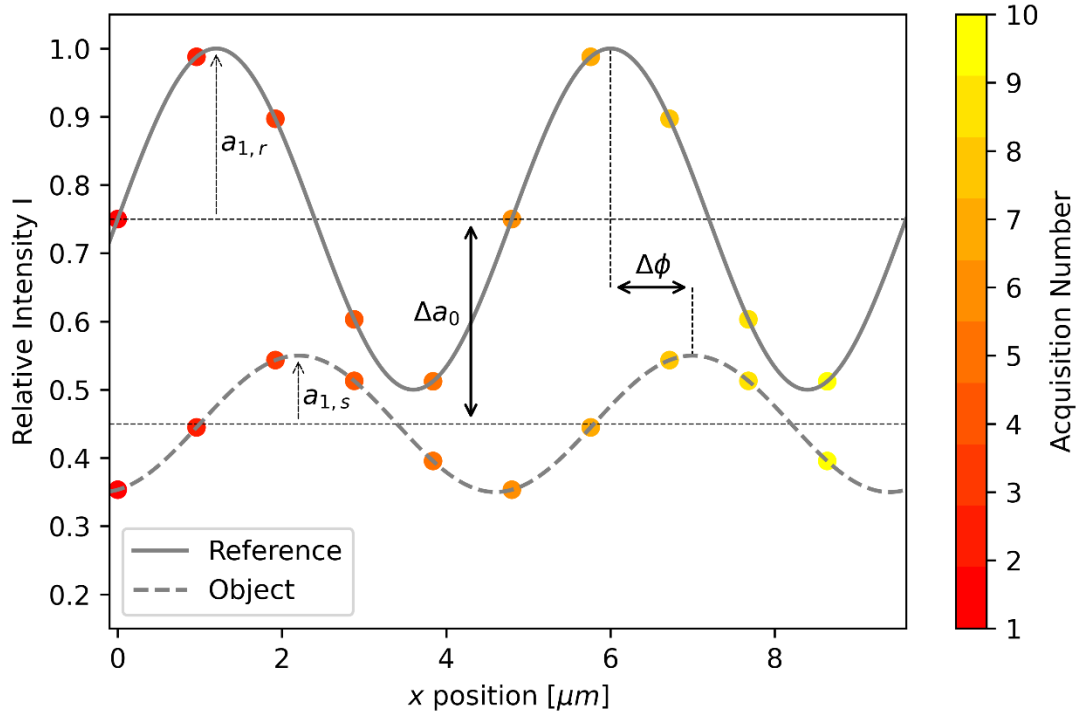


**Figure 2.4** Phase stepping diagram showing the measured x-ray intensity at a single pixel as a function of the lateral translation of  $G_2$  in the  $x$  direction. Depending on the size of the detector pixel the above curves could be the averaged signal of a few or many adjacent periods (fringes) of the interference pattern measured ideally at the same phase with each acquisition. The solid gray phase step curve (PSC) shows the reference interference pattern with no object in the beam line. By adding an object to the beam line this PSC can undergo a change in offset of  $\Delta a_0 = a_{0,r} - a_{0,s}$ , a phase shift of  $\Delta\phi = \phi_r - \phi_s$ , or a change in amplitude of  $\Delta a_1 = a_{1,s}/a_{1,r}$ .

The third image contrast available from grating interferometer phase stepping curves is the reduction in amplitude  $a_1$  of the PSC. More generally in interferometry, the amplitude of the interference pattern characterizes the *visibility*  $V$  of the interferometer, the magnitude of the oscillations relative to the mean intensity

$$V = a_1/a_0. \quad (2.5)$$

A measure of the visibility reduction by the sample is then given by taking the local reductions in visibility caused by a sample visibility  $V_s$  and normalizing them relative to the reference visibility of the interferometer with no sample  $V_r$ ,

$$V_N = V_s/V_r \quad (2.6)$$

Dark-field contrast  $D$  is then defined as the negative logarithm of this normalized visibility such that reductions in visibility result in elevated dark-field<sup>58</sup>

$$D = -\log(V_N). \quad (2.7)$$

The term x-ray dark-field, introduced by Pfeiffer et al. 2008<sup>18</sup>, derives from its similar appearance to optical dark-field microscopy. In optical dark-field microscopy, the central beam is blocked, and signal derives from scattering off the sample which is focused back into the detector resulting in a dark background<sup>59</sup>. Similarly x-ray dark-field images characteristically have a dark background and elevated signal at scattering surfaces. As a result, x-ray dark-field was originally introduced as deriving from small-angle-x-ray scattering (SAXS), a material property related to both content and structure. SAXS is a consequence of phase shifts from particularly small objects ( $<1 \mu\text{m}$ ), or porous materials where the wavefront scatters in a forward cone of angle  $\alpha$ <sup>37</sup>. As a result of the equal and opposite phase shifts induced by SAXS at the detector plane the resulting superimposed wavefront measured by interferometer has a reduced visibility (amplitude) compared to the reference PSC (**Figure 2.5**). This connection between x-ray dark-field measurements and SAXS has been confirmed with synchrotron experiments.<sup>60</sup>

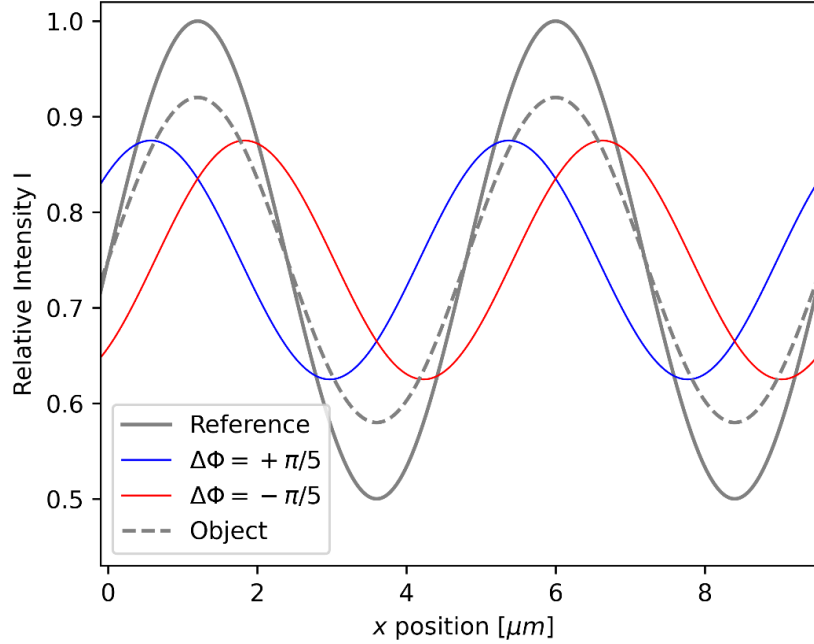


**Figure 2.5** Phase step diagram demonstrating x-ray dark-field resulting from small-angle x-ray scattering where scatter in an equiangular cone yields equal and opposite phase shifts (demonstrated as blue and red constituent curves  $\Delta\Phi = \pm\pi/5$ ) which interfere reducing the amplitude of the interference pattern before the analyzer grating  $G_2$ .

## 2.4 Computed Tomography of X-Ray Contrasts

Planar x-ray projection images are valuable for screening of certain lung diseases. However, for quantitative staging and making definitive diagnoses of interstitial lung diseases, the contrast reduction due to superimposed anatomy in chest radiography is a major challenge. Computed tomography (CT) overcomes this by reconstructing axial cross-sectional images mapping the location and magnitude of x-ray interactions. This is done by taking line integrals (projections) measured at different angles around the object of interest and solving for the constituent materials, position, and thickness that generated the line integral. **Eqs. 2.2, 2.3** present line integrals of x-ray attenuation and phase which can be reconstructed using CT. In attenuation CT, the measured quantity is the linear attenuation coefficient  $\mu$ , related to  $\beta$ , calculated from attenuation projections  $A$  (**Eq. 2.2**) acquired at different angles  $\theta$  for a given x-ray energy  $E$

$$\mu(x, y, z; E) = R^{-1}(A(x, z, \theta)) = \frac{4\pi\beta(x, y, z; E)}{\lambda}. \quad (2.8)$$

$R^{-1}$  represents the inverse Radon transform, a mathematical operator mapping angular projections to their cross-sectional distribution. More details on the implementation of the inverse Radon transform and CT details are discussed in **Chapter 3**. Similarly, x-ray phase can also be reconstructed via CT yielding the phase coefficient  $\eta$ <sup>44</sup>

$$\eta(x, y, z; E) = R^{-1}(\Phi(x, z, \theta)) = \frac{2\pi\delta(x, y, z; E)}{\lambda}. \quad (2.9)$$

Unique to phase contrast imaging in grating interferometry is that the *differential phase*  $\partial\Phi/\partial x$  is measured (**Eq. 2.12**), which must be integrated in the reconstruction process. By measuring and reconstructing the absorption and phase coefficients, the complete complex index of refraction is recovered.

X-ray dark-field deriving from SAXS has also been shown to accumulate as a line integral and thus can be reconstructed using CT, where the measured quantity has been termed the linear diffusion coefficient<sup>61,62</sup>.

## 2.5 Practical Considerations in X-Ray CT Measurements

The inversion process of recovering attenuation and phase information from x-ray projections is based on several assumptions which in practice do not generally apply. Not accounting for these inconsistencies can result in quantitative inaccuracies and reduction in image quality. In CT, assumptions about x-ray energy homogeneity and sampling spatial resolution can have a particularly large impact and must be accounted for with preprocessing and correction strategies. These same data inconsistencies pose additional challenges for grating interferometry due to the added complexity of the grating structures and data acquisition process.

### 2.5.1 Beam Hardening

One of these data inconsistencies is the log linear relationship between attenuation and measured intensity (**Eq. 2.2**). This simplification only applies when imaging with monoenergetic x-rays, which is not the case in medical imaging applications with

conventional sources generating x-rays via Bremsstrahlung (**Figure 2.1**). This same inconsistency applies for measured phase and dark-field coefficients. Both  $\delta$  and  $\beta$  are energy dependent and increase as x-ray energy decreases (**Table 2.1**). At medical energies, x-ray absorption is proportional to  $1/E^3$ , causing lower energy x-rays to be preferentially absorbed and increases the mean energy of the spectra. This process of beam hardening reduces the magnitude of attenuation and phase interactions as x-rays penetrate matter. Beam hardening has also been shown to generate dark-field signal in absence of unresolvable edges<sup>40</sup>. Beam hardening interferes with quantification of CT images by progressively underestimating the attenuation and phase shift deeper in matter. While beam hardening corrections have been developed for attenuation<sup>63</sup> and phase imaging<sup>38</sup>, use of x-ray gratings with a broad x-ray spectra generates a spatially varying beam hardening that has not been addressed with existing approaches. In CT, these beam hardening artifacts form high frequency rings which can challenge quantification of the high frequency structures native to the lungs.

### 2.5.2 Spatial Resolution

Another unrealistic assumption in the previous discussion of radiographic and CT measurements is of infinitely fine spatial sampling. In practice, spatial sampling is discretized with a sampling interval large enough to ensure sufficient signal to noise ratios. The spatial sampling determines a system's spatial resolution, which refers to the scanner's ability to separate closely spaced objects. Some primary factors that affect spatial resolution include the x-ray source focal spot size, detector pixel size, subject magnification, motion related to the imaging system and subject stability, as well as angular spacing between projections<sup>51</sup>. The effect of each of these factors has a cumulative blurring effect, reducing spatial resolution and contributing to the system's point spread function (PSF)  $h$ . Described mathematically, when an imaging system with PSF  $h$  samples an object  $f$ , the resulting image  $f'$  is the product of the sampled object convolved ( $*$ ) with the imaging system's PSF

$$f' = h * f. \quad (2.18)$$

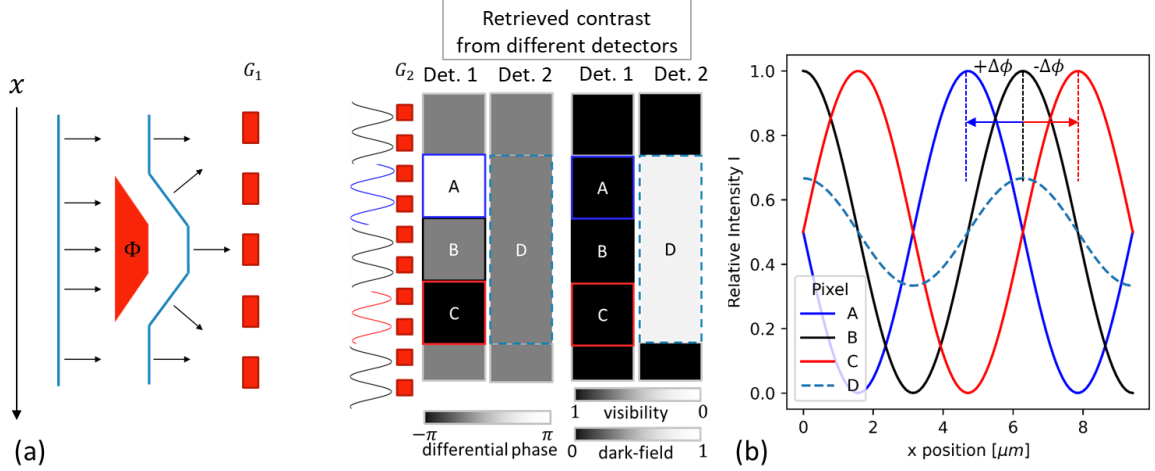
As every component in the imaging system has a PSF with nonzero width, their individual PSFs compound into the final PSF. This sampling by a PSF with finite width has the effect of smoothing edges and reducing contrast when the size of the sampled object is comparable or smaller than the PSF width. This loss in contrast due to insufficient spatial resolution in volumetric imaging is referred to as the partial volume effect. Quantitatively, image contrast decreases linearly with partial volume effect as less of the object of interest is covered by the detector<sup>51</sup>. In cases where cone-beam geometries cause partial volume effects to vary by projection angle this can result in non-linear streaking effects<sup>64</sup>. In low-resolution imaging of the lungs as used in clinical and *in vivo* micro-CT, the linear partial volume effect accounts for much of the lung signal as individual structures are far too small to be imaged directly so an intermediary attenuation signal between air and tissue, related to the lung density, is reported in the reconstructed voxel. In these situations lung structure can only be inferred indirectly by this density value<sup>47</sup> or by the texture of a neighborhood of voxels<sup>10</sup>.

Image noise is innately tied to spatial resolution in x-ray imaging and is dependent on the number of measured x-rays. Noise is reduced by detecting more x-rays either by increasing the x-ray exposure rate or increasing the detector pixel dimensions to integrate more intensity in a larger area or over a longer time. X-ray source emission rates are ultimately limited by x-ray tube heating limitations and in most practical instances can only be increased by using a larger tube filament and focal spot, which contribute to penumbral blur, negatively impacting spatial resolution by increasing the PSF. For a fixed source size, integrated x-ray intensity is then most easily increased by increasing integration time and detector pixel area. In both clinical CT and micro-CT lung imaging applications, there are pressures to keep scan times as short as possible to reduce the effects of motion blur and increase scanner throughput. In designing a CT scan protocol, these data acquisition factors all compete, and their optimal values are application dependent. In CT lung imaging, there is a higher tolerance for noise due to the high contrast between air and tissue, enabling higher spatial resolutions compared to other soft tissue applications. Despite this, due to the high spatial frequency hierarchical structure of lungs and the progressive nature of interstitial lung diseases, early detection remains resolution limited<sup>21,22,65</sup>.

## 2.6 Dark-Field from Intra-Pixel Phase Gradients

Distinct from x-ray attenuation, x-ray dark-field signal can increase as spatial resolution decreases. This effect has been shown in several dark-field experiments performed outside of synchrotron facilities with large focal spot x-ray sources and large detectors routinely encountered in biomedical imaging to facilitate the larger fields of view and shorter scan times<sup>40–42,66,67</sup>. In addition to SAXS, these experiments with Talbot-Lau interferometers using conventional detectors and sources identified other sources of visibility reduction in PSCs, including sharp edges<sup>41,66</sup>, beam hardening<sup>40</sup>, and insufficient spatial resolution<sup>42</sup>. These additional sources of visibility reduction result in an increase in dark-field signal (**Eq. 2.15**). With the exception of beam hardening, these other sources of dark-field can be understood as arising from intra-pixel phase gradients where phase signal in small structures is lost to partial volume averaging<sup>42</sup>.

To illustrate how a large PSF can reduce interferometer visibility via intra-pixel phase gradients and thus generate dark-field signal, **Figure 2.6a** shows the same grating interferometer from **Figure 2.3** with a uniform phase sample with two gradient edges. Differential phase and dark-field signals of this same sample but retrieved from two detector configurations with different pixel sizes are shown at the right of **Figure 2.6a**. The first detector configuration, Det. 1, features small pixels A, B, and C, able to resolve the two phase-gradients which appear as a positive and negative differential phase impulses with no drop in visibility and thus no dark-field signal. The second detector configuration, Det. 2, features a large pixel D, larger than pixels A, B, and C from Det. 1, and measures the average interference pattern signal measured directly behind both gradients. This intra-pixel phase gradient, encompassed by the larger pixel D, breaks the assumption of slowly varying phase relative to the size of the system PSF, discussed in **Section 2.3**. The retrieved differential phase and dark-field signals from pixel locations in each detector configuration are explained by the recorded phase stepping curves in **Figure 2.6b**. Small pixels A and C from Det. 1 each record the positive and negative phase shifted curves ( $\pm\Delta\phi$ ) associated with the positive and negative differential phase impulses from the same pixel locations in **Figure 2.6a**. Larger pixel D shows the averaged signal resulting in net zero phase shift and reduced visibility responsible for the increased dark-field from its location in **Figure 2.6a**.



**Figure 2.6** X-ray dark-field from intra-pixel phase gradients. (a) grating interferometer with a uniform phase object  $\Phi$  with two gradient edges generating a positive phase shift in the interference pattern (blue) and negative phase shift (red). At right of the analyzer grating  $G_2$  are the retrieved differential phase and dark-field signals following phase stepping (curves shown in panel (b)) using two different detector configurations, Det. 1 and 2. The first detector features small pixels A, B, and C able to resolve the two gradient edges as positive and negative differential phase impulses  $\pm\Delta\phi$  and zero dark-field (visibility = 1) behind measured behind the gradient edges. The second detector configuration features large pixels D, larger than A, B, and C combined. The larger pixel D averages the local shifts in the interference pattern caused by the two gradients yielding no measure phase shift but a positive dark-field signal due to a loss in visibility (Eq. 2.15). (b) These retrieved differential phase and dark-field signals can be understood by their measured phase step curves as measured by small pixels A, B, and C from Det. 1 and the large pixel D from Det. 2. Small pixels A and C from Det. 1 located directly behind the gradients in (a) can resolve the positive and negative phase shifts ( $+\Delta\phi$ ,  $-\Delta\phi$ ). However, the large pixel D from Det. 2 in (a) covers both gradients, averaging the gradients and yielding a reduced visibility and thus positive dark-field signal.

## 2.7 Previous Works on Complementarity of X-Ray Contrasts

Previous examples of combining information in x-ray attenuation and dark-field have largely been limited to radiographic applications. Notably, the depth dependence of both attenuation and dark-field has been used to produce a normalized image, called normalized scatter<sup>58</sup>, whose signal magnitude is independent of penetration depth

$$\Gamma(x, z) = \frac{D(x, z)}{A(x, z)} \quad (2.19)$$

This combined parameter has been shown to further improve the sensitivity to emphysema by removing the lung thickness dependence of x-ray dark-field radiography, improving contrast with pathology<sup>24</sup>.

Other examples include using principle component analysis to combine the relationships between attenuation and dark-field signals, along with their spatial relationships, into a lower dimensionality to better classify pulmonary fibrosis than regional mean pixel values<sup>29</sup>.

## **2.8 Conclusions**

The motivation of this work is to leverage the complementarity between x-ray attenuation and dark-field CT with regards to spatial resolution signal dependence to improve spatial resolution and quantitative accuracy. Doing so poses the opportunity to leverage each contrast's strengths while accounting for their weaknesses. Using dark-field information in this way also poses an opportunity to use the same source and detectors to better resolve blurred features. However, in doing so challenges of image artifacts caused by beam hardening and how to best combine these image contrasts to overcome dark-field's sensitivity to spatial resolution must be overcome, which will be explored in the following chapters.

# CHAPTER 3

---

## Experimental System

### 3.1 Introduction

To investigate the complementarity of x-ray physical contrasts, primarily attenuation and dark-field, in enhancing the visualization and quantification of pulmonary fibrosis, an integrated Talbot-Lau grating interferometer micro-CT imaging system was built. As introduced in **Chapter 2**, using a Talbot-Lau grating interferometer, attenuation, differential phase, and dark-field are retrieved from measured alterations in an x-ray interference pattern induced by the sampled object. The interference pattern is modeled as a sinusoid function (**Figure 2.4**). Attenuation derives from a drop in the mean intensity of the sampled sinusoid pattern. Phase is related to lateral shifts in the pattern. Dark-field refers to the reduction in the interference pattern visibility, defined as the sinusoid amplitude relative to its mean intensity. The interferometer is built into a micro-CT system, which is responsible for rotating the sample and recording all three image contrasts for each projection angle. Three reconstructed image series are then generated from these three sets of projection data. A schematic overview of the system is given in **Figure 3.1** with further details on data acquisition, preprocessing, and reconstruction given in following sections.

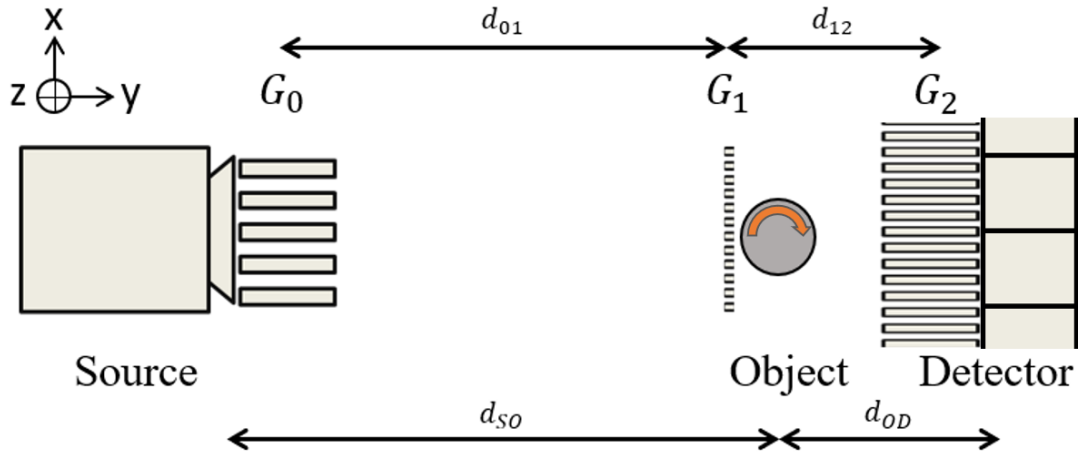


**Figure 3.1** Schematic overview of the Talbot-Lau grating interferometer micro-CT system. The source grating  $G_0$  spatially modulates x rays from a source with a large focal spot.  $G_1$  produces a downstream Talbot carpet sensitive to phase shifts induced by an object in the beam path.  $G_2$  matches the period of the Talbot interference pattern at the detector plane, enabling sampling of the high frequency interference pattern with large detector apertures that can cover several periods of  $G_2$ . A rotating object stage enables tomographic acquisitions by acquiring multi-contrast data at multiple view angles.

### 3.2 System Description

The Talbot-Lau grating interferometer micro-CT system (pictured in **Figure 3.2**) is mounted on a 2.4 m long by 1.2 m wide floating optical bench surrounded by a lead-lined enclosure to minimize radiation exposure to the user while the x-ray source is on. The period and thickness of the three interferometer gratings  $G_0$ ,  $G_1$ , and  $G_2$  define the operating energy and geometry of the grating interferometer and the minimum length of the micro-CT imaging system.

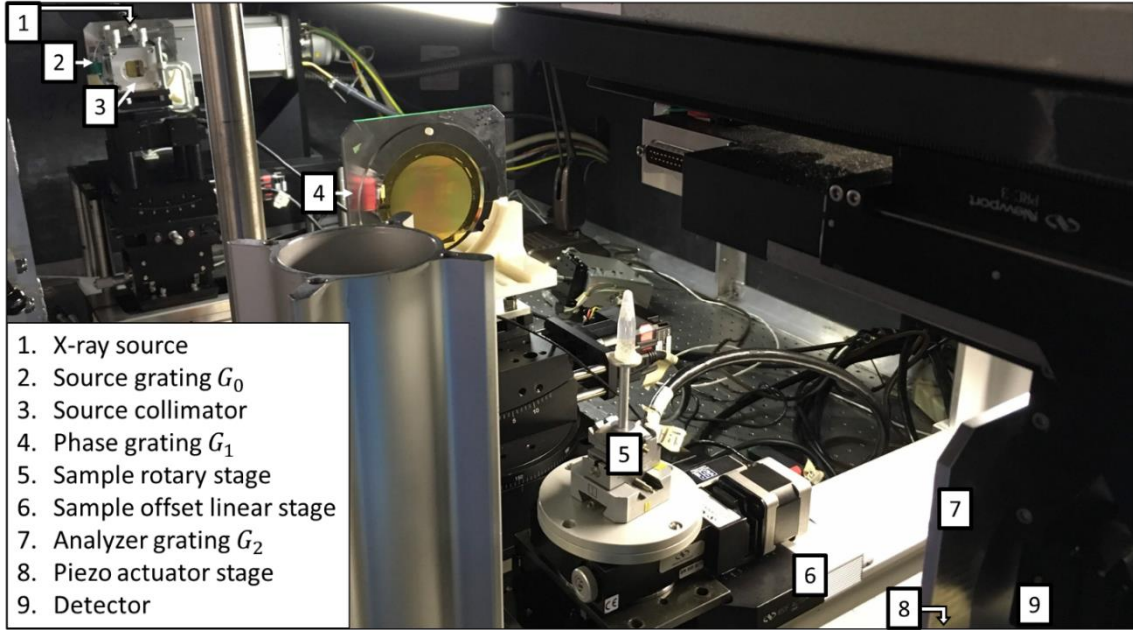


**Figure 3.2** Talbot-Lau grating interferometer micro-CT system photograph with labelled annotations.

### 3.2.1 System Geometry

The length of a Talbot-Lau grating interferometer is set by the imaging Talbot distance (Eq. 2.7) which is determined by the x-ray wavelength and the phase grating period  $p_1$ . This Talbot distance defines the inter-grating distances between  $G_0$  and  $G_1$  ( $L$ ) and between  $G_1$  and  $G_2$  ( $d$ ) (Figure 3.1). Efforts to decrease the overall length of these interferometers are limited by manufacturing challenges in further decreasing the period of the analyzer grating  $p_2$  which must match the phase grating period  $p_1$  (Eq. 2.9). With the minimum system length predetermined by the grating geometry, the remaining micro-CT components were then built around the grating interferometer.

The x-ray source was placed just before the source grating  $G_0$  (Figure 3.2.1). A PANalytical XRF water-cooled tungsten reflection anode with a true focal spot size of  $400 \mu\text{m}$  tall by  $800 \mu\text{m}$  wide was used. The source was positioned such the flat anode face made a 25-degree angle relative to the imaging beam line (y axis in Figure 3.1) to project the cathode long axis into an approximately square effective source plane focal spot size of  $f_s = 400 \mu\text{m} \times 400 \mu\text{m}$ . A rotating sample stage (Figure 3.2.5) was placed at a source-to-object distance of  $d_{SO} = 710 \text{mm}$ . A detector was placed at an object-to-detector

distance of  $d_{OD} = 110$  mm further past the rotation stage along the imaging line. The detector (**Figure 3.2.9**) was a Princeton Instruments PIXIS-XF 2048 water-cooled flat-panel CCD detector with a CsI(Tl) single crystal scintillator and  $13.5\mu\text{m}$  square pixels in a  $2048 \times 2048$  matrix yielding a detector area of  $27.6\text{mm} \times 27.6\text{mm}$ . The source, sample stage, and detector configuration contribute to the system geometry, which is shown to scale in **Figure 3.3** with a geometric sample magnification of  $M = (d_{SO} + d_{OD})/d_{SO} = 1.15$  and cone angle of  $\gamma = 2$  degrees. This magnification, when combined with the effective focal spot size ( $f_s$ ), yields a focal spot size at the object plane with an approximate height and width of  $f_p = 62\mu\text{m}$ , defining the limiting spatial resolution of the system.

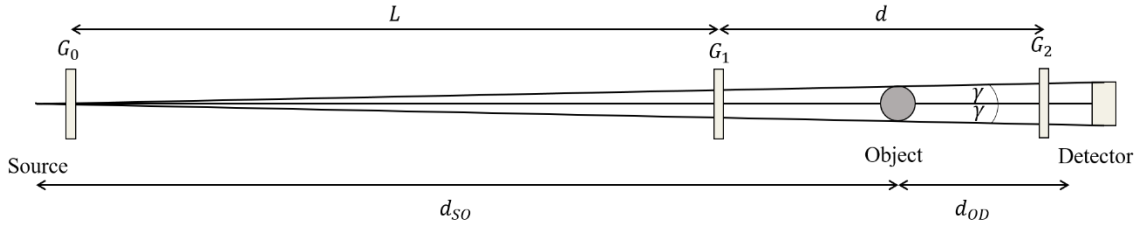


**Figure 3.3** Radiographic geometry of Talbot-Lau grating interferometer system drawn to scale.

### 3.2.2 Talbot-Lau Grating Interferometer Components

The goal of the interferometer is to measure phase using three gratings. To do this, these gratings must be carefully positioned at the correct relative distances and orientations to generate an x-ray interference pattern after  $G_1$  and detected at the plane of  $G_2$ . First,  $G_0$ , placed directly in front of the x-ray source, is oriented with its lamella parallel to the system's vertical  $z$  axis.  $G_0$  is mounted on a multi-axis motorized positioning stage with a linear translational degree of freedom in the system  $x$  direction and rotational degree of freedom along the vertical  $z$  axis, rotating in the  $x - y$  plane. A source collimator is placed immediately in front of  $G_0$  to restrict the spread of the beam to only cover the detector area, reducing scatter. Second is the phase shift grating  $G_1$ , which is placed at distance  $L$  from  $G_0$  and before the rotary sample stage.  $G_1$  requires the most degrees of freedom for aligning the interferometer and thus is mounted on a six-axis motorized positioning axis with lateral translational degrees of freedom in  $x$ ,  $y$ , and,  $z$  directions and rotational degrees of freedom

around those same axes. Third, the analyzer grating  $G_2$ , is placed just before the detector at distance  $d$  from  $G_1$ , and is mounted on a motorized multi-positioning stage with lateral  $x$  and rotational  $z$  degrees of freedom, like  $G_0$ . Additionally,  $G_2$  is mounted on a piezo-electric stage (Mad City Labs), enabling micron-scale translations for phase stepping. Using the motorized positioning stages the three gratings are positioned and aligned to generate a phase sensitive Talbot Carpet between  $G_1$  and  $G_2$  using the alignment methods described by Bech 2006<sup>68</sup>.

The gratings used in the interferometer system (Microworks GmbH, Karlsruhe, Germany) all feature parallel lamellae structures with strong x-ray absorption properties mounted on a non-interacting thin substrate (**Figure 3.4**). All three gratings were manufactured using a LIGA manufacturing process, a deep x-ray lithography technique capable of producing high spatial frequency, thin, and high aspect ratio (height/width > 100) optical elements<sup>69</sup>. Their exact specifications are reported in **Table 3.1**. Generally, the process starts by making a mold of the grating by exposing a light-sensitive polymer (PMMA) to x-ray light and then chemically dissolving away the exposed material. This mold is then filled with gold forming the lamellae before chemically removing the remaining mold, leaving only the gold lamellae on the mounted substrate. The lamella height determines the x-ray absorption.  $G_1$  features short lamellae which negligibly absorb x-rays while inducing a quarter-wavelength ( $\pi/2$ ) phase shift producing periodic pathlength differences necessary to produce the interference pattern described in **chapter 2**.  $G_0$  and  $G_2$  feature considerably taller lamellae to completely absorb the incident x-ray beam. Imaging with higher energy x-rays as required in medical imaging require progressively taller lamellae and are thus more difficult to manufacture and are more prone to manufacturing defects. The most common is deformation of the grating mold while filling with gold leading to cross-linked lamellae, impairing image quality. To minimize cross-linking, the  $G_0$  and  $G_2$  molds were made with the Sunray mold design, where diagonal support struts are built into the mold design to improve structural stability during the gold-infilling process. When these supporting struts are dissolved away with the rest of the mold, they leave behind the holes in the  $G_0$  and  $G_2$  lamellae as depicted in **Fig. 3.2**. The development of the Sunray method has greatly improved grating mold stability enabling taller lamellae and higher energy x-

ray applications. However, at x-ray energy  $> 30$  keV, some cross-linking of lamellae is inevitable. When used in conjunction with CT imaging, the effects of lamellae defects on image quality are compounded across view angles. Methods for addressing these artifacts in grating interferometer CT are introduced in **chapter 4**.

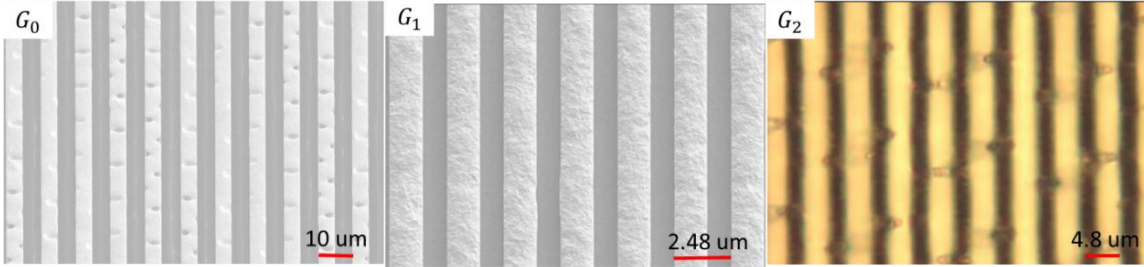


**Figure 3.4** Interferometer gratings.  $G_0$  and  $G_1$  are shown in grayscale scanning electron micrograph images.  $G_2$  is displayed in color as visible-light microscope image.

**Table 3.1** Grating specifications.

Grating	Period (μm)	Duty cycle (%)	Lamellae material	Lamellae height (μm)	Size (cm <sup>2</sup> )	Substrate material	Substrate thickness (μm)
$G_0$	10.0	44	Au	135	6 x 6	graphite	500
$G_1$	3.24	55	Au	2.6	6 x 6	Si	200
$G_2$	4.8	55	Au	130	6 x 6	Si	500

### 3.3 Data Collection

**Figure 2.4** showed theoretical phase stepping curves (PSCs), which are assumed to have a sinusoidal intensity fluctuation as a function of laterally translating  $G_2$  by distance  $x$  to sample the Talbot Carpet (**Eq. 2.10**). These PSCs modeled as sinusoids are defined by three parameters: their mean intensity  $a_0$ , phase  $\phi$ , and fluctuation amplitude  $a_1$ :

$$I(x) = a_0 + a_1 \sin\left(\frac{2\pi x}{p_2} - \phi\right). \quad (3.1)$$

In practice a minimum of three phase steps covering a single Talbot Carpet period ( $p_2$ ) are required to retrieve the three interference pattern parameters used to form three image series. **Figure 3.5** shows experimentally measured PSCs for real materials using the piezoelectric stepper to laterally translate  $G_2$  in six incremental steps across one period in the  $+x$

direction. A cropped view of three even numbered frames of the six phase stepping acquisitions are shown. In each the measured intensity from three regions-of-interest (ROI) is plotted as a function of phase stepping distance with the acquisition number reported as the marker color increasing from red to yellow. Each ROI covers a projection of a material with different x-ray interaction properties. ROI A encompasses a homogenous region of the acrylic cylinder with a shallow gradient, resulting in primarily a drop in the PSC offset. ROI B covers a wooden insert in the cylinder. The fine wooden fibers provide an abundance of phase shifting interfaces and unresolved edges that greatly disrupt the interference pattern and reduce visibility in this region. ROI C is placed near the wall of an air-filled insert and features a strong gradient yield a phase shift in the PSC. Additionally, while  $G_2$  is only translated a total distance of  $p_2 = 4.8 \mu\text{m}$ , a Moire intensity fringe is seen translating to the right across the detector field of view (24 mm). These large Moire fringes are due in part to remaining misalignments in the gratings due to the cone beam spread of the beam when used with parallel grating lamellae. These fringes, with periods of millimeters, travel at a speed and have a period length proportional to the Talbot Carpet translation<sup>70</sup>, and are used in the grating alignment process<sup>68</sup>. Intentional misalignments can be used to directly extract the contrasts from **Eq. 3.1** directly from these Moire fringes in a “single-shot” acquisition but at the expense of spatial resolution<sup>71</sup>.

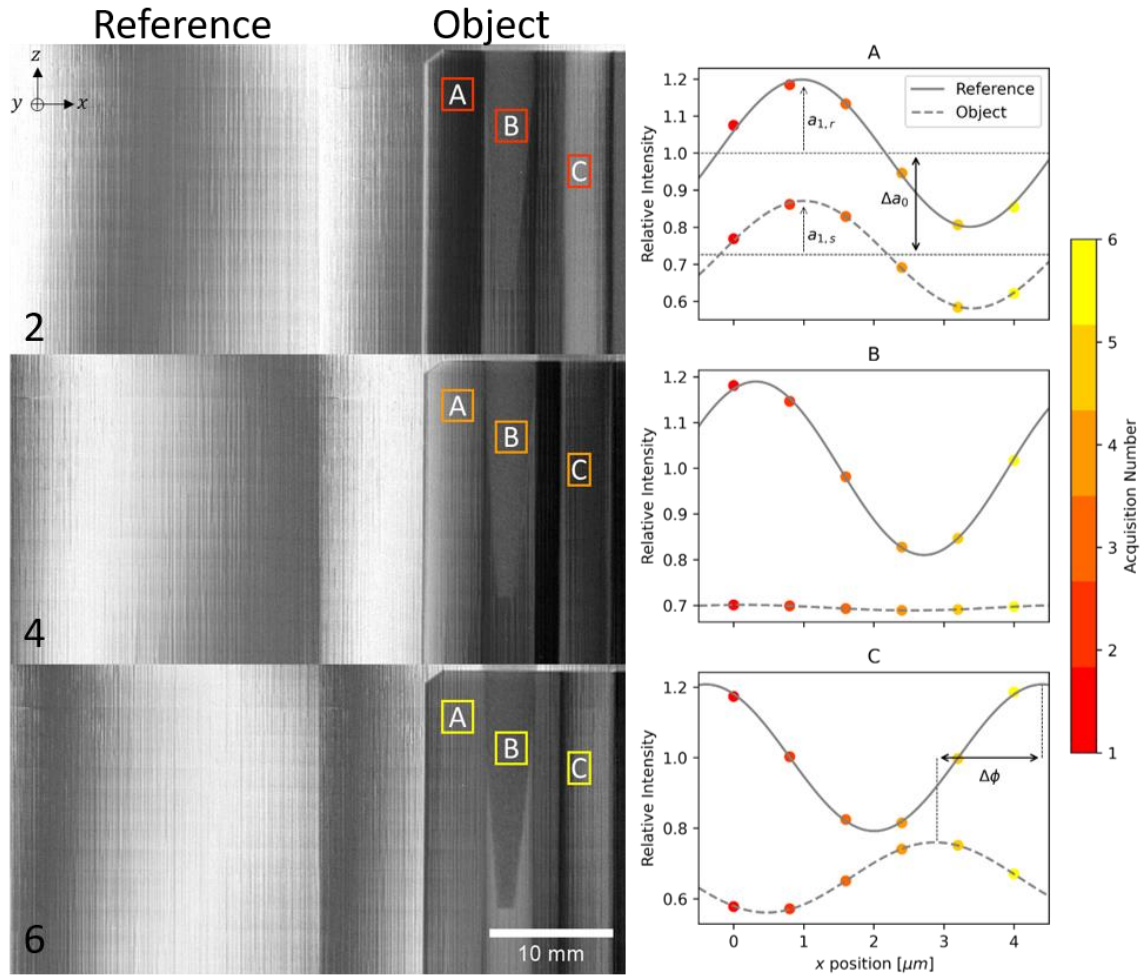


**Figure 3.5** Experimental phase stepping curve images of an acrylic cylinder with a wooden dowel insert and air-filled inserts. Left: Even numbered reference and object phase stepping acquisition images. Three ROIs A-C cover different regions with different x-ray interaction properties with their measured intensities plotted as a function of  $G_2$  translation distance at right. The ROI frame color matches the respective measurement on the plotted PSC.

During the phase stepping procedure images are acquired at each translated position of  $G_2$ , yielding phase stepping samples like the colored points shown in **Figure 3.5** for every pixel location in the detector matrix. A reference PSC is acquired with no sample in the beam and is compared against a PSC acquired with an object to generate image contrasts. From these sampled points, offset  $a_0$ , phase  $\phi$ , and amplitude  $a_1$  from **Eq. 3.1** are found using a curve fitting procedure (gray curves in **Figure 3.5**) applied at every pixel location for both the reference and object PSCs. This curve fitting can be performed efficiently using the Fast Fourier Transform to represent the PSC as a series of sinusoidal basis functions. The

offset is given by the real component of the zeroth Fourier coefficient  $a_0$ . Assuming the PSC covers a single period the amplitude is then given by the real component of the first Fourier coefficient  $a_1$ . Phase is then given by the angle between the real and imaginary components of the complex Fourier coefficient  $\phi_1 = \angle \widetilde{a}_1$ .

Attenuation,  $A$ , is given by the negative log ratio of the sample and reference PSC offsets

$$A = -\log(a_{0_s}/a_{0_r}), \quad (3.2)$$

differential phase contrast  $\Delta\phi$  is given by

$$\Delta\phi = \phi_{1_s} - \phi_{1_r}, \quad (3.3)$$

and visibility  $V$  is given by

$$V = 2a_1/a_0. \quad (3.4)$$

Taking the ratio of the sample PSC visibility with the reference PSC gives the normalized visibility  $V_N$  contrast

$$V_N = V_s/V_r. \quad (3.5)$$

We then define dark-field  $D$  as the negative log of the normalized visibility:

$$D = -\log(V_N) = -\log(V_s/V_r). \quad (3.6)$$

The retrieved contrast images from the phase stepping data of **Figure 3.5** are presented in **Figure 3.6**. These images demonstrate some key differences in x-ray interactions observed in real materials. The low density of the wooden insert has low x-ray attenuation and thus offers little contrast from the acrylic cylinder background. Only the air innervating the fibers offers some difference in image texture. However, these fibers provide an abundance of contrast in the dark-field projection. The differential phase contrast image shows the phase gradient measured in the phase stepping direction ( $\partial\phi/\partial x$ ) and thus interfaces between materials offer the most contrast. However, the wooden insert demonstrates a consequence of the circular extent of differential phase measurements ( $-\pi, \pi$ ). The

abundance of strong gradients and interfaces produce largely uninterpretable signals, and thus a loss of information. This poses a challenge for using phase measurements in highly porous materials. While differential phase projections can be directly integrated to yield full phase, this integration step is commonly incorporated into the image reconstruction filter when performing CT. Further details on this are introduced in the following **Section 3.5**.

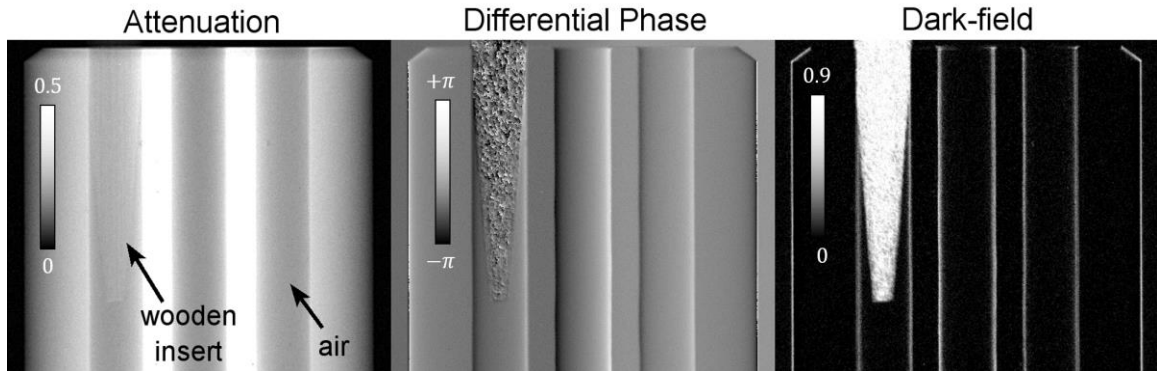


**Figure 3.6** Retrieved contrasts from an x-ray grating interferometer of a cylindrical acrylic phantom with hollow inserts. **Left:** Attenuation projection. Arrows indicate a wooden insert and air in the empty phantom chambers. **Center:** differential phase projection. **Right:** dark-field projection.

An important characteristic of a grating interferometer is the visibility map, which is the reference visibility image  $V_r$  (**Figure 3.7**). This image represents the strength of the interference pattern at each pixel location in the absence of any sampled object. Many factors can contribute to a reduction in the system visibility, including imaging with an x-ray energy substantially different than the interferometer's design energy. Partial transmission in the grating lamellae also contributes to a reduction in the visibility map. Partial transmission occurs when imaging with a broad spectrum where a large proportion of the applied x-rays are above the grating design energy. Cone beam effects contribute to differences in visibility at the borders of the detector area while lamellae cross-linkage and other inconsistencies in  $G_2$  contribute to local variations in the visibility map. Unique from attenuation contrast, an additional source of noise in both the differential phase and dark-field contrast images is low visibility. This source of image noise has been shown to vary

inversely with visibility in both contrasts<sup>72,73</sup>. While taller lamellae can improve visibility they come at the expense of dose efficiency and are more challenging to manufacture<sup>74</sup>. A system's visibility is commonly summarized by the mean visibility, which for this current setup is  $\bar{V}_r = 0.23$ , though this scalar value obscures any local variations in visibility.

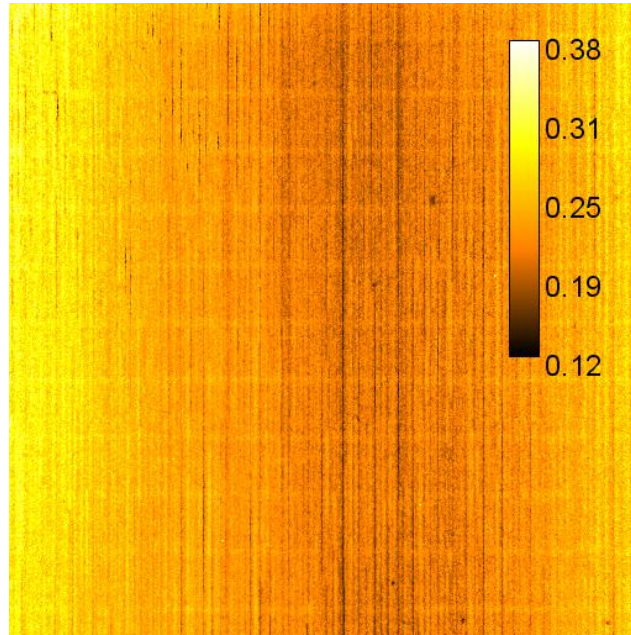


**Figure 3.7** Example visibility map acquired from the experimental Talbot-lau grating interferometer. Grating quality, grating alignment, and acquisition parameters all influence the visibility map.

### 3.4 Data Calibration and Preprocessing

Prior to performing CT image reconstruction, an additional preprocessing step is taken to account for the non-negligible scintillator decay speed of our detector (**Figure 3.8**). Such long decay speeds are characteristic of CsI(Tl) scintillators, which are optimized to maximize sensitivity at low x-ray exposure levels. When used for computed tomography, such scintillators retain residual signal from previous exposures. The contribution of each of these exposures taken at previous rotation positions and separated by time interval  $\Delta t$  decays exponentially with time. The impact on image quality is most apparent when viewed as a CT reconstructed image (**Figure 3.9a**) where this retained information effectively blurs the acquisition in the angular direction, producing circular noise textures and some loss in spatial resolution<sup>75</sup>. This blurring can be modeling as a convolution of the

input signal with a blurring kernel  $h$  (Eq. 2.16), where  $h$  is an exponential decay impulse function acting along the temporal direction between projections. For solid-state x-ray scintillators this impulse response can be modeled as a multi-exponential

$$h(t) = \sum_{n=1}^N \frac{\alpha_n}{\tau_n} U(t) e^{-t/\tau_n} \quad (3.7)$$

here  $\alpha_n$  represents the relative contribution of each exponential decay component defined by a time constant  $\tau_n$  and  $U(t)$  such that blurring only acts after  $t \geq 0$  following the impulse input

$$U(t) = \begin{cases} 1 & t \geq 0, \\ 0 & t < 0. \end{cases} \quad (3.8)$$

The constants  $\alpha_n$  and  $\tau_n$  were found for our system by fitting the following exponential

$$I(t) = \sum_{n=1}^N \alpha_n U(t) e^{-t/\tau_n} \quad (3.9)$$

to the measured decay data in **Figure 3.8**, recorded starting at  $t = 0$  immediately after turning off the x-ray source. From these constants the decay can be corrected for with the following recursive algorithm (adapted from Hsieh et al. 2000)<sup>75</sup>:

$$I'(k\Delta t) = \frac{I(k\Delta t) - \sum_{n=1}^N \beta_n e^{-\Delta t/\tau_n} S_{nk}}{\sum_{n=1}^N \beta_n}. \quad (3.10)$$

Here  $S_{nk} = I'[(k-1)\Delta t] + e^{-\Delta t/\tau_n} S_{n(k-1)}$  is the recursive term accumulating information from previous views to be subtracted away and  $\beta_n = \alpha_n (e^{-\Delta t/\tau_n})$  is a constant value characteristic of the scintillator decay rates and system sampling interval  $\Delta t$ .  $I(t)$  refers to the original projection data acquired at time  $t$ ,  $I'(t)$  are the corrected projections, and  $k$  refers to the acquisition number. For simplicity a constant sampling interval of  $\Delta t = 0.1s$  was set between sample rotation and phase step acquisitions. This correction scheme (Eq. 3.10) was applied to all raw projection data prior to phase retrieval with a representative corrected attenuation slice shown in **Figure 3.9b**. Similar to the results presented in (Hsieh et al. 2000)<sup>75</sup>, this recursive deconvolution technique (Eq. 3.10) reduces the circular noise texture at the cost of some increase in overall noise. Future steps include adding a regularization term to reduce this increase in noise.

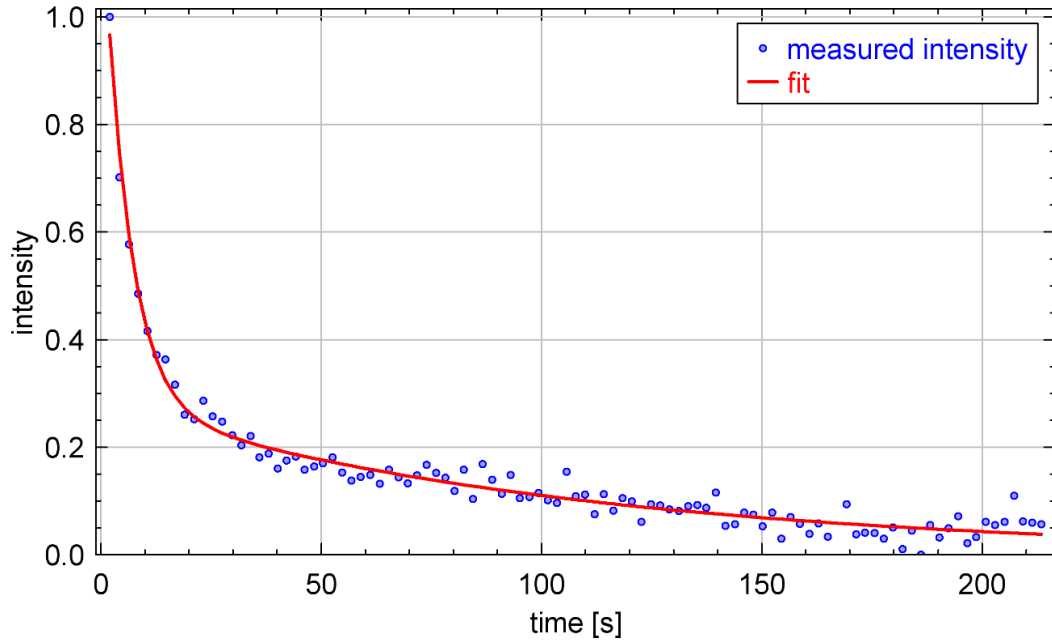


**Figure 3.8** Measured detector decay recorded immediately after turning off the x-ray source. The decay is modeled as two-part exponential with the line best fit plotted.

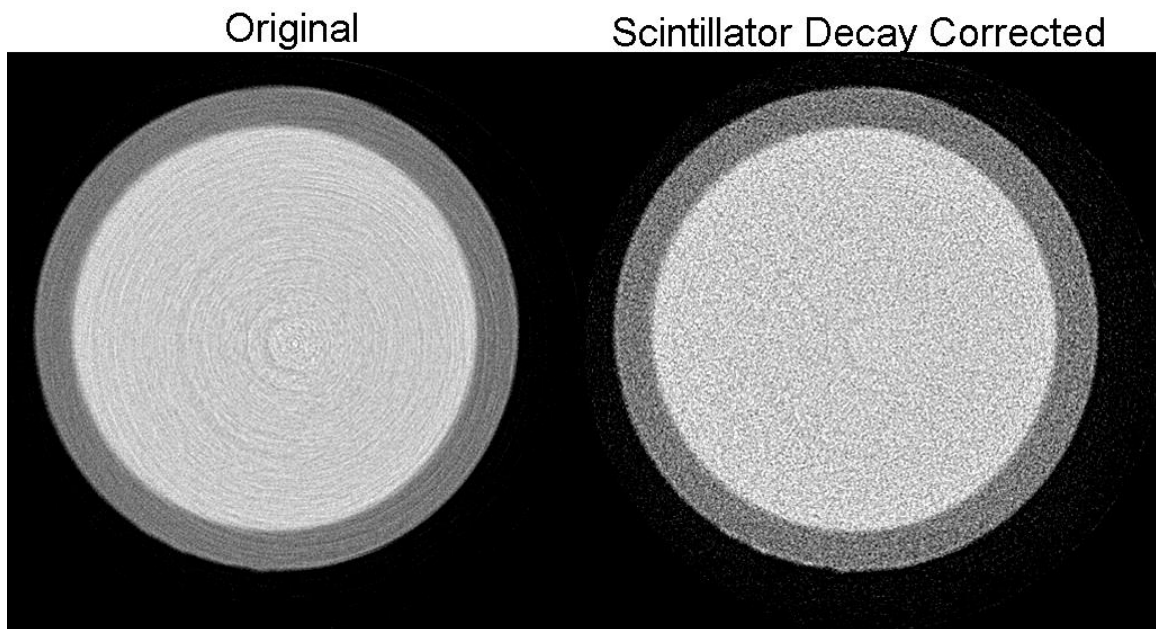


**Figure 3.9** Effect of scintillator decay on CT noise texture.

### 3.5 Image Reconstruction

Using the phase stepping and precorrection procedures described above and the beam hardening correction introduced in **Chapter 4**, tomographic datasets were then acquired by repeating the phase stepping and contrast retrieval process after applying incremental rotations of the sample stage over 182 degrees with a tube voltage of 55 kVp and current of 30 mA with 1.5 seconds of detector integration time per acquisition. A sinogram representation of this data is shown for one row of the detector as a function of rotation angle  $\theta$  (**Figure 3.10**).

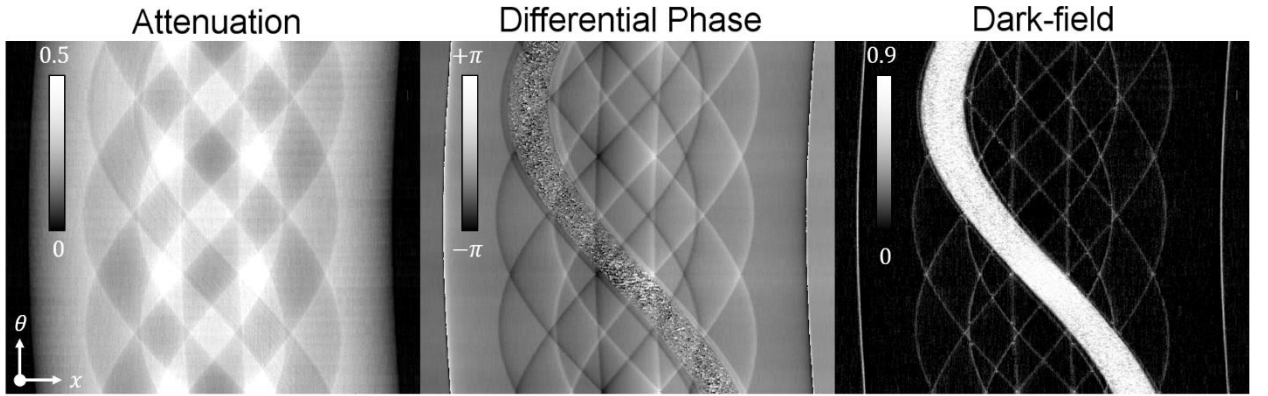


**Figure 3.10** Sinogram acquisition of three contrasts over  $\pi$  radian rotation.

These projection datasets, combined with the system geometry information including cone-angle and sample magnification described in **Section 3.2.1** were used as inputs to the Feldkamp, Davis and Kress (FDK) 3D cone-beam reconstruction algorithm<sup>76</sup> as implemented in the TIGRE CT reconstruction toolbox<sup>77</sup>. Images were reconstructed with a voxel size set to approximately equal the system spatial resolution of  $60 \mu\text{m}^3$  covering a  $30 \text{mm}^3$  FOV. Prior to CT backprojection attenuation and dark-field projections were filtered via Fourier domain multiplication with the high-pass Ram-Lak ramp filter<sup>51,61</sup>:

$$h(r) = |r|, \quad (3.11)$$

for spatial frequencies  $r$ . To account for the spatial derivative in the differential phase contrast, projections were integrated using the imaginary Hilbert filter

$$h(r) = \frac{|r|}{2\pi ir} \quad (3.12)$$

which makes use of the Fourier transform theorem for integrals, whereby multiplying  $h$  from **Eq. 3.12** with our differential phase contrast projections in the Fourier domain accomplishes both the integration and high-pass filtering in a single operation<sup>68</sup>.

The resulting three contrast reconstructions are shown in **Figure 3.11** as two axial slices, one including the wooden insert (top) and one without (bottom). In the attenuation image there is large contrast between the acrylic cylinder and hollow inserts. The wooden insert is less attenuating and thus darker than the acrylic phantom material (displayed as white) but lighter than air (shown in black), while the airspaces between the wood grains are resolvable. The combination of the gratings and the broad x-ray spectrum used leave spectral ring artifacts most noticeable here in the attenuation contrast image. More details on this process and a correction strategy are given in **Chapter 4**.

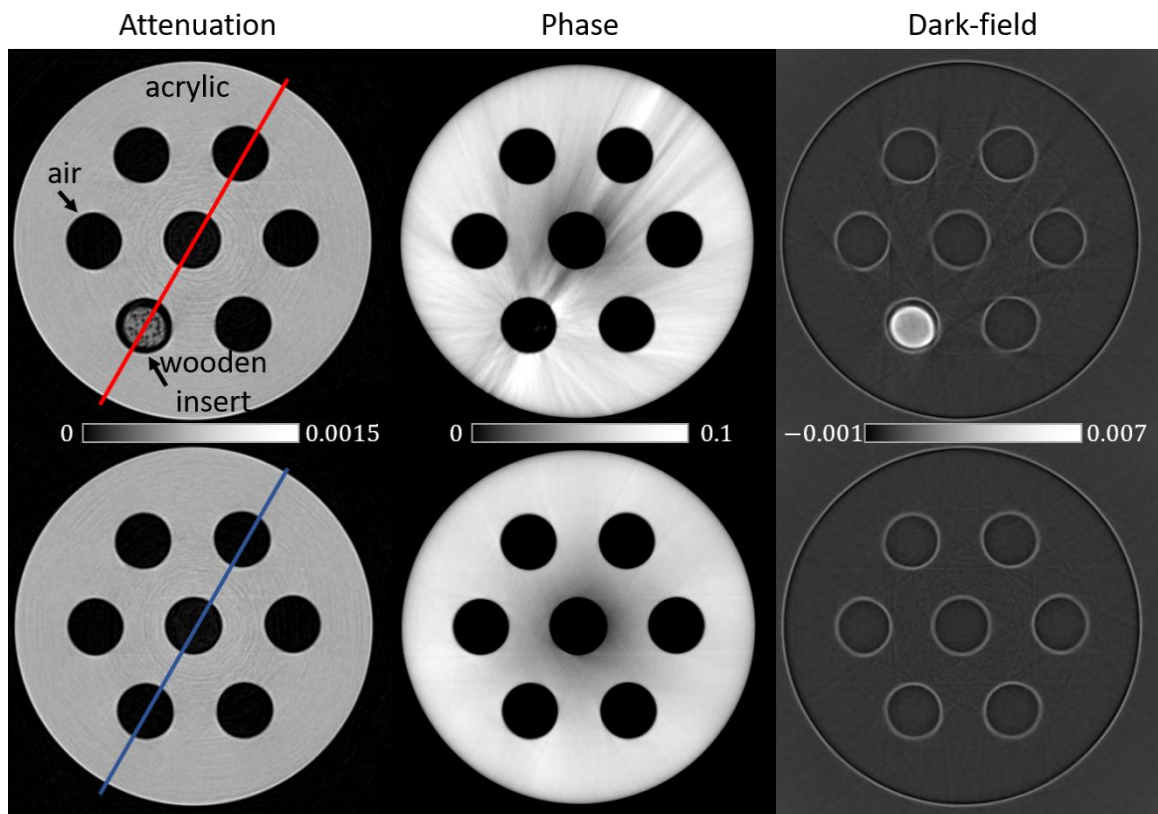


**Figure 3.11** Three contrast reconstructions from grating interferometer micro-CT of a cylindrical acrylic phantom with hollow inserts. **Left:** attenuation contrast image. Arrows indicate wooden insert (top row) and air contained in hollow portions of the phantom. **Center:** phase contrast image. **Right:** dark-field images.

Compared to the attenuation reconstruction, the phase image has a lower frequency noise texture which is more apparent when comparing line profiles between contrasts (**Figure 3.12**). This lower frequency noise is due to the integration involved in the phase reconstruction step. This gives phase images a smoother appearance but can yield low frequency signal variation as the influences of noise propagate further over the image. Such low frequency variations must be accounted for prior to using phase contrast quantitatively<sup>78</sup> as shown by the signal dip towards the center of the phase image. In addition, the loss of signal in the highly scattering wooden insert leaves the phase projections signal starved in these regions leading to streak artifacts similar to metal-induced streak artifacts in attenuation CT<sup>79</sup>.

In the dark-field image, contrast is present at material interfaces as edge-enhancing undershoots and overshoots due to dark-field's sensitivity to phase gradients<sup>41,42,66</sup>. Consistent with **Figure 3.6** and **Figure 3.10**, dark-field has the greatest contrast in the wooden insert due to the abundance of scattering interfaces and unresolved phase edges<sup>62</sup>. However, given that the visibility in this region is near zero as shown by the PSC curve in **Figure 3.5**, internal details in the wooden insert are lost as the dark-field signal is essentially saturated.

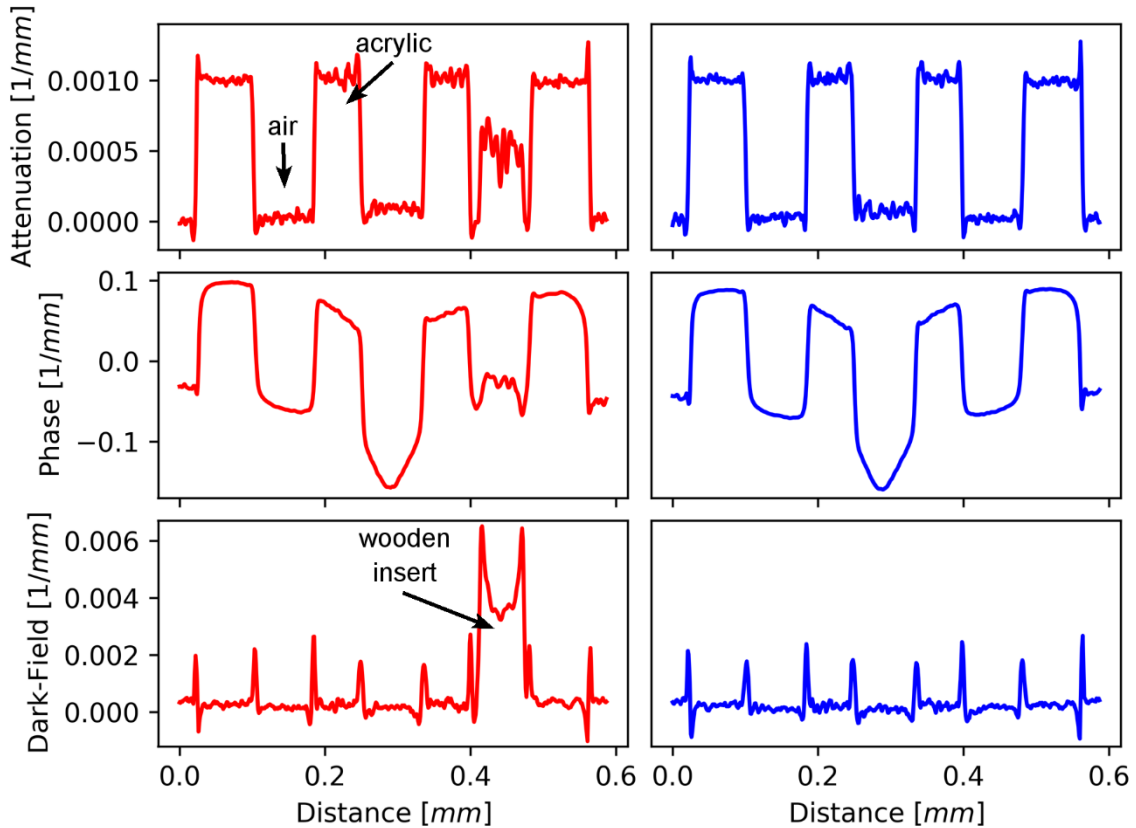


**Figure 3.12** Line profiles from three x-ray contrast reconstructions covering a wood insert and hollow inserts in an acrylic phantom. **Top:** attenuation profile. **Middle:** phase profile. **Bottom:** dark-field profile. Arrows indicate signal response from different materials in the phantom.

### 3.6 Conclusions

While the imaged materials (acrylic, air, and wood) presented in this chapter are not typically found in most biological applications, they clearly demonstrate the unique differences between the image contrasts available with grating interferometry. The remaining chapters further explore the complementary nature between these contrasts and how their combined use can be used to benefit biological applications, particularly in lung imaging.

# CHAPTER 4

---

## Beam Hardening in X-Ray Grating Interferometry

### 4.1 Introduction

The use of Talbot-Lau grating interferometry<sup>17</sup> broadens potential applications of x-ray phase-based measurements, including x-ray dark-field, by using polychromatic sources readily available in clinical and laboratory environments<sup>44</sup>. These sources feature greater tube output, which reduces scan times at the cost of biasing quantitative measurements by introducing beam hardening artifacts<sup>80</sup>. Beam hardening refers to the increase in mean energy of a polychromatic x-ray beam while passing through a sample as lower energy photons are preferentially absorbed. In addition to absorption, lower energy photons are also preferentially phase shifted (**Table 2.1**) meaning that beam hardening underestimates both attenuation and phase measurements.

As discussed in **Section 2.2.2**, x-ray absorption is described by the imaginary component  $\beta$  of the complex index of refraction  $n = 1 - \delta + i\beta$  (**Eq. 2.1**).  $\beta$  is a factor of the material's density  $\rho$  [g/cm<sup>3</sup>] and energy-dependent atomic scattering factor  $f_2$ . In attenuation imaging the linear attenuation coefficient  $\mu$  [cm<sup>-1</sup>] is thus proportional to  $\rho$  and  $f_2$

$$\mu(x, y; E) = \rho(x, y)\mu_m(E) \propto \beta(x, y; E) \frac{1}{E} \propto \rho(x, y)f_2(E) \frac{1}{E} \quad (4.1)$$

where  $\mu_m$  [cm<sup>2</sup>/g] is the material's mass attenuation coefficient<sup>44,53</sup>. Common beam hardening correction strategies leverage the ability to estimate this energy dependence by scanning a calibration object, where the expected monochromatic response is known<sup>80</sup>. From this an energy correction function can be found that will compensate for the beam hardening effects. The x-ray phase coefficient  $\eta$  can similarly be described as a factor of material density and energy-dependent  $f_1$  scattering

$$\eta(x, y; E) \propto \delta(x, y; E) \frac{1}{E} \propto \rho(x, y) f_1(E) \frac{1}{E}. \quad (4.2)$$

The separability of both attenuation and phase coefficients into energy and spatial components enables the translation of correction strategies originally developed for attenuation imaging to be used in phase contrast imaging as well.<sup>38</sup> Despite this translatability, separate corrections must be fit and applied to each image contrast mechanism to account for different energy dependencies of  $f_1$  and  $f_2$  scattering processes that underly each interaction.

X-ray dark-field has also been experimentally shown to be susceptible to beam hardening effects<sup>81</sup>. However, since dark-field signal derives from small-angle scattering which is a function of material composition and structure, it cannot be easily factored into energy and spatial components. Another complication, beam hardening has been shown to reduce visibility and thus generate dark-field<sup>40</sup>. Despite these challenges, empirical corrections have been shown to substantially reduce the impacts of beam hardening in dark-field measurements<sup>81</sup>.

In addition to the unique energy dependencies of attenuation, phase, and dark-field, nonidealities in the phase measurement device can introduce further beam-hardening-related challenges. In grating-interferometry, the most common x-ray phase measurement technique, the grating optics are a prominent source of such nonidealities due to the difficulty in manufacturing grating lamellae with sufficiently high aspect ratio for medical x-rays<sup>74</sup>. Partial transmission from insufficiently tall lamellae or lamellae cross-linking (described in **Section 3.2.2**) has been shown to harden the beam in a spatially varying manner<sup>82,83</sup>. Using the grating-interferometer introduced in **Chapter 3**, this effect is demonstrated in **Figure 4.1a** by comparing an x-ray attenuation projection of a water tube acquired before and after inserting the gratings. While the image without gratings has a relatively smooth signal profile across the sample diameter (**Figure 4.1b**), the addition of the gratings introduces heterogeneous vertical striations of reduced attenuation. Gratings with taller lamellae can reduce these partial-transmission effects, but such gratings reduce attenuation contrast-to-noise ratios<sup>74</sup>. Additionally, at higher energy applications (>80 keV, above the k-edge of gold) partial transmission may be unavoidable, inevitably

requiring algorithmic correction. Thus, there is a need for a suitable correction scheme for grating interferometry that compensates for the varying energy dependencies of each contrast mechanism while also accounting for spatial heterogeneity introduced by nonidealities in the grating optics.

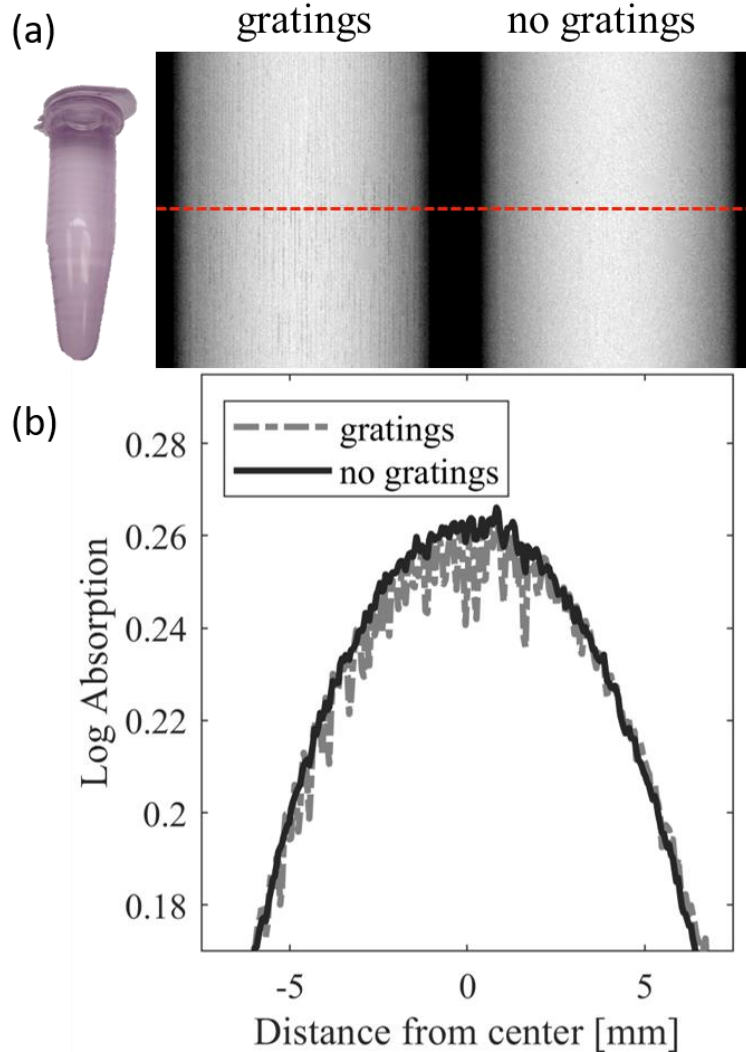


**Figure 4.1** (a) Projections of attenuation signal through a water-filled tube in the highlighted region of interest, acquired both without and with gratings. (b) Line profiles through both images.

A range of beam hardening correction strategies have been developed for grating interferometry that address some, but not all these challenges<sup>38,81,84</sup>. Early corrections accounted for the energy-dependent signal variations by using specialized calibration phantoms to appropriately scale each contrast projection to match expected values for the

given phantom geometry and composition.<sup>38</sup> Analytical methods overcome the need for phantom calibration scans, but require detailed knowledge of the source spectra and detector response and to date, have not corrected for beam hardening in the dark-field channel<sup>84</sup>.

One promising solution compensates for beam hardening artifacts from an anti-scatter grid by using x-ray images of the grid to encode the spatial dependence of the observed beam hardening artifacts<sup>63</sup>. Such a method leverages the separability of energy and spatial dependence in the sample (**Eq. 4.1**) but loosens the assumptions that energy dependence is spatially uniform in the imaging chain. Given that previous grating interferometer beam hardening corrections have lacked the ability to account for spatial variation in beam hardening, the hypothesis explained in this chapter is that this more general approach yields an accurate and computationally practical beam hardening correction suitable for translation to grating interferometry. The purpose of this work is thus to develop and experimentally validate such a correction strategy, hereafter referred to as Empirical Beam Hardening Correction for Grating Interferometry (EBHC-GI). Results using the proposed EBHC-GI method are reported for data acquired using a water sample to approximate biological samples and a silicon sample to create more severe beam hardening artifacts. Generalizability is then shown by applying the calibration coefficients obtained from a water sample to micro-CT data of a mouse lung sample. The improvement in image quality obtained support the use of this algorithm in subsequent chapters on interferometer studies of the mouse lung.

## **4.2 Methods**

EBHC-GI is a polynomial correction applied separately to each image contrast in grating interferometry where the energy dependence of each contrast is assumed to be measurable with a single calibration scan that is used to encode the spatial heterogeneity of beam hardening caused by the system gratings.

### **4.2.1 EBHC-GI**

EBHC-GI applies polynomial corrections to x-ray grating interferometer projections following Fourier phase retrieval, specifically attenuation  $A$ , differential phase  $\Delta\phi$ , and dark-field  $D$ . Polynomial corrections model the energy response function as an  $N$  degree polynomial<sup>85</sup> mapping polychromatic projections  $q$  to monochromatic projections  $p$ :

$$p = \sum_{i=0}^N c_i q^i. \quad (4.3)$$

Due to the linearity of the Radon transform (denoted by  $R$ ), the  $N + 1$  correction coefficients  $c_i$  can be found in image space by minimizing for  $\mathbf{c}$

$$\mathbf{c} = \operatorname{argmin}_{\mathbf{c}} \int d^3r w(\mathbf{r}) (\sum_{i=0}^N c_i f_i(\mathbf{r}) - t(\mathbf{r})). \quad (4.4)$$

Here  $f_i(\mathbf{r}) = R^{-1}(q^i)$  are CT images reconstructed from projections  $q^i$ ,  $t(\mathbf{r})$  is the template image free of beam hardening artifacts representing the vector of voxels  $\mathbf{r}$ , and  $w(\mathbf{r})$  is a binary mask used to exclude region boundaries sensitive to partial volume effects<sup>85</sup>.

Next, to account for the system's spatial heterogeneity of beam hardening, a variable  $M$  is introduced that represents a projection image of the x-ray optics encoding the spatial heterogeneity of the system's energy response<sup>63</sup>

$$p = \sum_{i,j} c_{i,j} q^i M^j. \quad (4.5)$$

Here  $q^i M^j$  are the reconstructed monomial images generated via elementwise multiplication of projections  $q$  and optics projections  $M$  followed by exponentiation to the powers  $i$  and  $j$ .

Finally, to account for the unique energy response of each image contrast in grating interferometry, EBHC-GI is completed by applying **Eq. 4.5** separately to each contrast projection as indicated by the subscript  $k$ ,

$$p_k = \sum_{i,j} c_{k,i,j} q_k^i M_k^j. \quad (4.6)$$

Like **Eq. 4.4** correction coefficients  $c_{k,i,j}$  are solved for in image space but are determined separately for each contrast  $k$  all from a single interferometer CT scan of the calibration object,

$$\mathbf{c}_k = \operatorname{argmin}_{\mathbf{c}_k} \int d^3r w_k(\mathbf{r}) (\sum_{i,j} c_{k,i,j} f_{k,i,j}(\mathbf{r}) - t_k(\mathbf{r})). \quad (4.7)$$

Here,  $f_{k,i,j}$  represents the reconstructed monomials  $f_{k,i,j}(\mathbf{r}) = R^{-1}(q_k^i M_k^j)$  of the calibration object and  $t_k$  the target monochromatic image for each contrast  $k$ .

The template images  $t_k$  from **Eq. 4.7** represent the idealized image for the chosen calibration object free of beam hardening artifacts for each contrast. This calibration object should consist of primarily the material to be corrected for in mostly large homogenous regions, for example a water container of appropriate size when imaging biologic samples. As beam hardening artifacts in grating interferometry can include both cupping effects as well as ring artifacts due to the spatial nonuniformity of beam hardening from the gratings, a combination of median filtering followed by segmentation can be used to approximate the desired uniform response. In particular for the attenuation and phase templates ( $t_A$  and  $t_{\Delta\phi}$ ) the ideal responses were estimated using Otsu's method<sup>86</sup> to segment the original reconstructed image for each contrast, then replacing all values within the segmented region with the region's median value. By replacing voxels with the median value, large fluctuations from ring artifacts do not strongly influence the desired template value. However, severe cupping may still underestimate the true value. In determining the template dark-field image  $t_D$  the beam-hardening-free template assumes no contrast in homogenous regions, thus their constant value is set equal to that of air. A final step is to record the minimum and maximum calibration values along with the correction coefficients such that when applying the correction technique only projection values that fall within the calibration range are updated to avoid spurious changes<sup>85</sup>.

#### 4.2.2 Determining the System Spatial Heterogeneity Term $M_k$

In EBHC-GI,  $M_k$  from **Eq. 4.6** encodes the spatial heterogeneity of beam hardening from all three gratings as viewed by each image contrast  $k$ . Assuming this spatial heterogeneity is constant over the duration of a CT acquisition, these biases are reflected as ring artifacts

which in a cone-beam imaging system can vary substantially between slices. This variation is recorded in measurements of  $M_k$  for a given system which can then be used to compensate for the rings. For attenuation and phase,  $M_A$  and  $M_\phi$  are best approximated by their respective grating images, the unnormalized reference air images  $a_{0,r}$ ,  $\phi_{1,r}$  (**Figure 4.2**). These grating images are found by retrieving attenuation  $a_{0,r}$  (**Eq. 3.2**), phase  $\phi_{1,r}$  (**Eq. 3.3**), and visibility  $V_{1,r}$  (**Eq. 3.4**) signal images from phase stepping curves (PSCs) acquired without any sample and represent the reference system response for each signal. Any residual artifacts from the gratings following standard phase retrieval are the result of structures in these images not being adequately canceled in the normalization process.

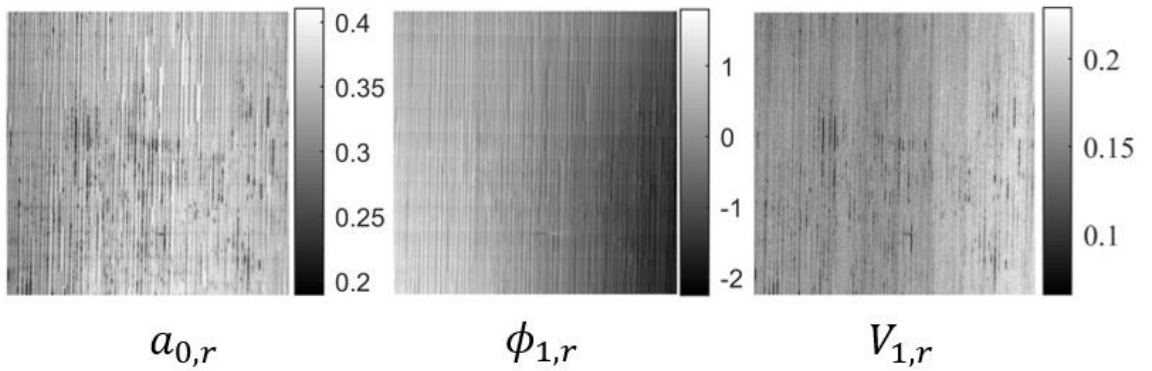


**Figure 4.2** Reference Fourier coefficient images serve as grating images to show underlying grating structure viewed in all three contrasts.

Determining  $M_D$  for dark-field is complicated by the inability to fully separate the energy and spatial dependencies, so  $M_D$  must be determined empirically from projections of the calibration object<sup>81</sup>. To accomplish this, repeat projections of the calibration object were averaged to obtain low noise projections showing grating-induced spectral artifacts. This enabled low-noise comparisons of how artifacts in visibility projections correlated with the visible grating structures in the grating images, quantified using the Pearson correlation coefficient magnitude  $|r|$ . The correlation magnitude  $|r|$  was used to account for contrast reversals between the air scans and projections. For a given sample material the dark-field spatial modulating term  $M_D$  was found to be the reference image (ref =  $a_{0,r}$ ,  $V_{1,r}$ , or  $\phi_{1,r}$ ) that best correlates with the grating artifacts in the calibration object dark-field projection:

$$M_D = \operatorname{argmax}_{\text{ref}} |r_{D,\text{ref}}|. \quad (4.9)$$

A similar approach to finding the spatial modulating terms  $M_k$  would be to solve **Eq. 4.7** determining coefficients  $\mathbf{c}_k$  for each contrast  $k$  and reference image for  $M_k$  and selecting the combination that yields the best correction as determined by the criteria described in **Section 4.2.5**. We argue, however, that the above approach of using low-noise projections and comparing correlations yields the same results while requiring fewer exposures and image reconstructions. We confirm this approach by determining the normalized visibility modulating term  $M_V$  using both described methods.

Each step of EBHC-GI has been summarized in **Figure 4.3** which starts with data acquisition and multi-contrast projection retrieval. These different sample and reference contrast projections are used to make the monomial projections. The polynomial coefficients used to linearly combine these monomial projections are determined from fitting the monomial image reconstructions against a calibration phantom image reconstruction with the desired beam-hardening free response. These coefficients are then used to correct all future projections.

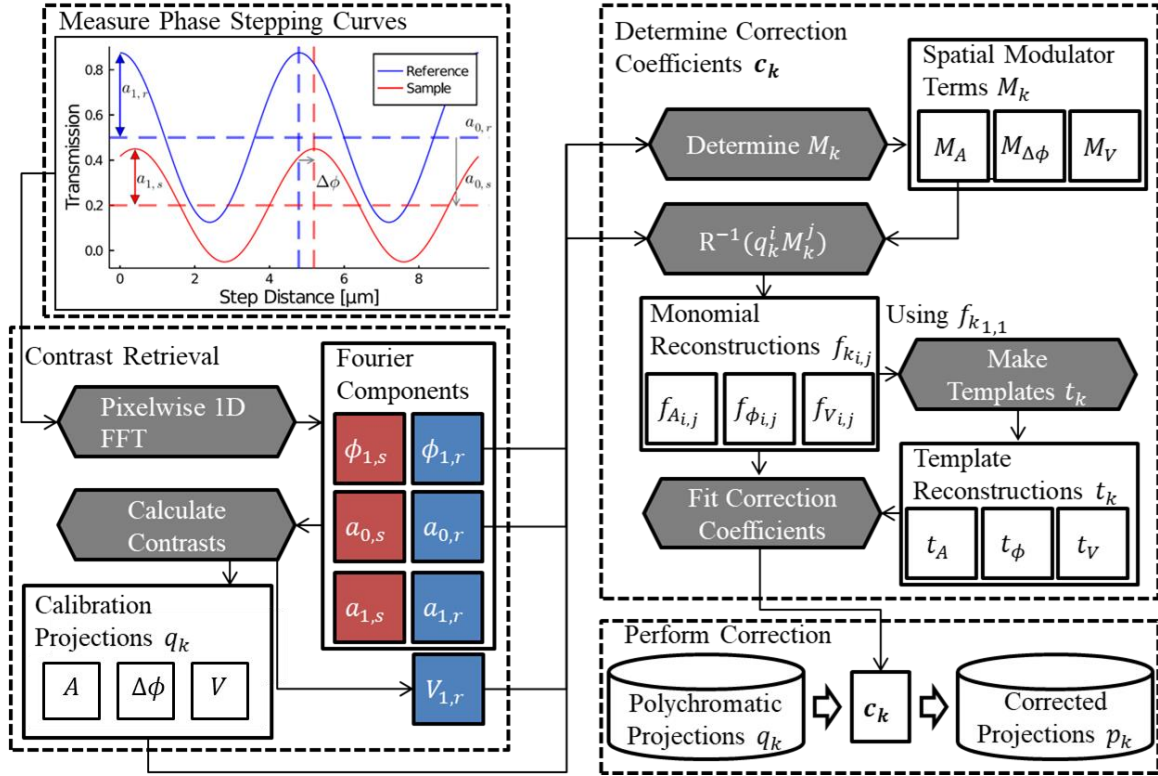


**Figure 4.3** Overview of processing steps involved in EBHC-GI. Three contrast calibration projections  $q_k$  retrieved from phase stepping curves acquired of a calibration object with a known homogenous region are used to fit correction coefficients for each contrast  $c_k$  that are used to correct future projections of similar materials.

### 4.2.3 Sample Preparation

Three samples were evaluated in this study: a water tube representing a low atomic number material (**Figure 4.4**), a silicon tile representing a higher atomic number material (**Figure 4.4b**), as well as an *ex vivo* mouse lung (**Figure 4.4c**) to demonstrate generalizability of the water coefficients to a biological sample. The water tube was a 1.5 mL Eppendorf snap tube filled with tap water. The silicon (Z=14) tile used was the lower portion of the axial spatial resolution module contained in a QRM micro-CT bar pattern phantom.<sup>87</sup> The dotted inset image of **Figure 4.4b** shows the edge on view of the tile from the perspective of the detector. The spatial resolution module in the phantom is etched into the top 100  $\mu\text{m}$  of a 500  $\mu\text{m}$  thick silicon tile. However, for this study we used the remaining 400  $\mu\text{m}$  thick un-etched silicon region to evaluate the performance of the proposed method in a sample generating more severe beam hardening artifacts. Finally, the mouse lungs used were excised from an *ex vivo* sample (see **Chapter 5** for more details).

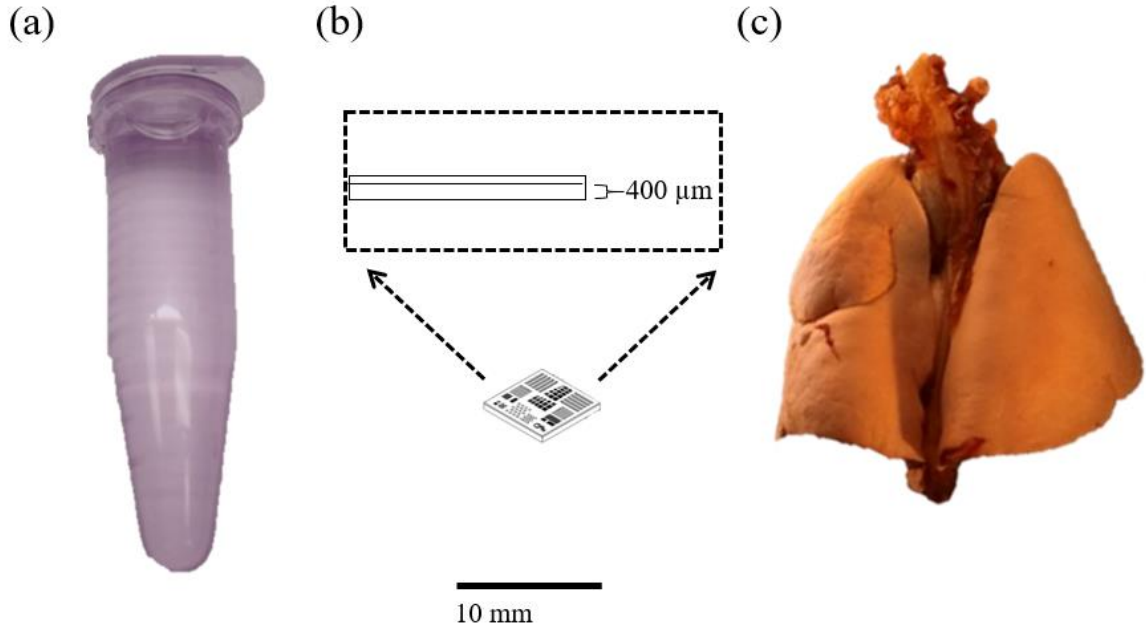


**Figure 4.4** Imaged samples shown to scale include (a) 1.5 mL snap tube filled with water, (b) QRM micro-CT bar pattern phantom schematic<sup>87</sup>. The inset shows an enlarged view of the chip and the edge-on orientation used to acquire images. The lower 400  $\mu\text{m}$  silicon region was used exclusively in this study. (c) Posterior view of excised mouse lung with heart following fixation and air drying at end-exhalation inflated volume.

#### 4.2.4 Data Acquisition and Image Reconstruction

Sample and reference phase stepping curves (subscripted  $s$  and  $r$  in **Figure 4.3**) were generated by the phase stepping of  $G_1$  over a single period of  $G_1$  in six steps of 1.5 seconds each for a total of 9 seconds per view angle. Projection data of the three contrasts were then retrieved using the Fourier method<sup>56</sup>. In our experimental setup mean reference visibility was measured to be  $V_{1,r} = 16.4\%$ . Using the aforementioned phase stepping and retrieval procedure, water, silicon, and mouse lung samples were positioned with a source-to-object distance of  $d_{\text{SO}} = 710$  mm and object-to-detector distance of  $d_{\text{OD}} = 110$  mm to perform CT. All CT acquisitions were performed over a full 360-degree range such that any ring artifacts would be presented as full rings. Due to the rotational symmetry of the water cylinder projection data were acquired every 2 degrees, while projections of both the silicon tile and fixed lung were acquired every 0.5 degrees. Images were then reconstructed into  $512 \times 512$  matrix slices of  $47 \mu\text{m}$  isotropic voxels using the FDK algorithm<sup>76</sup>. In order to minimize image noise when determining correction coefficients, both the water cylinder and silicon tile images were reconstructed with TIGRE's Hamming filter while lung

images were reconstructed with a Ram-Lak filter appropriate for the high frequency features in the lungs<sup>77</sup>.

#### 4.2.5 Evaluation of EBHCI-GI

The performance of our correction was quantified in terms of a reduction in the mean squared error (MSE) between the corrected and template images:

$$MSE = \frac{1}{n} \sum_i^n (e_i)^2, \quad (4.10)$$

where  $e = P_k(\mathbf{r}) - t_k(\mathbf{r})$  is the  $n$  voxels difference image between the template image  $t_k(\mathbf{r})$  and the corrected image  $P_k = R^{-1}(p_k)$  reconstructed using EBHC-GI corrected projections  $p_k$ . Standard deviation measured in a central homogenous region of each sample image was used as a secondary measure of artifact reduction. These values were then used to compare the uncorrected and corrected images for each contrast. Line profile comparisons were also performed to visually compare the uncorrected, corrected, and template images.

Finally, to assess the generalizability of the coefficients to similar materials we concluded our investigation by applying the coefficients determined from the water sample on the mouse lung sample. Performance was assessed qualitatively for each contrast by visual inspection of uncorrected, corrected, and subtraction images.

### 4.3 Results

#### 4.3.1 Determining the System Spatial Heterogeneity Term $M_k$

The spatial heterogeneity term for dark-field  $M_D$  in EBHC-GI was determined for two calibration objects of different materials by assessing which grating image best correlated with the observed beam hardening artifacts. These correlations between the system grating projections and sample projections are shown for both water and silicon calibration samples as a bar chart in **Figure 4.5**. Correlations of grating images with attenuation and differential phase projections are shown for comparison. Stars indicate correlations that were significant, defined as a p-value  $< 0.05$ . For each image contrast the correlation of the sample projection ( $A$ ,  $\Delta\phi$ , and  $D$ ) is computed with each grating image ( $a_{0,r}$ ,  $\phi_{1,r}$ ,  $V_{1,r}$ ) and

depicted as a differently shaded bar. For example, the black bar in the group of three bars for attenuation contrast refers to the correlation  $|r_{A,a_{0,r}}|$ .

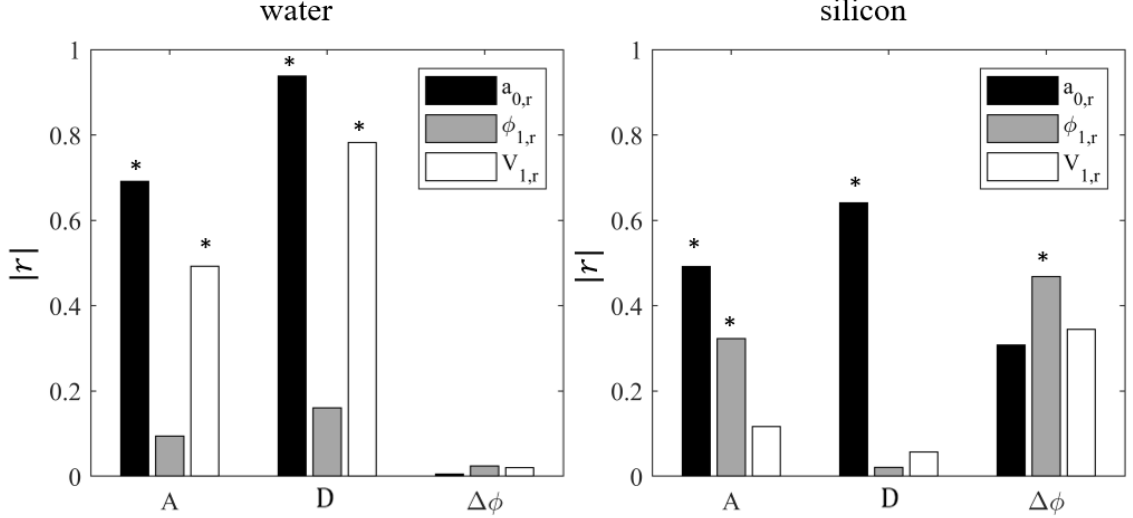


**Figure 4.5** Pearson correlation coefficient magnitudes  $|r|$  between sample and air grating projections for both the water and silicon samples. \*indicates  $P < 0.05$ .

Consistent with expectations, the correlation of artifacts in the attenuation and differential phase contrast projections were highest with their respective attenuation and differential phase grating images for both the water and silicon samples. This validates the choice of  $M_A = a_{0,r}$  and  $M_{\Delta\phi} = \phi_{1,r}$  in both samples based upon **Eq. 4.9**. While no correlation was found to be significant for differential phase in the water calibration sample, these findings are consistent with our observation that artifacts were absent in the water differential phase projections, indicating a minimal  $M_{\Delta\phi}$  contribution to the correction.

In empirically determining  $M_D$  for dark-field, we observed  $|r_{D,a_{0,r}}| > |r_{D,V_{1,r}}|$  in both sample materials, suggests that  $M_D = a_{0,r}$  for both water and silicon calibrations. This provides further evidence of cross-contamination of attenuation and phase information into the visibility contrast, an effect previously reported in experimental studies<sup>42</sup>.

### 4.3.2 Evaluation of EBHC-GI in Water

Using the  $M_k$  grating terms determined for water, fit coefficients for the water sample were determined using the original and template images shown in **Figure 4.6**. In the water

sample, 2<sup>nd</sup> degree polynomial coefficients were determined for both variable dimensions resulting in 9 total coefficients for each contrast. The choice of 2<sup>nd</sup> degree polynomials for the water sample was determined empirically to best remove spectral artifacts with no substantial improvement observed by adding higher polynomial terms.

**Figure 4.7** then compares the resulting images reconstructed from uncorrected projections and EBHC-GI corrected projections. Line profile comparisons including the template image are included in **Figure 4.7c**. The measured MSE and standard deviation averaged over 30 central slices containing ring artifacts are presented in **Table 4.1**. In all three contrasts there was little evidence of cupping artifacts suggesting a limited influence of beam hardening from the water tube due to its small size and lower atomic number. However, the presence of ring artifacts in the attenuation contrast reflects the spectral nonuniformity from the gratings observed quantitatively as an elevated MSE and standard deviation reported in **Table 4.1**. Of note, these ring artifacts are strongly suppressed following the application of EBHC-GI where the attenuation MSE was decreased by 80% and standard deviation by 57%. In the dark-field channel, the influence of beam hardening is not obvious. Despite this, we measured a 65% reduction in the dark-field standard deviation following correction using  $M_D = a_{0,r}$  compared to only a 58% reduction using  $M_D = V_{1,r}$  with comparable reductions in MSE in both cases.

The presented images and measured results are representative of typical slices in the reconstructed volume containing spectral ring artifacts. In EBHC-GI  $M_k$  controls the local ring artifact correction, and as a result slices containing rings experience a reduction in MSE and standard deviation following EBHC-GI correction, whereas slices without prominent rings are left largely unchanged. Similar observations were made in the differential phase contrast images where spectral artifacts were visually undetectable in the original images. Thus, the original and corrected images were indistinguishable with a correspondingly small reduction in MSE and standard deviation.

These results suggest that for our given system in water, the attenuation contrast is most strongly influenced by beam hardening and, in this low-Z imaging task, benefits most from EBHC-GI in terms of ring artifact reduction as quantified by a reduction in MSE from the

template and reduced standard deviation. Additionally, the improvements observed in water for the attenuation and visibility images also suggest that beam hardening affects intensity-like features of the phase stepping curve ( $a_0$  and  $a_1$  Fourier coefficients) more than the phase term ( $\phi_1$ ).

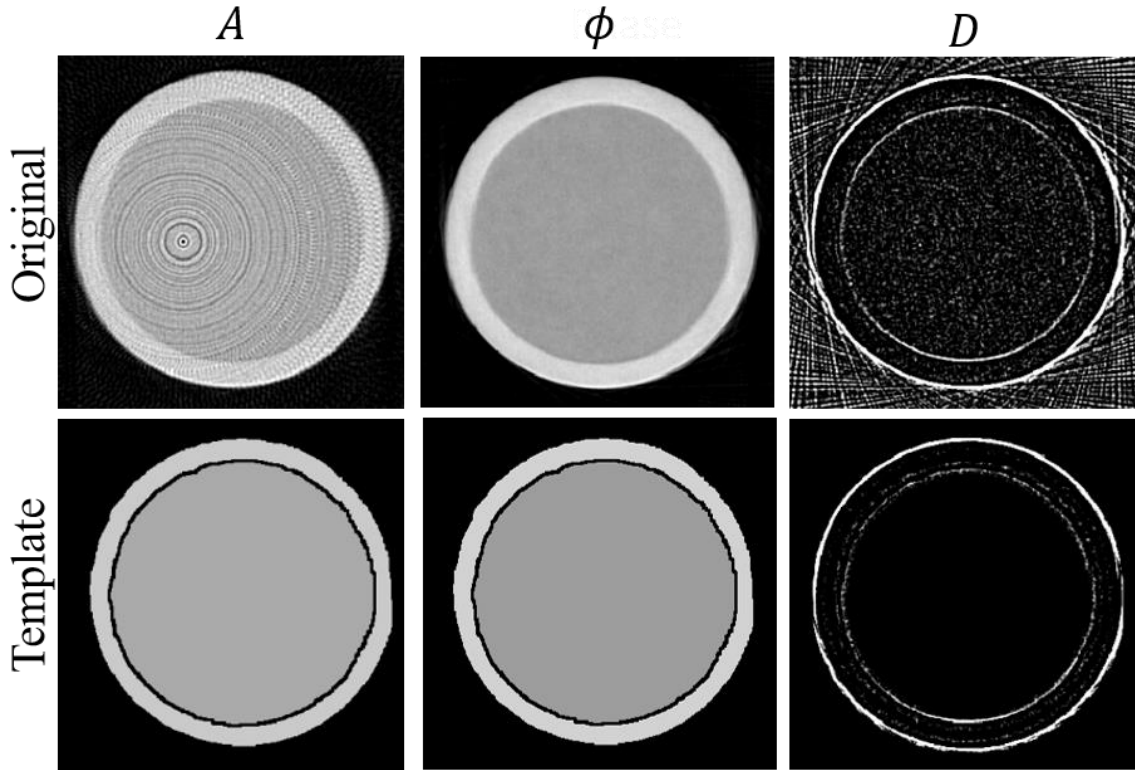


**Figure 4.6** Uncorrected reconstructions and artifact-free templates of the water sample for attenuation  $A$ , phase  $\phi$ , and dark-field  $D$  contrasts.

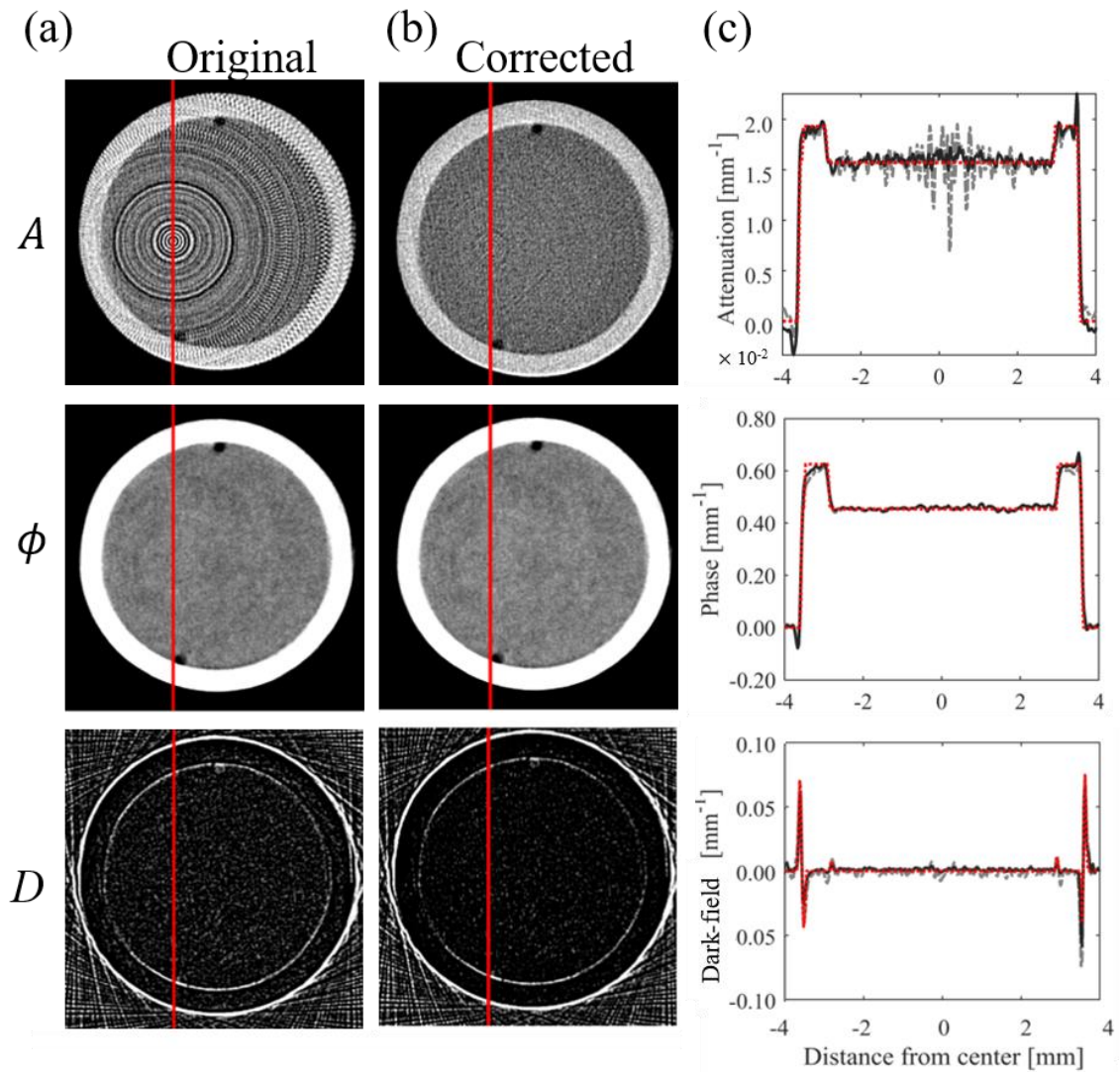


**Figure 4.7** Water sample reconstructions for each contrast with the original uncorrected axial image **(a)** shown left of the EBHC-GI corrected slice **(b)**. The image display settings for each contrast are determined from the uncorrected image with a level equal to the image mean and window width of four standard deviations. **(c)** Line profiles that correspond to the columns of pixels marked in red in **(a)** and **(b)** compare original (dashed gray), corrected (solid black), and template (dotted red) line profiles.

**Table 4.1** Beam hardening correction results for water quantified in terms of mean squared error (MSE) from template  $t$  and standard deviation (Std dev) within the homogenous water region.

Attenuation		
Image	MSE	Std dev
Original	$1.33 \times 10^{-6}$	$1.15 \times 10^{-3}$
Corrected	$2.61 \times 10^{-7}$	$4.85 \times 10^{-4}$
<b>Change</b>	-80.37%	-57.83%
Phase		
Image	MSE	Std dev
Original	$3.83 \times 10^{-5}$	$6.02 \times 10^{-3}$
Corrected	$3.63 \times 10^{-5}$	$5.86 \times 10^{-3}$
<b>Change</b>	-5.22%	-2.66%
Dark-field		
Image	MSE	Std dev
Original	$7.58 \times 10^{-6}$	$2.60 \times 10^{-3}$
Corrected	$2.49 \times 10^{-6}$	$8.86 \times 10^{-4}$
<b>Change</b>	-67.15%	-65.92%

### 4.3.3 Evaluation in Higher Atomic Number Materials

Using correction coefficients  $c_k$  determined for silicon, image, and line profile comparisons for each contrast from the original and corrected silicon sample projections are shown in **Figure 4.8** with MSE and standard deviation values reported in **Table 4.2**. For the higher atomic number silicon sample, 3<sup>rd</sup> degree polynomial coefficients were determined for each variable yielding 16 coefficients per contrast. The additional polynomial terms were found to further improve artifact reduction over the 2<sup>nd</sup> degree polynomial used with the water sample. Such results are plausible given the higher atomic number of silicon and hence greater degree of beam hardening. In the silicon tile images, all contrasts presented more severe artifacts than in water, with rings in each contrast, cupping in phase, and capping in the normalized visibility images. Furthermore, all three contrasts saw over 90% reductions in MSE following correction. These results are an improvement over using the visibility reference  $V_{1,r}$  for  $M_D$  which resulted in only an 88.2% reduction in MSE and 40% reduction in standard deviation from the uncorrected image. Both values are less than the 90% and 51% reductions reported in **Table 4.2** for dark-field using  $M_D = a_{0,r}$ , confirming the correlation analysis conclusions for silicon in **Figure 4.5**.

Compared to the reductions in MSE observed in the water sample following EBHC-GI, the reductions observed with the silicon sample were greater for all contrasts. This is in part due to the greater severity of spectral artifacts in the higher Z silicon sample but was also influenced by our use of MSE to quantify both ring and cupping artifacts. Ring artifact severity decreases sharply away from the image center while cupping severity does so to a lesser degree, resulting in more voxels being affected by cupping thus influencing our results to have greater MSE for cupping over ring artifacts. In addition, despite having a greater reduction in MSE and standard deviation, we observed more residual ring artifacts in the silicon sample compared to the water sample. This was a consequence of the silicon sample inducing more beam hardening and thus making the correction more challenging. Finally, the presence of spectral artifacts for all three contrasts in the silicon sample differs from our observations in the water sample, where spectral artifacts were primarily present for only the attenuation and visibility contrasts. This suggests a material and contrast dependence for spectral artifacts.

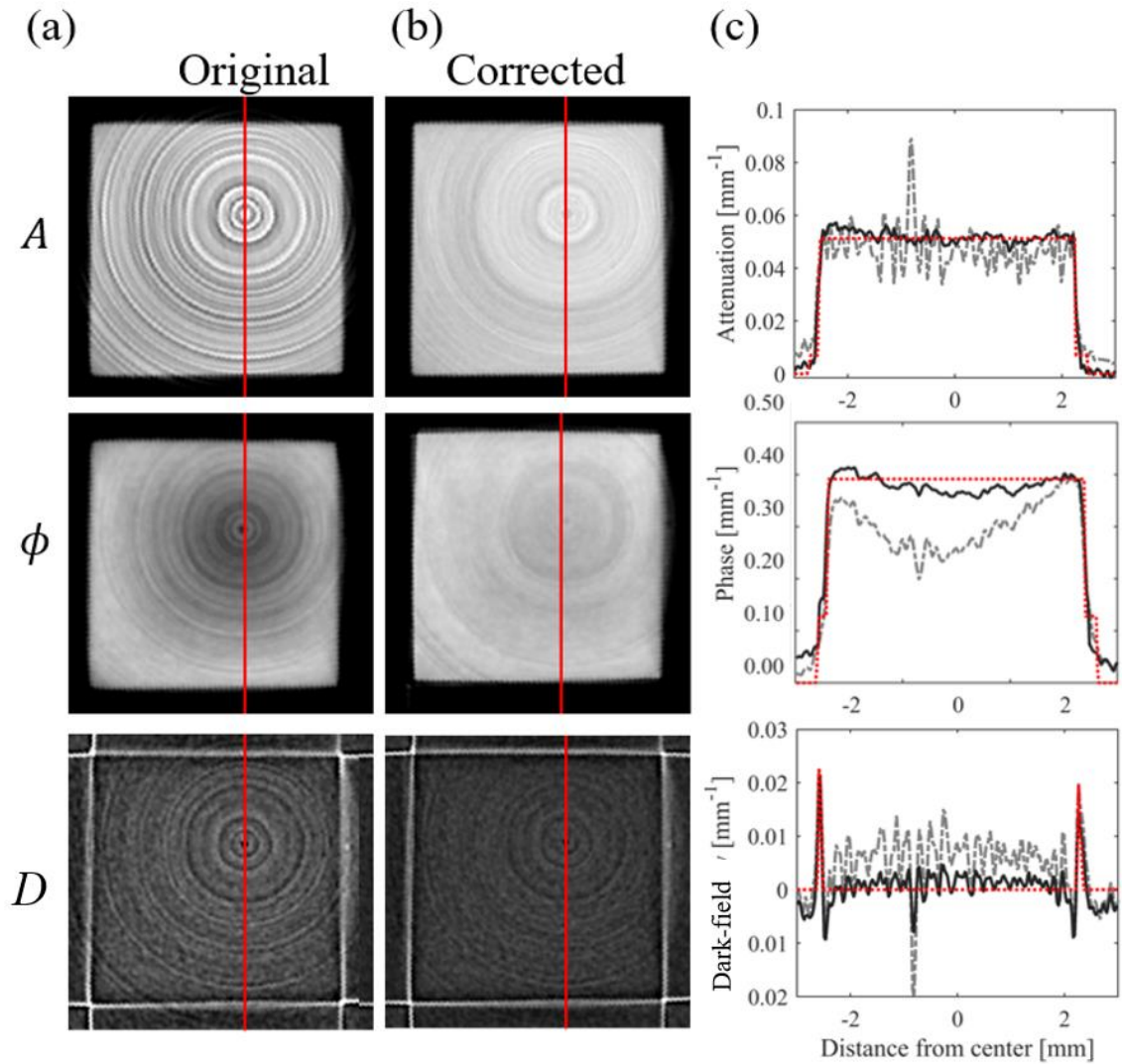


**Figure 4.8** Silicon tile reconstructions of attenuation, phase, and dark-field contrasts. Uncorrected images (a) are shown to the left of EBHC-GI corrected slices (b). The image display settings for each contrast are determined from the uncorrected image with a level equal to the image mean and window width of four standard deviations. (c) Line profiles that correspond to the columns of pixels marked in red in (a) and (b) compare original (dashed gray), corrected (solid black), and template (dotted red) line profiles.

**Table 4.2** Beam hardening correction results for silicon quantified in terms of MSE from the template and standard deviation of values within the homogenous silicon region.

<b>Attenuation</b>		
<b>Image</b>	<b>MSE</b>	<b>Std dev</b>
Original	$6.76 \times 10^{-5}$	$5.61 \times 10^{-3}$
Corrected	$4.06 \times 10^{-6}$	$1.94 \times 10^{-3}$
<b>Change</b>	-94.01%	-65.24%
<b>Phase</b>		
<b>Image</b>	<b>MSE</b>	<b>Std dev</b>
Original	$8.30 \times 10^{-3}$	$3.62 \times 10^{-2}$
Corrected	$2.67 \times 10^{-4}$	$1.17 \times 10^{-2}$
<b>Change</b>	-96.78%	-67.68%
<b>Dark-field</b>		
<b>Image</b>	<b>MSE</b>	<b>Std dev</b>
Original	$5.15 \times 10^{-5}$	$3.38 \times 10^{-3}$
Corrected	$4.65 \times 10^{-6}$	$1.65 \times 10^{-3}$
<b>Change</b>	-90.97%	-51.18%

#### 4.3.4 Lung Imaging Application

To demonstrate the generalizability of the correction coefficients found in the water calibration object as demonstrate the applicability to imaging biomedical specimens, a set of fixed *ex vivo* mouse lungs were imaged and processed with EBHC-GI. The original and corrected images of the mouse lung specimen are shown approximately midway through the mediastinum alongside difference images in **Figure 4.9**. Like observations in the water sample, the most noticeable artifacts were the rings in the original attenuation image, which were effectively eliminated in the corrected series. Examining the attenuation difference images shows the rings removed from the original with some faint residual anatomical features. These features were not lost in the corrected image, but their signal values were changed slightly, which is a consequence of EBHC-GI acting on materials different from the calibration material. However, given that materials in this mouse sample are like water, these differences were small. In the corrected phase contrast images, there were no prominent rings in the uncorrected images and thus images are mostly unchanged following correction. The difference image does reveal subtle signal changes like those described for the water sample. While the image texture differs from the attenuation difference image, this is because EBHCI-GI is applied to differential phase contrast prior to the integration step and thus these local differences are spread out to some extent. In the dark-field images, there was evidence of removed rings as well as non-edge signal changes

in the difference image, which is again due to EBHC-GI subtly shifting signal values for materials absent in the calibration object. Together, our results in the mouse lung sample were consistent with those seen in the water phantom that the attenuation contrast was most susceptible to grating induced ring artifacts, but that they could be effectively removed using EBHC-GI.

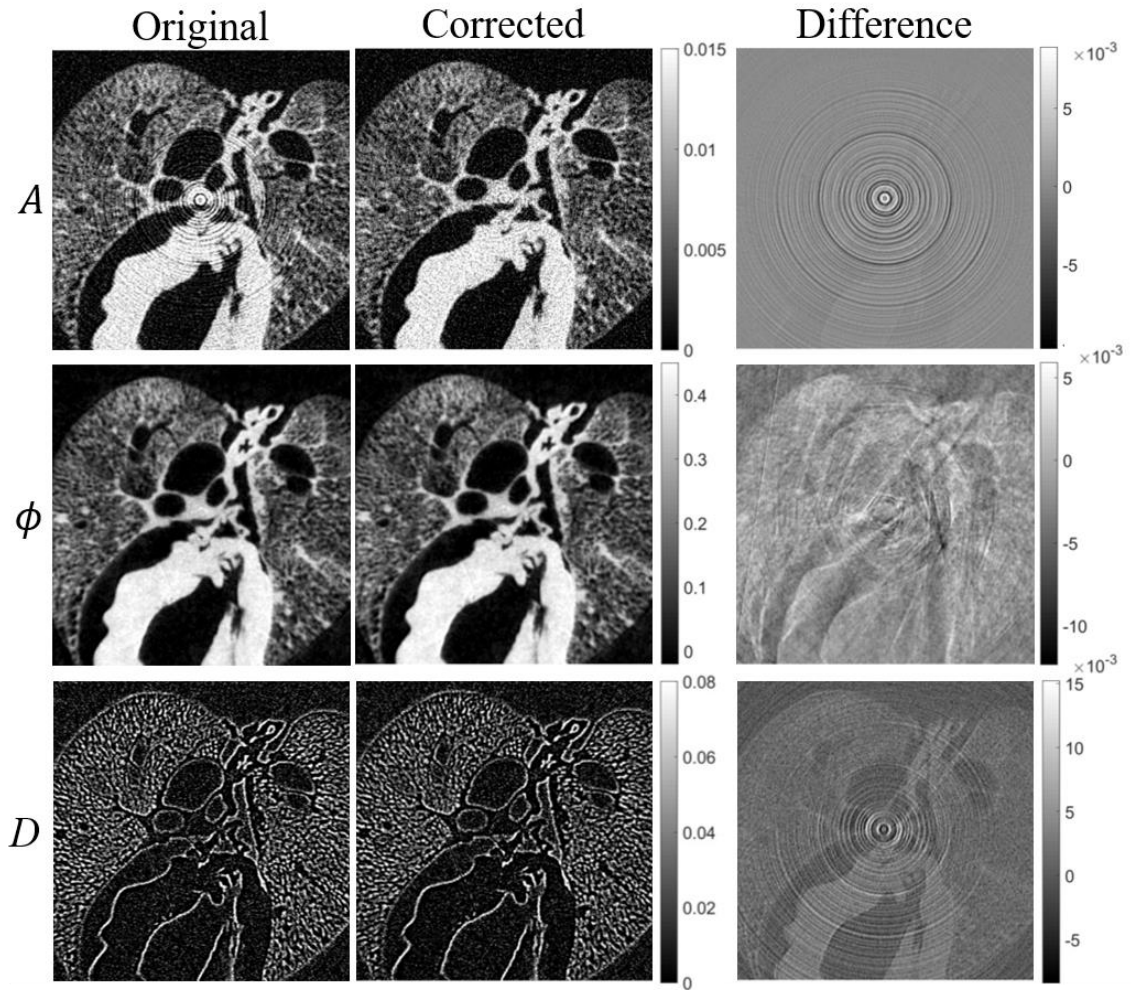


**Figure 4.9** Axial mouse lung reconstructions in prone position show the heart, large airways, and lung parenchyma. Attenuation, phase, and dark-field contrast images are shown both before and after corrections along with a difference image. The display settings are set equal for both corrected and uncorrected sets.

## 4.4 Discussion

The key findings from our study are that beam hardening artifacts in grating-based x-ray phase contrast imaging can be largely suppressed with EBHC-GI, a two-variable polynomial correction to each of the derived contrasts. Specifically, the two-variable approach includes both sample projections and grating projections in each contrast to correct for both cupping and capping artifacts derived from beam hardening in the sample as well as spectral artifacts from the gratings. EBHC-GI demonstrates a successful translation of a beam hardening correction originally developed for managing beam hardening artifacts from anti-scatter grids in cone beam CT made possible by the loosened assumption that the system's energy dependence can be spatially nonuniform<sup>63</sup>. Key changes included applying the polynomial correction separately for each contrast mechanism to account for the different energy dependencies of the different contrast mechanisms and using projections of the system gratings to encode spatial heterogeneity. We also showed methods to best determine this grating-term for dark-field contrast which is influenced by both the imaging system and sample requiring it to be determined empirically.

In determining the spatial heterogeneity term for dark-field  $M_D$  we found for both materials studied that the dark-field sample projections had the highest correlation with the attenuation grating projections. These observations of system and material dependencies of grating-induced artifact in the dark-field contrast are consistent with previous work that showed similar influence of attenuation and phase information in polychromatic dark-field measurements<sup>81</sup>. This known mixing of contrasts also suggests that further improvements to EBHC-GI could be made by considering  $M_D$  to be a weighted sum of grating images to better reflecting this intercedence. The cross-contamination between the three contrast mechanisms that occurs due to beam hardening is but one of several sources of bias in normalized visibility imaging present in grating based laboratory setups<sup>40-42,67</sup>. Ultimately, to perform better quantitative studies<sup>61</sup> of the small-angle-scattering and sub-resolvable structural information contained in the dark-field, these systematic influences must be understood and accounted for.

After determining the grating terms  $M_k$  and applying our found fit coefficients for each contrast and material, our results further demonstrated the benefit of applying a unique set of correction coefficients for each contrast. We saw this in varying contributions of cupping and ring artifacts between materials and contrasts. The uncorrected water attenuation image suffered most from grating-induced ring artifacts and needed a strong correction, whereas the phase image required minimal correction. In the silicon tile we observed an even greater divergence of artifacts between the three contrasts. The silicon attenuation image presented severe ring artifacts with modest cupping, while the phase image had more severe cupping. Finally, the silicon dark-field image had modest cupping and rings. In both samples studied, these results suggest a material and contrast dependence on the observed beam hardening artifacts, a dependence consistent with previous findings<sup>38,82</sup>.

We then demonstrated the generalizability of correction coefficients found in a water sample to remove ring artifacts when applied to an *ex vivo* mouse lung sample supporting the use EBHC-GI in further investigations involving lung specimens. A limitation of our lung sample in evaluating the performance of EBHC-GI was that the ribcage and other natural boney anatomy surrounding the lungs were not retained following excision for fixation. Thus, our lung image results do not show the typical shadowing that occur around bone because of beam hardening. While a pre-reconstruction linearization technique calibrated with a water sample would partially compensate for this shadowing, if the materials to be imaged were known ahead of time, those materials could be included in the calibration phantom to increase the effective range of materials to be corrected. For imaging objects with large proportions of both low and higher atomic number materials, say largely boney anatomy, a multi-step approach may be required. Post-reconstruction iterative techniques<sup>88-90</sup> could be utilized to further improve spectral artifact compensation in these multi-material situations. Ultimately, the choice of beam hardening correction technique is highly application dependent. Nonetheless, our proposed EBHC-GI method could readily be implemented as one step in the x-ray grating interferometry image processing pipeline.

Limitations of EBHC-GI include the empirical approach to generating the dark-field template image. Assigning known homogenous regions in our test objects to have a

normalized visibility signal equivalent to air was necessary as it was unclear as to what would make an ideal dark-field calibration object. This is coupled with the fact that the choice of an ideal dark-field test object would likely be specific to material, energy and other systemic factors<sup>42</sup>. Additionally, EBHC-GI is a first order correction and thus some rings remained due to detector gain inconsistencies or higher order beam hardening effects. Removing these residual artifacts would be best handled with iterative methods<sup>84</sup> adapted to account for spatially varying grating effects or additional image filtering<sup>91</sup>. Additionally for the dark-field contrast, improved artifact reduction may be possible by first separating the influences of other contrasts<sup>81</sup>. Another approach would be to add a second modulating term to include both dark-field and attenuation contributions. However, this comes at the cost of increasing the number of images required to determine the correction coefficients.

Finally, the push to enable human imaging with grating interferometry<sup>34,92,93</sup> requires higher x-ray energies (e.g., high tube potential settings) and larger fields-of-view which places even higher demands on grating design and fabrication. When imaging at these higher energies partial transmission becomes unavoidable<sup>74</sup>, and can even be desirable when phase and dark-field image quality is to be balanced with attenuation image quality<sup>23,74,94</sup>. Our results demonstrate that image quality can be preserved for all three contrast mechanisms using a polychromatic x-ray source. This eases the requirements for grating design and fabrication and may facilitate multi-contrast x-ray studies in humans.

## **4.5 Conclusions**

In this investigation we introduced an empirical correction for beam hardening in grating interferometry, EBHC-GI, that is an extension of a two-variable polynomial correction for anti-scatter grids that we adapted to the unique contrast mechanisms and system properties of a grating interferometer. These adaptations included applying the polynomial correction to each contrast mechanism separately and determining an optimal spatial modulating term for the dark-field contrast. In attenuation and phase contrast images, this term was the reference projection data for each respective contrast mechanism. However, due to cross-contamination of attenuation and phase contrast information into the dark-field channel, the optimal dark-field modulating term was determined for our system to be the attenuation

reference projection data. Quantitative assessment of our method showed a reduction in beam hardening artifacts due to both the sample and the gratings in both water and silicon test objects, representing imaging of low- and higher-Z materials, respectively. This empirical method can be used, without the need of detailed system or sample knowledge, to correct for beam hardening effects in the sample and in the gratings. Once determined, the coefficients can be used on all subsequent scans of like materials performed with similar acquisition settings.

## **4.6 Accomplishments**

The work described in this specific aim has produced one peer-reviewed journal article:

**Nelson BJ**, Leng S, Shanblatt ER, McCollough CH, Koenig T. Empirical beam hardening and ring artifact correction for x-ray grating interferometry (EBHC-GI). *Medical Physics*. 2021;48(3):1327-1340. doi:<https://doi.org/10.1002/mp.14672>

# CHAPTER 5

---

## Dark-Field Enhanced Attenuation Imaging

### 5.1 Introduction

Dark-field contrast was originally introduced as being caused by small-angle x-ray scattering (SAXS)<sup>18</sup>, which is an energy dependent property related to a material's composition and structure size<sup>53</sup>. Talbot-Lau grating interferometry enables x-ray phase and dark-field measurements with standard x-ray sources and detectors, greatly expanding their potential applications and use. However, experiments have shown that dark-field measured on these systems also derives from intra-pixel phase gradients and thus are a function of the system's spatial resolution relative to the material structure size<sup>42</sup> (**Section 2.6**). This presents opportunities to gain signal from unresolved structural changes, otherwise lost by partial volume averaging. It also poses challenges for the quantitative use of dark-field, as the dark-field signal also depends on any process altering the spatial resolution of the system including detector pixel size, focal spot size, and magnification<sup>42</sup>. In x-ray attenuation CT imaging, insufficient spatial resolution is responsible for partial volume averaging where the attenuation information from tissues of differing attenuation properties that are contained within one voxel are averaged together. In lung imaging, this results in blurred boundaries between tissues and air and is responsible for the wide range of lung CT numbers in the parenchyma. These blurring effects can be detrimental in attenuation CT of the lungs by obscuring characteristic disease patterns like honeycombing required to diagnose idiopathic pulmonary fibrosis (IPF) and underestimating quantitative assessments of fibrosis extent<sup>21,22,65</sup>.

The purpose of this work is to introduce and validate a means of combining dark-field's intra-pixel phase gradient sensitivity with the simultaneously acquired phase and attenuation signals to partially restore spatial resolution and improve contrast while maintaining the quantitative value and interpretability of the attenuation and phase information. Furthermore, incorporating dark-field information introduces opportunities

for enhanced contrast between materials with similar attenuation but distinct structural properties. These techniques are hereafter referred to as dark-field enhanced attenuation (DFEA) and dark-field enhanced phase (DFEP). This chapter is organized into three main sections, with results reported immediately after the methods in each section. First, the claim that DFEA and DFEP improve spatial resolution is investigated experimentally with edge spread function measurements on a solid-water phantom with accompanying modulation transfer function (MTF) calculations to assess contrast retention at different spatial frequencies. Next, the claim that DFEA and DFEP maintain quantitative attenuation and phase values in solid tissues while enhancing contrast with unresolved structures is supporting with region-of-interest (ROI) measurements of contrast, noise, and contrast-to-noise ratios (CNR). Finally, the qualitative impact of these benefits is demonstrated in the context of lung imaging by applying DFEA to an *ex vivo* fixed lung sample.

## 5.2 Dark-Field Enhanced Attenuation and Phase: General Approach

X-ray attenuation has long provided reliable measurements of lung structure due to the natural high contrast between the x-ray attenuation of air and tissue. Partial volume effects, however, result in blurring that reduces the sensitivity of attenuation radiography and CT to detect small (<5mm) pulmonary nodules<sup>95</sup> and quantify fibrosis extent<sup>22</sup>. Edge enhancement techniques have been used to mitigate these spatial resolution limitations in x-ray attenuation imaging to better resolve small focal lung pathology<sup>96</sup>. A widely used edge-enhancing post-processing technique is unsharp masking<sup>97</sup> where the measured attenuation signal  $A$  is copied and blurred yielding  $A'$ . Taking the difference between original measurement and the blurred copy reveals edges lost from the blurring which are scaled by an enhancement factor  $\alpha$ , typically between  $[0, 1]$  and added back to the original image

$$A_{\text{unsharp}} = A + \alpha(A - A'). \quad (5.1)$$

While unsharp masking has been used successfully to visually enhance edges, it is not quantitative as the true edge information is lost and can only be estimated by taking the difference from further blurring.

X-ray dark-field  $D$  provides access to phase gradient signal lost to blurring processes and thus could be used in place of  $(A - A')$  in **Eq. 5.1** to restore edge information in phase contrast images  $\Phi$ , in a process hereafter referred to as dark-field enhanced phase (DFEP):

$$DFEP = \Phi - \alpha D. \quad (5.2)$$

In practice grating interferometers directly measure *differential phase*  $\frac{\partial\Phi}{\partial x}$  and not phase  $\Phi$ , which complicates the direct application of **Eq. 5.2**. Differential phase can be integrated in the phase step direction  $x$  to recover  $\Phi$ . However, noise from detectors, photon statistics, and phase step vibrations are also integrated into the phase signal yielding low-frequency noise effects<sup>72</sup>. Iterative methods have been introduced to better recover this phase information, yet it remains a non-trivial task<sup>78,98</sup>. Furthermore, phase is a circular measurement bound by  $(-\pi, \pi)$  and thus phase wrapping becomes an issue when the projected differential phase shift exceeds the bounds. To reduce phase wrapping, water-like soft tissue samples are often immersed in a water bath for x-ray phase contrast measurements to avoid large phase gradients with the air background<sup>99</sup>. While mild phase wrap can be recovered with phase unwrapping algorithms<sup>100,101</sup>, the many air-tissue interfaces of the lungs yield large phase gradients and substantial phase wrap that are challenging to recover.

These complications of using phase for lung imaging combined with the established use of attenuation contrast motivates the use of dark-field information to restore blurred edge information in attenuation images via dark-field enhanced attenuation (DFEA)

$$DFEA = A - \alpha D. \quad (5.3)$$

Given that attenuation  $A$  and phase  $\Phi$  are strongly correlated at diagnostic x-ray energies (40-120 keV),<sup>68</sup> the phase edge information contained in dark-field also correlates with the blurred attenuation edges. This supports the use of dark-field to recover edges in both attenuation and phase for appropriate values of  $\alpha$ . Given the large difference in signal magnitude between attenuation and phase in soft tissues (**Table 2.1**),  $\alpha$  must be scaled down to reflect these differences in signal magnitude. An estimate of  $\alpha$  can be found as the

ratio of the mean attenuation and phase signals from a homogenous region covering the primary material of interest, e.g., water.

### **5.3 Influence on Spatial Resolution**

To evaluate DFEA and DFEP's ability to restore spatial resolution, a QRM micro-CT bar pattern phantom was imaged with the grating interferometer described in **Chapter 3**.

#### **5.3.1 Methods**

All phase step projections were acquired at 55 kVp, 40 mA, and in 6 steps covering one period of  $G_2$  at 1.5 seconds per step. Attenuation, differential phase, and dark-field projections were then retrieved from phase step data using the Fourier method<sup>18</sup>. In our experimental setup, mean reference visibility was measured to be  $V_{1,r} = 16.4\%$ . 721 projections were acquired in equiangular intervals covering 360 degrees and reconstructed into  $512 \times 512$  matrix images of  $60 \mu\text{m}$  isotropic voxels using the FDK algorithm<sup>76</sup> with a Ram-Lak filter for attenuation and dark-field images and a Hilbert filter to integrate phase in the reconstruction process<sup>56</sup>.

From these images, an edge spread function was measured by averaging 20 adjacent slices in a cylindrical "solid water" module of a QRM micro-CT phantom<sup>87</sup>. The module was carefully aligned such that the central axis of the cylinder aligned with the CT rotational axis. A radially averaged line profile was then measured from the center of the circular axial cross-section. Prior edge spread function (ESF) profiles between attenuation and DFEA as well as phase and DFEP were compared against the ground truth edge response determined from the known geometry of the phantom. Spatial resolution was assessed in terms of qualitative difference from the true edge response as well as differences in MTF curves calculated from the edge responses. MTF was calculated by first interpolating each ESF, taking the finite difference derivative to estimate the line spread function, taking the Fourier transform via FFT and normalizing with respect to the zero frequency MTF(0), described by Richard et al 2012<sup>102</sup>.

#### **5.3.2 Results**

Edge restoration by subtracting the scaled dark-field image was qualitatively assessed by viewing images of the attenuation, phase, and dark-field enhanced images in **Figure 5.1**. In calculating DFEP, dark-field was directly subtracted from phase ( $\alpha = 1$ , **Eq. 5.2**). In calculating DFEA,  $\alpha$  from **Eq. 5.3** was determined empirically as the ratio of mean attenuation to mean phase values measured in the solid water phantom. It was found to be  $\alpha = 0.025$  in this current study. Radially averaged edge spread functions derived from these solid-water phantom images show that both DFEP and DFEA better estimate the underlying edge distribution when compared against the simulated truth value as indicated by arrows identifying the restored edge features (**Figure 5.2**).

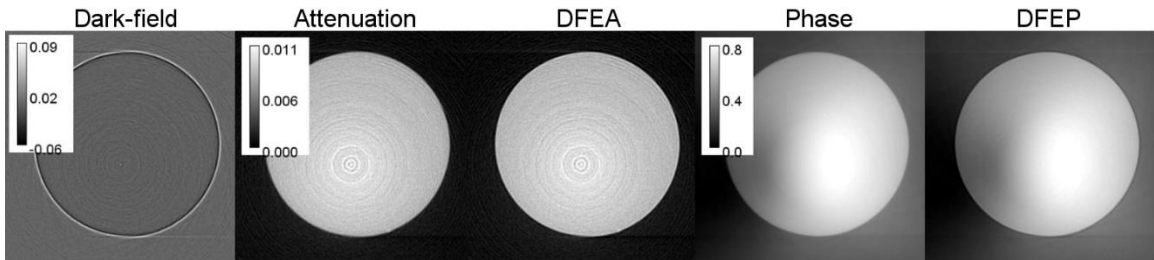


**Figure 5.1** Synergistic use of dark-field with attenuation and phase contrast images of a cylindrical solid water phantom. From left to right, dark-field, phase, dark-field enhanced phase (DFEP), attenuation, dark-field enhanced attenuation (DFEA).

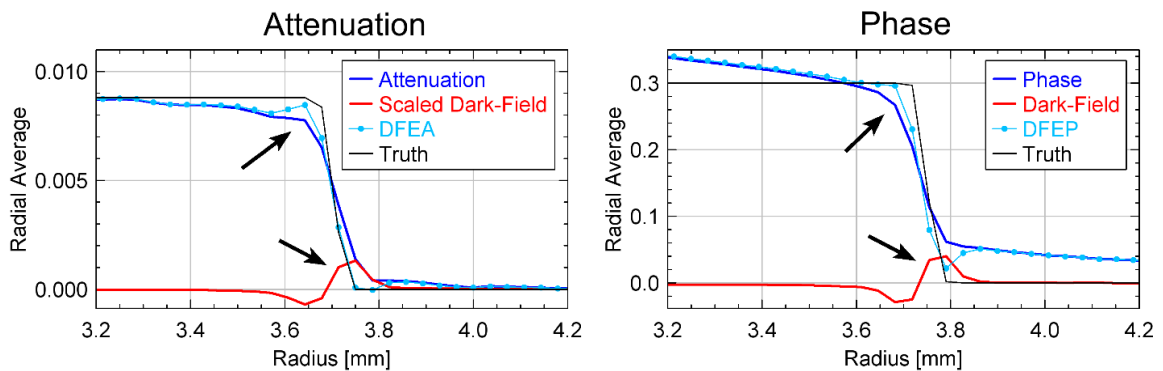


**Figure 5.2** Dark-field recovers high spatial frequencies. **Left:** radially averaged edge spread function profiles from attenuation images of the water cylinder. **Right:** profiles from the phase images of the water cylinder. Arrows indicate restoration of edge relative to the true profile.

These findings are further supported by MTF measurements which quantify the preservation of contrast as a function of spatial frequency, reported as line pairs per mm (lp/mm). The MTF response for an ideal edge is a constant value of 1 at all spatial

frequencies. The MTF responses of both DFEA and DFEP are greater than the respective attenuation and phase MTFs at all measured spatial frequencies better approximating the ideal response (**Figure 5.3**). Notably the greatest improvement in MTF is around 5 lp/mm for both DFEA and DFEP which is approximately half of the maximum sampling rate. By quantifying spatial resolution at different spatial frequencies as nearness to the ideal edge MTF response, these results support the claim of improved spatial resolution of DFEA and DFEP over attenuation and phase for all measured spatial frequencies.

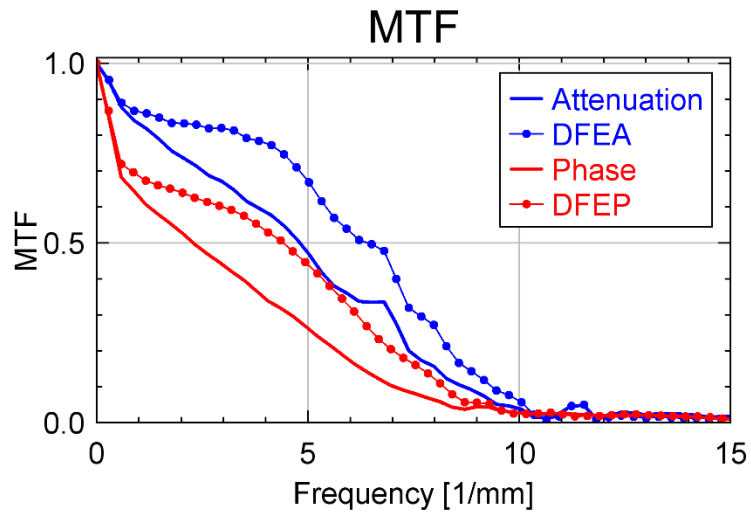


**Figure 5.3** Modulation transfer function comparisons between attenuation, phase, and dark-field enhanced phase and attenuation profiles.

While subtracting dark-field can effectively restore edges in both phase and attenuation images, it cannot address the low frequency noise prevalent in the phase images (**Figure 5.1**), which remains a challenge in the quantitative use of phase contrast imaging. For this reason, the remainder of this chapter focuses on the use of dark-field to enhance image quality of attenuation images, which are regularly used in lung imaging due to their advantageous natural contrast between air and tissue and interpretability as local lung density.

**Figures 5.1-5.3** demonstrate the restoration of spatial resolution via DFEP and DFEA by directly subtracting dark-field from phase ( $\alpha = 1$ ) and scaling dark-field based on empirical attenuation and phase measurements before subtracting it from attenuation ( $\alpha = 0.025$ ). **Figure 5.4** plots MTF curves for larger values of  $\alpha$  which represent further edge-

enhancement, i.e., MTF values exceeding 1 at some spatial frequencies. Bar plots are shown at right of the MTF curves showing spatial frequencies at which 50%, 30%, and 10% contrast are maintained across the different image series. The overall higher MTF curves of DFEA for different values of  $\alpha$  means that more contrast is maintained at higher spatial frequencies. In particular, the spatial frequency at which 50% contrast is preserved is nearly doubled for DFEA with  $\alpha > 0.5$  compared to the attenuation image. The relative improvement is lessened at 30% and 10% contrast preservation as the primary spatial resolution enhancement is around half the maximum sampling rate at 5 lp/mm.

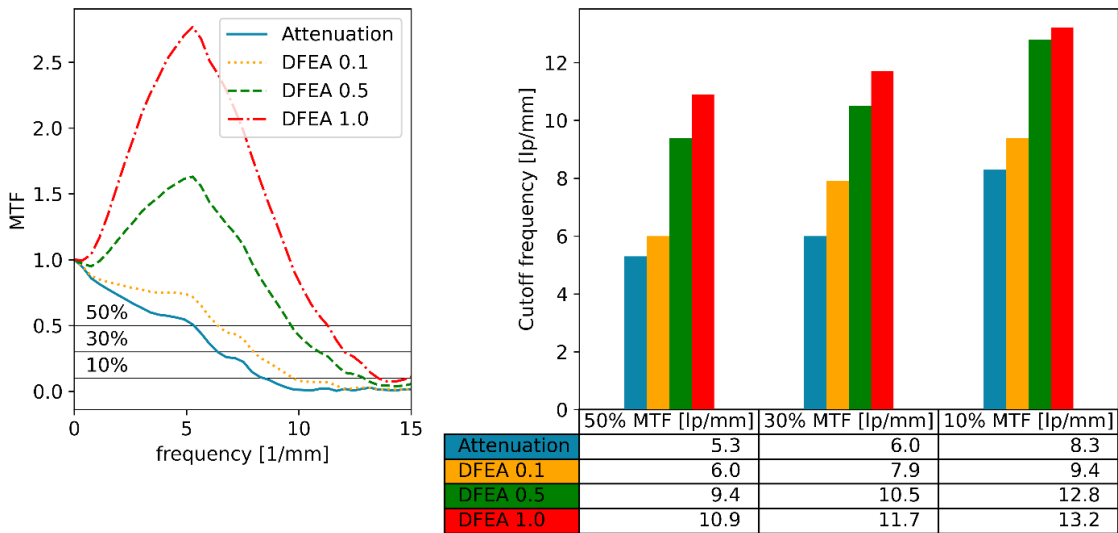


**Figure 5.4** Using enhancement factor  $\alpha$  for variable edge enhancement. **Left:** Measured MTF curves from attenuation ( $\alpha = 0$ ), and DFEA with increasing enhancement factor  $\alpha$ . **Right:** Bar chart plotting spatial frequencies, reported as line pairs per mm (lp/mm) at which different contrast levels are maintained, corresponding to 50%, 30%, and 10% MTF for attenuation and DFEA  $\alpha$  for different values of  $\alpha$ .

## 5.4 Influence on Contrast with Unresolved Structures

The lung parenchyma is the functional volume of the lung where gas exchange occurs and is comprised of an interconnected web of small airways and blood vessels terminating at the alveolar sacs. The structures of the parenchyma are some of the thinnest in the body to minimize diffusion distance between the atmosphere and blood, with respiratory airways and alveoli walls being only a single cell in thickness at around 2  $\mu\text{m}$  thick. From the

perspective of clinical lung imaging, these functional structures where pathology begins are two orders of magnitude smaller than clinical CT imaging systems' resolvable spatial resolution. Thus, a single CT voxel of  $(0.5 \text{ mm})^3$  can contain tens of alveoli, which can be approximated as packed hollow spheres with  $\geq 2 \text{ }\mu\text{m}$  thick membranes  $100 - 200 \text{ }\mu\text{m}$  in diameter<sup>103</sup>. These structures are averaged out in large attenuation CT voxels yielding local measures of mean lung density. Changes in lung health can impact lung density. Substantial changes in CT number away from normative values for a given point in the respiratory cycle can be indicative of pathology such as air trapping or fibrosis. However, given the large difference between clinical CT spatial resolution and the fundamental structures of lung, the large degree of partial volume averaging lessens sensitivity to early structural changes that do not strongly affect the mean lung density. The top row of **Figure 5.5** provides a contrived example of four regions sampled by a PSF approximately equal to the imaging pixel width. Despite the widely varying structural arrangement of tissue shown in white and air represented by black, all four regions have the same density and thus have a uniform attenuation CT response. X-ray dark-field provides an opportunity to distinguish these structures with uniform attenuation as the number of unresolved gradients varies by region.

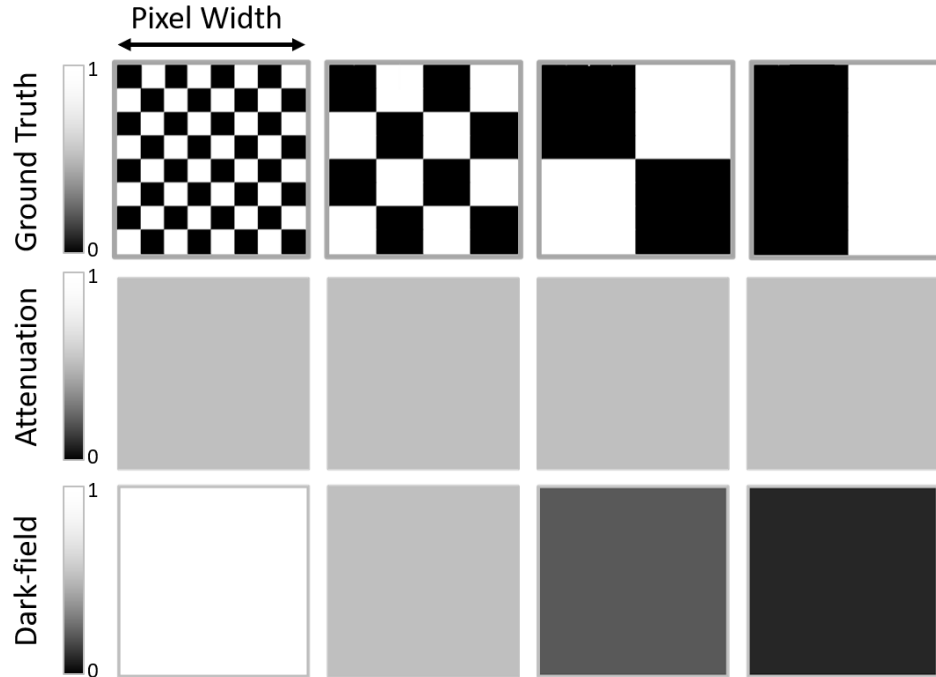


**Figure 5.5** Four distinct regions sampled by a CT system with PSF approximated by its pixel size yield a uniform attenuation measurement but can be distinguished by dark-field due to the difference in number of unresolved gradients. In the ground truth row white represents tissue and blacks represents air space in this contrived model of lung. In the attenuation and dark-field rows greater signal is represented in white and null signal by black according to the color bar at left.

By combining both attenuation and dark-field signals in DFEA, contrast between large homogenous structures (relative to the spatial resolution of the imaging system) and heterogenous structures, such as the parenchyma, can be further enhanced. This proposed benefit of DFEA is first demonstrated in a phantom experiment with a hollow cylindrical phantom with six inserts of varying attenuation coefficients and heterogeneity.

#### 5.4.1 Methods

The phantom has two sections of three materials each. The first is composed of mineral oil, water, and saturated saltwater inserts representing homogenous regions of varying attenuation coefficients. The second section features three low attenuating materials of varying porosity and structural makeup and are known to generate dark-field signal. These include a loosely packed cotton gauze, polyurethane hard foam, and polystyrene soft foam. To assess the ability of DFEA to enhance contrast between these low attenuating materials while not biasing the quantitative value of the large homogenous materials, circular

regions-of-interest (ROIs) were selected covering each insert to measure the mean and standard deviation of the DFEA signal for varying degrees of  $\alpha$ . Changes in mean signal can be used to assess contrast differences between materials and standard deviation in the homogenous regions can be used as a measure of noise.

#### 5.4.2 Results

**Figure 5.6** demonstrates the role of incorporating dark-field information to enhance contrast with unresolved structures without biasing the attenuation values in large, resolved materials. The left most column of **Figure 5.6a** shows the attenuation image of both sections of the phantom where the upper inserts of salt water, water, and mineral oil represent large regions of varying attenuation properties. Meanwhile, the bottom inserts are low attenuating and indistinguishable from each other and the air background. The rightmost column shows the dark-field image which is not able to distinguish the various attenuating upper inserts, but can distinguish the lower inserts, particularly the cotton gauze due to its fine fibers. The middle columns of **Figure 5.6a** show DFEA for different values of  $\alpha$  representing increasing contribution of dark-field information. Given that the homogenous attenuating inserts (mineral oil, water, salt water) do not generate dark-field, their signal is not visually altered except for an increase in noise at larger  $\alpha$ . However when more dark-field information is incorporated with  $\alpha = 0.9$ , contrast differences are present between both the large attenuating materials and unresolved low attenuating materials simultaneously. These findings are supported quantitatively by plotting ROI measurements of signal (mean ROI value) and noise (ROI standard deviation) as a function of  $\alpha$  in **Figure 5.6b**. This shows that incorporating more dark-field information by increasing  $\alpha$  maintains contrast between large attenuating inserts (salt water, water, and mineral oil) by not impacting their mean signal level. Increasing  $\alpha$  increases contrast between air and the different non-attenuating materials, most notably the cotton gauze. In terms of noise, a tradeoff was observed to exist that by increasing  $\alpha$  noise, defined as standard deviation in the ROI, increased in the large attenuating material inserts. While this trend was also observed in the non-attenuating materials, not all the increase in standard deviation can be attributed to noise as much of the increase is due to increased contrast with real structures contained within the ROI.

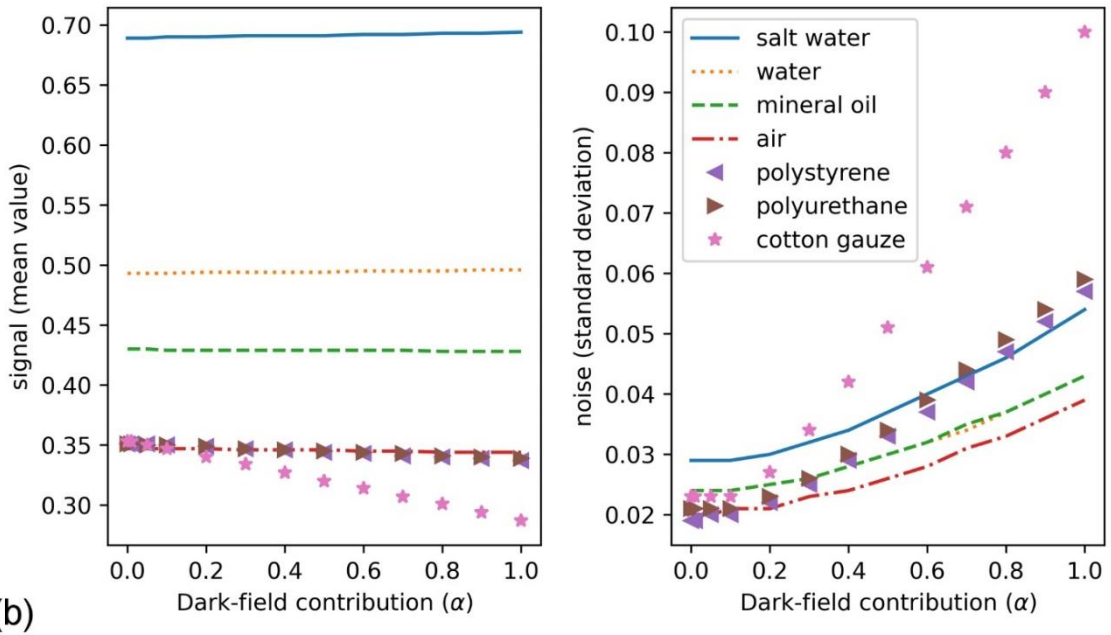
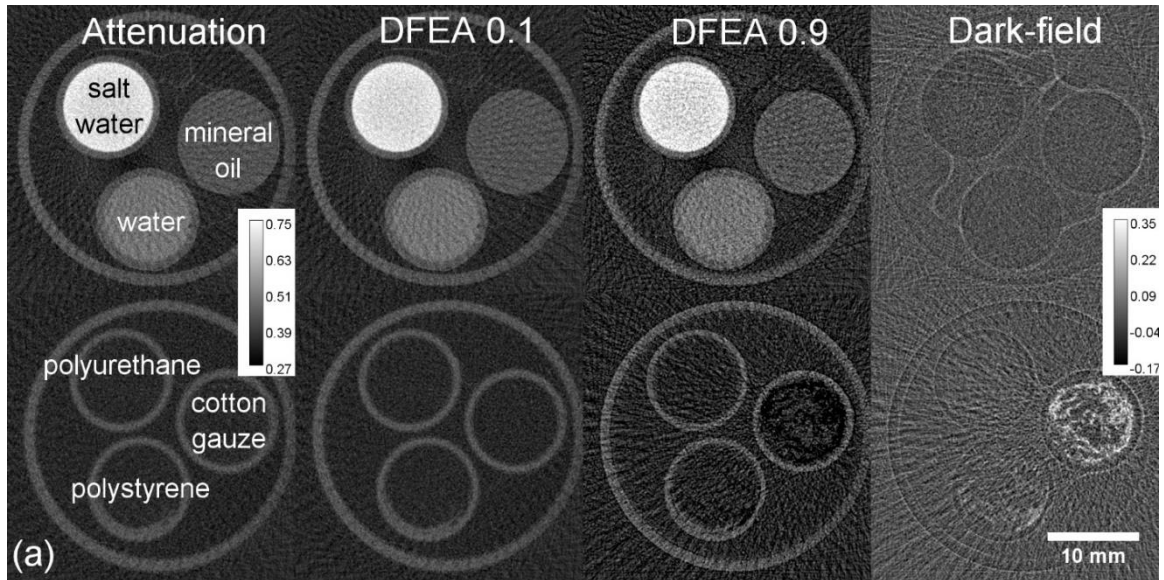


**Figure 5.6** Influence of dark-field contribution ( $\alpha$ ) in materials of different x-ray attenuation and porosity. **(a)** Phantom with six inserts. Top row shows different attenuating materials while the bottom row shows non-attenuating materials with different porosity. At left is the attenuation image with the dark-field image at right. The middle columns show DFEA images for different values of  $\alpha$ . **(b)** Signal and noise measured in circular regions of interest covering each of the inserts for all six materials for increasing values of  $\alpha$  in DFEA.

## 5.5 Qualitative Evaluation of DFEA on Lung Imaging

Micro-CT imaging of bleomycin mouse models is important in studying mechanisms and interventions of idiopathic pulmonary fibrosis<sup>104</sup>. *In vivo* micro-CT is used for longitudinal measurements of lung density, typically with 30  $\mu\text{m}$  isotropic voxels. However, it cannot be used to reproducibly measure alveoli-sized lung structure due to limits in spatial resolution and challenges of respiratory motion blur, even with gating techniques<sup>21</sup>. Like clinical lung CT, these small structures become blurred out by partial volume effects where voxels represent mean lung density in the region. *Ex vivo* lung imaging enables reproducible high-resolution imaging to accurately measure lung structure down to the level of small airways and alveoli<sup>105</sup> to better quantify fibrotic disease than is possible with *in vivo* techniques<sup>22</sup>. X-ray dark-field offers a potential compromise between these two regimes of micro-CT by providing indirect measures of unresolved signal not available in low resolution *in vivo* micro-CT. *In vivo* x-ray dark-field micro-CT systems have been developed and have already shown improved sensitivity at detecting certain lung pathologies<sup>30,106</sup>. Furthermore, DFEA has potential to maintain the quantitative interpretability of attenuation CT values combined with edge restoration and increased contrast with unresolved lung structures with dark-field. The following study provides a qualitative assessment of DFEA applied to lung imaging.

### 5.5.1 Methods

To best demonstrate the effects of DFEA, the mouse lungs used were excised from an *ex vivo* cohort. Mice were imaged *ex vivo* to enable repeatable scanning and to avoid blur associated with respiratory motion. All animal studies were approved by Mayo Clinic's Institutional Animal Care and Use Committee. Fibrotic pathology was induced in the lungs via intratracheal application of bleomycin. Following 21 days of incubation, the lungs were surgically removed and cannulated for fixation (**Figure 5.7a**). Fixation is necessary in *ex vivo* lung imaging to maintain the air-filled structure of the lung. A fixation solution of 50% PEG 400, 25% Ethyl alcohol, 10% formaldehyde and 15% water was instilled via the trachea to a filling pressure of a 20 cm water column. Compared to vascular perfusion of fixative, the tracheal instillation route better preserves airway structures and leaves blood vessels naturally radiopaque, better resembling the *in vivo* appearance (**Figure 5.7b**).

Following administration of fixative via trachea instillation, the lungs were tied off at the trachea and immersed in the same fixative solution for seven days before being air-inflated at 25 mmHg and dried for 72 hours to hold their air-inflated state<sup>107</sup>. The final fixed lung is shown in **Figure 5.7c**. This fixation method preserves native air-tissue contrast as well as the inflated structure of the lung, and is a standard method for *ex vivo* structural imaging as determined by the American Thoracic Society guide on structural lung imaging<sup>108</sup>. In total 7 lung samples were successfully fixed and used for imaging in this study.

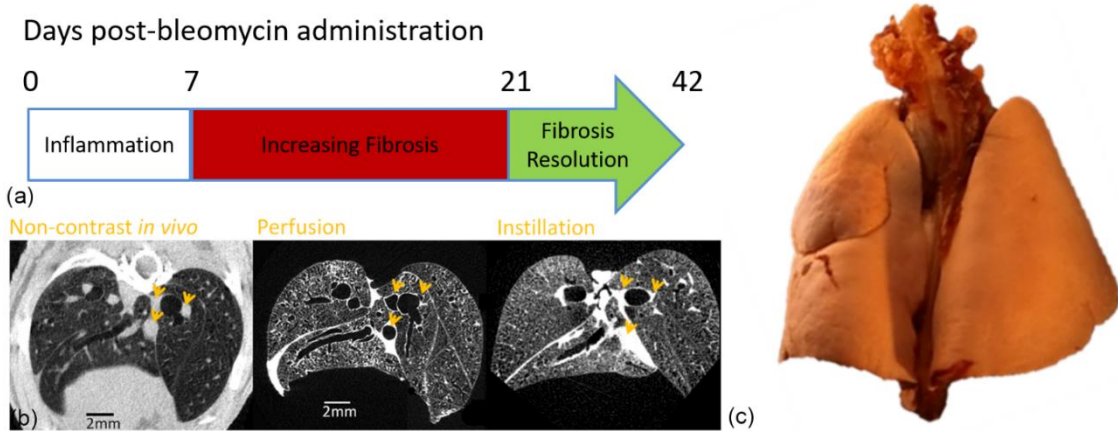


**Figure 5.7** Bleomycin mouse model of idiopathic pulmonary fibrosis. (a) Summary of the bleomycin mouse model of pulmonary fibrosis where bleomycin is administered via the trachea and incubated for 21 days before lung extraction and fixation. (b) Comparison of different routes of fixative administration lung structures shown in ex-vivo micro-CT compared to in-vivo micro-CT. (c) External view of fixed inflated lungs using the instillation method.

The fixated *ex vivo* lungs were then imaged with the previously described grating interferometer. Projections were acquired at 55 kVp, 40 mA, and 1.5 seconds per phase step for 5 steps covering one period of  $G_2$ . CT images were reconstructed from 721 equiangular projections covering 360 degrees. DFEA projections and CT images were generated using the retrieved attenuation and dark-field projections and CTs respectively using **Eq. 5.3**. The enhancement factor  $\alpha$  was determined empirically as the ratio of mean attenuation and phase signal from a solid tissue ROI. Projections and CT images were used for qualitative comparisons of lung structure.

## 5.5.2 Results

The qualitative impact of edge restoration and enhanced contrast with unresolved structures is evaluated on lung imaging using DFEA projections is first shown in **Figure 5.8** alongside the simultaneously acquired attenuation and dark-field images. In the attenuation projection signal is brightest just posterior to the heart where the lungs are thickest. The heart, esophagus, and large blood vessels are most visible as hyperattenuating structures with the bilateral major bronchi visible as hypoattenuating structures. In the dark-field projection (**Figure 5.8** center), the signal is also brightest where the lungs are thickest reflecting the increased penetration depth through unresolved edges. The large heart shadow at the lung apex and dark esophagus down the midline are the most visible structures in the dark-field image as null signal. However, when used alone, the bright dark-field signal combined with its high frequency edge enhancement obscures blood vessels and airways visible in the attenuation projection. When information from these two projection series is combined via DFEA, the structures from the attenuation projection are preserved but with increased contrast between the blood vessels, heart, and the lung parenchyma background composed of unresolvable structures.

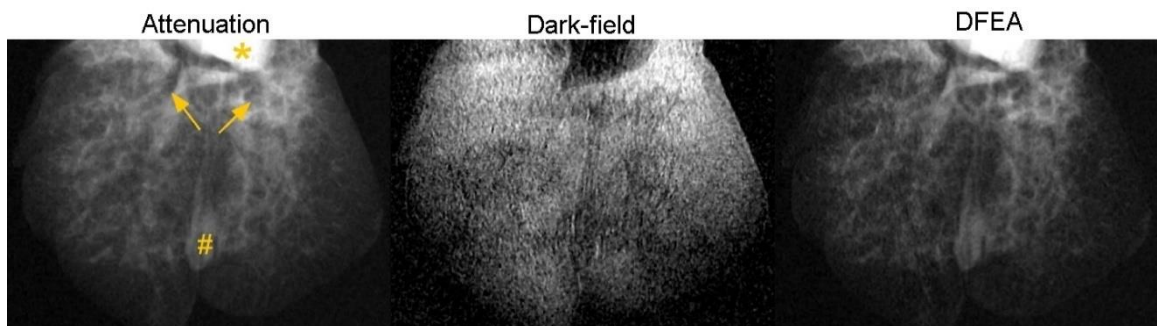


**Figure 5.8** Comparison of attenuation, dark-field, and dark-field enhanced attenuation (DFEA) projections. Large attenuating structures like the heart (\*), esophagus (#), large blood vessels, and fibrosis accumulations around the radiolucent bronchi (arrows) appear bright in the attenuation image and null in the dark-field image.

These effects are more pronounced in axial CT images shown in **Figure 5.9**. Consistent with the projections, large attenuating structures such as blood vessels, the esophagus, and fibrotic loci appear bright in the attenuation image and dark in the dark-field image. In the dark-field image the edges of large structures and the parenchyma background composed of many unresolved structures are brightest. Incorporating this dark-field information with the attenuation image in DFEA restores many blurred out features resulting in sharper

edges and improved resolution of small structures such as the micro-honeycombing indicated by the red arrow in the DFEA image (**Figure 5.9** center). In addition to improved resolution of small structures and enhanced parenchyma contrast, select artifacts in phase stepping projections are present in both the attenuation and dark-field images and as a result are removed in DFEA. An exemplary streak artifact is present in the attenuation and dark-field images (**Figure 5.9** left and center) but is absent in the DFEA image (**Figure 5.9** right).

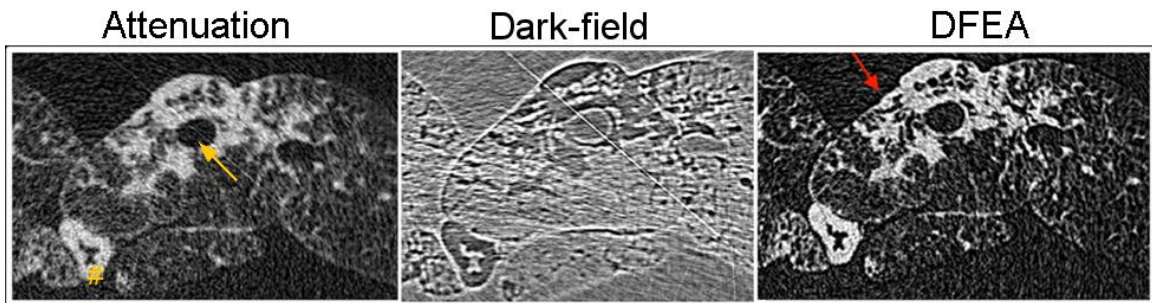


**Figure 5.9** Comparison of lung CT cross-sections with DFEA. **Left:** Attenuation axial CT image cropped around a peribronchial fibrotic lesion. Other relevant anatomy present are the esophagus (#) and major bronchi (orange arrow). **Center:** Dark-field axial image of the same region. **Right:** dark-field enhanced attenuation (DFEA) image shown at the same display settings as the original attenuation image at left. Note the absence of streak artifact in the DFEA image, which is present in both the attenuation and dark-field image because it was present in the raw phase step data.

A final comparison was performed to assess the potential impact of the interferometer gratings on the resulting image quality of the lung images. Without moving the lung sample, a second repeat CT acquisition was performed after removing all gratings from the beam line. CT acquisition settings were adjusted to match noise levels with the resulting image series (“Attenuation no gratings” shown side by side with the attenuation (“Attenuation with gratings”), dark-field, and DFEA image series from the original interferometer acquisition (**Figure 5.10**). As the primary consequence of the gratings is absorption of x-rays (primarily from absorption gratings  $G_0$  and  $G_2$ ) and thus an increase in scan time there is no visual change in spatial resolution between the attenuation images with and without the gratings. Secondary effects include beam hardening which reduces the signal brightness most noticeable in the heart (shown at the same display settings). The ring artifacts also induced by the gratings are addressed via algorithmic correction in

**Chapter 4.** However, by incorporating the gratings and performing an interferometer acquisition the additional dark-field data provides additional signal to unresolved edges making many small structures more visible in the DFEA image all with the same x-ray detector and source configuration.

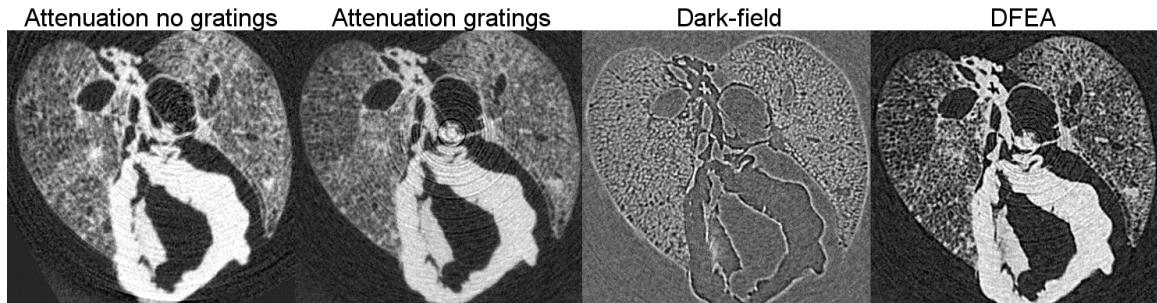


**Figure 5.10** Impact of interferometer gratings in lung imaging.

## 5.6 Discussion

Spatial resolution in x-ray attenuation imaging is influenced by many factors, including detector pixel size, scintillator screen thickness, focal spot size, and magnification, which in practice are optimized to balance spatial resolution with x-ray dose and scan time. These factors all contribute to the point spread function (PSF) of the imaging system that blur the edges around the sampled object. In x-ray grating interferometers with PSFs larger than several periods of the analyzer grating, these same blurring effects can produce dark-field contrast. This chapter has introduced a means of using dark-field to partially recover phase contrast edges lost due to blurring, a process introduced as dark-field enhanced phase (DFEP) imaging. Due to the correlation of x-ray phase and attenuation in biological tissues in medical x-ray energies, dark-field images can also be used to reclaim edges in attenuation images as well via dark-field enhanced attenuation (DFEA) imaging. Given that low frequency noise and phase wrap challenge the use of x-ray phase for lung imaging, DFEA represents a promising use of phase-gradient information to reclaim edges and enhance contrast with unresolved structures in lung imaging.

Experimental results in this chapter demonstrated the use of DFEA to restore edge sharpness in an edge spread function measured from a cylindrical water phantom of known

geometry. An improvement in spatial resolution at all measured spatial frequencies was demonstrated as an increase in the modulation transfer function (MTF) better approximating the ideal edge response in both DFEA and DFEP (**Figure 5.3**). Further enhancements to spatial resolution were then shown by further increasing the enhancement factor  $\alpha$  (**Eq. 6.3**) as measured by higher modulation transfer function (MTF) curves (**Figure 5.4**). A phantom with different inserts was then used to demonstrate that DFEA can increase contrast between unresolvable structures without biasing attenuation measurements in larger structures. Noise ROI measurements performed on these scans revealed that increasing the influence of dark-field information with  $\alpha$  can also increase noise. Future work remains to mitigate this noise amplification by applying a minimum threshold to the dark-field image before subtracting it from the attenuation image, a practice similar to that incorporated in unsharp mask edge enhancement<sup>109</sup>. Together, these image quality enhancements were shown to improve resolution of small structures in a fixed *ex vivo* mouse model of pulmonary fibrosis. A comparison of lung images acquired with the same system but without interferometer gratings confirmed that the gratings do not negatively impact the perceptible spatial resolution. Rather, by having access to the dark-field image data smaller lung structures can be more effectively visualized using DFEA on the same system.

## **5.7 Conclusions**

Intra-pixel phase gradients are the predominant source of dark-field signal in laboratory-based x-ray grating interferometers. Here, it has been shown how this gradient information in dark-field images can be used to restore spatial resolution and enhance contrast with unresolved structures by subtracting dark-field image data from the phase and attenuation images. An *ex vivo* mouse lung model of pulmonary fibrosis was used to demonstrate the ability of this new technique, dark-field enhanced attenuation (DFEA), at improving resolution of small structures.

## **5.8 Accomplishments**

### **5.8.1 Conference Presentations**

The work presented in this chapter resulted in an oral presentation presented at SPIE Medical Imaging 2022.

### **5.8.2 Conference Proceedings**

The work presented in this chapter resulted in a conference proceeding that has been submitted to SPIE Medical Imaging 2022.

1. Complementary Use of X-Ray Dark-Field and Attenuation Computed Tomography in Quantifying Pulmonary Fibrosis in a Mouse Model.; 2022.  
doi:10.1117/12.2612877

# CHAPTER 6

---

## Complementary Use of X-Ray Dark-Field and Attenuation Computed Tomography in Quantifying Pulmonary Fibrosis in a Mouse Model

### 6.1 Introduction

In clinical CT measuring fibrosis extent is a key quantitative imaging feature used both in diagnosing interstitial lung diseases (ILDs) as well as in prognosticating patient outcomes<sup>110</sup>. In micro-CT characterization of ILD models, fibrosis extent, often measured as segmented fibrosis volume, is the primary measurement used to evaluate pulmonary fibrosis severity. Moreover, the sensitivity to subtle changes in fibrosis volume, especially in early stages of fibrosis is limited by spatial resolution. X-ray dark-field is more sensitive in detecting structural changes otherwise too small to be resolved on the same detector via traditional absorption radiography and has been shown to be more sensitive at detecting various lung pathologies in both small and large animal pilot studies including emphysema<sup>23–25</sup>, inflammation<sup>26,111</sup>, lung cancer<sup>28</sup>, and fibrosis<sup>29</sup>. However, x-ray dark-field from laboratory-based systems with large focal spots and detector pixels derives from intra-pixel phase gradients and is of limited quantitative value when used alone<sup>42</sup>.

**Chapter 5** introduced and validated dark-field enhanced attenuation (DFEA) imaging to leverage dark-field's sensitivity to unresolved structures to restore blurred edges to the simultaneously acquired attenuation image. Phantom experiments demonstrated that DFEA improves spatial resolution by recovering this blurred edge information while also improving contrast with unresolved structures. The chapter concluded with a qualitative characterization of the impact these image quality enhancements of DFEA have on visualizing lung structure and pathology. The results of this study showed that DFEA improves the resolution of fine structures in the lungs including airway walls in the lung parenchyma and improves definition of micro-honeycombing structures in fibrotic loci.

The work presented in this chapter expands upon these investigations of DFEA applied to lung imaging by assessing its impact on characterizing fibrosis extent. To this end, a cohort of 7 *ex vivo* lungs were fixed and imaged both with grating interferometer micro-CT to generate DFEA images as well as with a dedicated high-resolution micro-CT to get a ground truth estimate of lung structure and fibrosis extent quantified via automatic histogram segmentation.

## 6.2 Methods and Materials

### 6.2.1 Dark-Field Enhanced Attenuation

Spatial resolution limitations of x-ray attenuation imaging systems result in blurring of fine pulmonary anatomy, reducing the sensitivity of attenuation radiography and CT to small scale changes. These same blurring effects are responsible for intra-pixel phase gradients generating dark-field signal (Section 2.6) and can be used to recover phase edge information (Section 5.2). Given that attenuation and phase coefficients are correlated at diagnostic medical energies (40 – 140 keV)<sup>68</sup>, dark-field can also be used to estimate edges lost from partial volume averaging in measured attenuation images  $A$  via dark-field enhanced attenuation (DFEA)

$$DFEA = A - \alpha D \quad (6.1)$$

where scalar  $\alpha$  can be empirically estimated as the ratio of attenuation to phase signal measured in a solid tissue or water region of interest.

### 6.2.2 Sample Preparation

To assess the impact of dark-field enhanced attenuation on quantifying pulmonary fibrosis extent, a bleomycin mouse model of pulmonary fibrosis was used. All animal studies were approved by Mayo Clinic’s Institutional Animal Care and Use Committee. Bleomycin was used to induce disease and the lungs were extracted and fixed *ex vivo* using the methods described in Section 5.5.1.

### 6.2.3 Image Acquisition

Experimental attenuation and dark-field images used in this study were generated with a Talbot-Lau grating interferometer system introduced in **Chapter 3**. The interferometer was operated at a design energy of 40 keV using a first Talbot order geometry (**Eq. 2.7**). The three grating optics were positioned with a  $G_0$ - $G_1$  distance of  $d_{01}=522$  mm and  $G_1$ - $G_2$  distance of  $d_{12}=251$  mm. Phase step curves were acquired by mechanically translating  $G_2$  six equidistant steps covering one Talbot carpet period with an exposure time of 1.5 seconds per step and mean reference visibility of  $V_r=14.7\%$ . Dark field and attenuation contrast projections were acquired over 360 degrees at 0.25 degree increment, retrieved using the Fourier method<sup>56</sup> and reconstructed into volumes of 60  $\mu\text{m}$  cubic voxels following Ram-Lak filtering using the FDK method implemented in the TIGRE reconstruction suite<sup>77</sup>.

#### **6.2.4 Fibrosis Quantification and Performance Evaluation**

In this study the extent of pulmonary fibrosis was quantified in terms of tissue area fraction measured in local regions of axial image slices. Tissue area fraction is defined as the fraction of pixels in a local patch containing tissue over the total patch area after excluding major anatomic structures of the lung such as major bronchi, large blood vessels, the heart, and esophagus<sup>112</sup>. This quantity includes small airway walls, small blood vessels, and fibrotic loci. It has a value of 5-10% in healthy parenchyma and increases progressively with fibrosis severity<sup>22,112</sup>.

To account for the limited number of lung samples available and the heterogenous distribution of fibrosis in each lung, a local patch-based approach was used. In the bleomycin mouse model, fibrosis develops in focal regions, called loci, primarily in the regions near the bleomycin administration site including the major bronchi<sup>113</sup>. Thus, with the limited cohort size, by systematically sampling image patches, a wider range of fibrosis severities can be evaluated. This range includes patches free of pathology with low tissue area fraction to those centered around loci with high tissue area fraction representing locally severe fibrosis.

The systematic sampling of patches was performed as follows: 2 mm square nonoverlapping patches were selected in a process of uniform random sampling<sup>112</sup> where

10 slices were randomly selected from the CT volume with eight patches randomly selected per slice. Slices overlapping the heart, esophagus, major bronchi, and major blood vessels were excluded and did not contribute to the patch count. Tissue fraction in each patch was measured with ImageJ<sup>114</sup> using a global intensity threshold, selected automatically using minimum error thresholding<sup>115</sup> applied to the whole volume intensity histogram for each image series.

The minimum error threshold segmentation technique used to measure tissue area fraction is based upon the pixel intensity distribution in the image patches. As measured by x-rays, the lungs are approximately composed of two constituent materials, tissue with attenuation properties like water, and the air trapped inside. Thus, intensity distributions of lung images are ideally bimodally distributed, with one low attenuation population of pixels representing air pixels and another higher attenuation population representing tissue. Minimum error thresholding assumes that these two populations of air pixels and tissue pixels are normally distributed and finds an intensity threshold that best separates the two populations.

Due to partial volume averaging, voxels containing both materials will measure the average weighted by the relative abundance of each contained within the voxel. This partial volume averaging accounts for the broadened range in attenuation coefficients measured in the lungs and results in underestimations of tissue fraction measurements. As a result, an imaging system with higher resolution is less susceptible to partial volume effects and can better separate tissue spaces from air spaces in the lungs which are composed of many small and high frequency interfaces of air and tissue<sup>22</sup>. For this reason, following CT acquisition on the grating interferometer, the lung specimen was subsequently imaged on a reference Bruker 1276 micro-CT system to acquire a high-resolution volume of the specimen at 5  $\mu\text{m}$  isotropic voxels to get a “ground truth” approximation of the lung structural properties. The reference scan was acquired at 40 kVp, 120  $\mu\text{A}$  with a four frame average of 0.75 s exposure per projection over 360 degrees with a 0.15 degree increment and reconstructed into 5  $\mu\text{m}$  voxels using the provided Bruker NR Recon package.

This reference high-spatial-resolution dataset was registered to the grating interferometer derived attenuation contrast CT volume using the Expert Automated Registration module in 3D Slicer<sup>116</sup>.

With both the grating interferometer micro-CT volumes and reference high-resolution volumes co-registered, 80 random patches were sampled from the same spatial coordinates. The impact of dark-field enhanced attenuation on fibrosis quantification (tissue area fraction) was assessed in terms agreement with the 5  $\mu\text{m}$  reference micro-CT scan. This agreement was quantified in terms of Bland-Altman plots of the ratio of the measured tissue area fraction to the reference measurement and plotted against the mean value from both measures<sup>117</sup>. These plots were also generated with the original attenuation images to assess impact of incorporating dark-field information.

### 6.3 Results

A qualitative comparison of the original attenuation and dark-field images acquired from the grating interferometer CT scan of the fixed lung along with their combined images are shown in **Figure 6.1**. In the original attenuation image (**Figure 6.1a**) large structures like the esophagus, major bronchi, and large blood vessels are resolvable. However, smaller vessels and airways in the lung parenchyma are blurred out yielding a textured pattern rather than clearly defined structures. The simultaneously acquired dark-field image (**Figure 6.1b**) reveals edge enhancements in the parenchyma exposing these smaller structures as well as highlighting the boundaries around larger structures. In the dark-field enhanced attenuation image (**Figure 6.1c**) the dark-field image is scaled and subtracted from the attenuation according using the empirically determined  $\alpha$  value ( $\alpha = 0.022$ ), yielding a qualitative improvement in resolving smaller structures blurred out in **Figure 6.1a**. In particular, the honeycombing fibrosis pattern is more apparent following enhancement of the attenuation image with dark-field edge information (red arrow in **Figure 6.1c**). Such patterns are important in distinguishing fibrosis from other hyperattenuating pathology such as infiltration. Further edge enhancement is also possible by increasing the relative contribution of dark-field to  $\alpha = 0.1$  (**Figure 6.1d**).

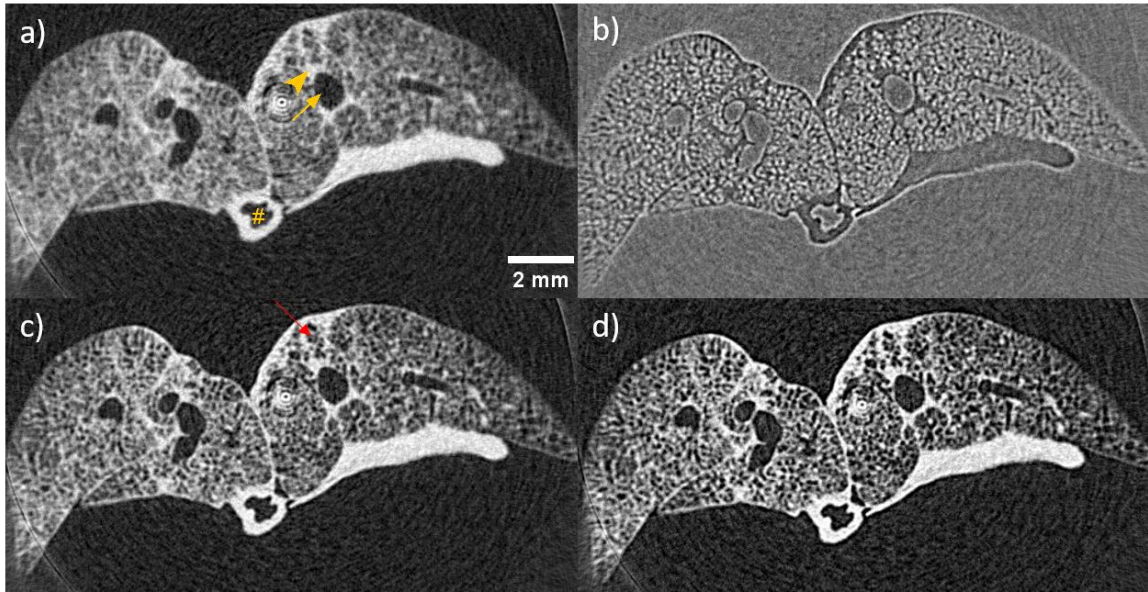


**Figure 6.1** Comparison between attenuation, dark-field, and dark-field enhanced attenuation (DFEA) lung images from a bleomycin mouse model of pulmonary fibrosis. **(a)** Original interferometer attenuation image. Examples of specific anatomy include the esophagus (#), blood vessels (orange arrowhead), and major bronchus (orange arrow). **(b)** original interferometer dark-field image. **(c)** dark-field enhanced attenuation image (DFEA) where the dark-field image (b) is subtracted from the attenuation image (a) after first being scaled by factor  $\alpha = 0.022$ , the measured ratio of water attenuation and phase coefficients. **(d)** increasing this scalar value to  $\alpha = 0.1$  results in a further edge-enhancing effect and further parenchyma contrast enhancement. Image subsets a), c), and d) are all shown at the same display settings of min/max:  $0/0.03 \text{ mm}^{-1}$ , while the dark-field image is shown with display setting min/max:  $-0.1/0.1 \text{ mm}^{-1}$ .

In addition to restoring small features and edges lost to blurring, dark-field enhanced attenuation also increases contrast of large structures like blood vessels and fibrosis. This is due to the abundance of unresolvable features in the lung parenchyma giving an overall positive signal in the dark-field image, while homogenous voxels covering resolvable blood vessels or fibrosis have mean zero signal. Looking at the distribution of pixels via a histogram analysis in **Figure 6.2** shows that following subtraction in dark-field enhanced attenuation, pixels in the parenchyma get shifted to lower values closer to the reference air peak while the restoration of small features and edges yields a small increase in the height of the tissue peak.

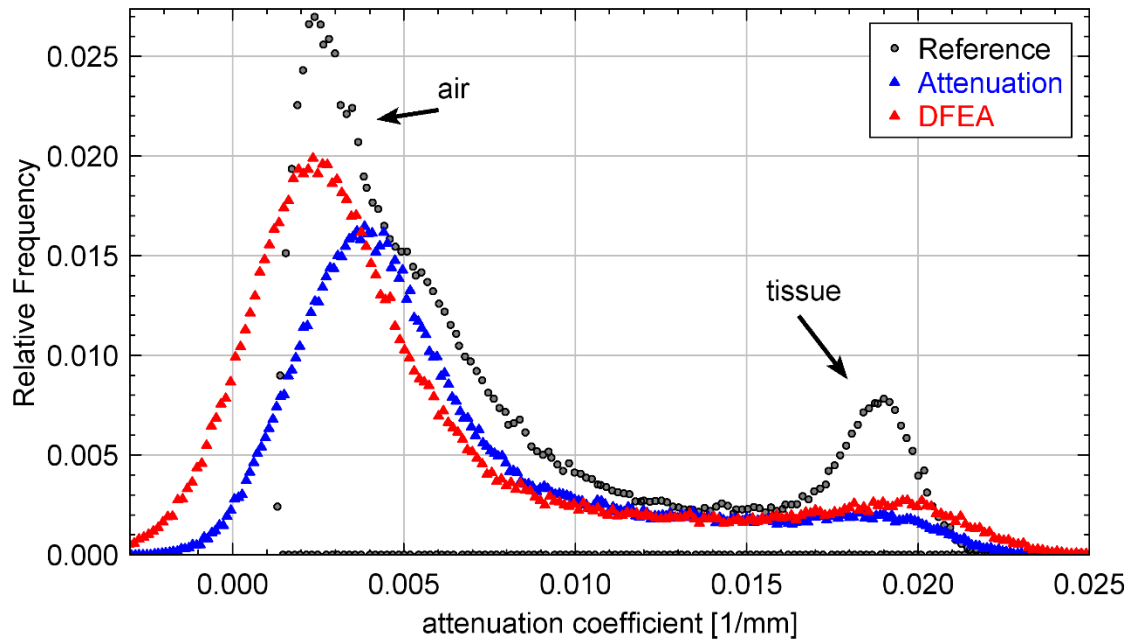


**Figure 6.2** Histogram comparison of attenuation and dark-field enhanced attenuation (DFEA) against a 5  $\mu\text{m}$  voxel high-resolution “Reference” micro-CT scan. Arrow annotations identify the locations of the air and tissue peaks in the bimodal distribution.

This increased histogram separation between the air and tissue peaks from DFEA benefits the histogram-based segmentation of fibrosis as shown in **Figure 6.2**. **Figure 6.3a** shows a representative patch comparing segmentations from the original attenuation, the dark-field enhanced attenuation image, and the co-registered 5  $\mu\text{m}$  reference micro-CT image. **Figure 6.3b** compares the resulting histogram-based segmentations between the image series. The red mask shows the pixels excluded from the analysis which represent healthy tissue anatomy including the heart and esophagus and large airways of the major bronchi. Compared to the original attenuation image the dark-field enhanced image has more small features retained in the segmentation which are visually consistent with the reference scan image.

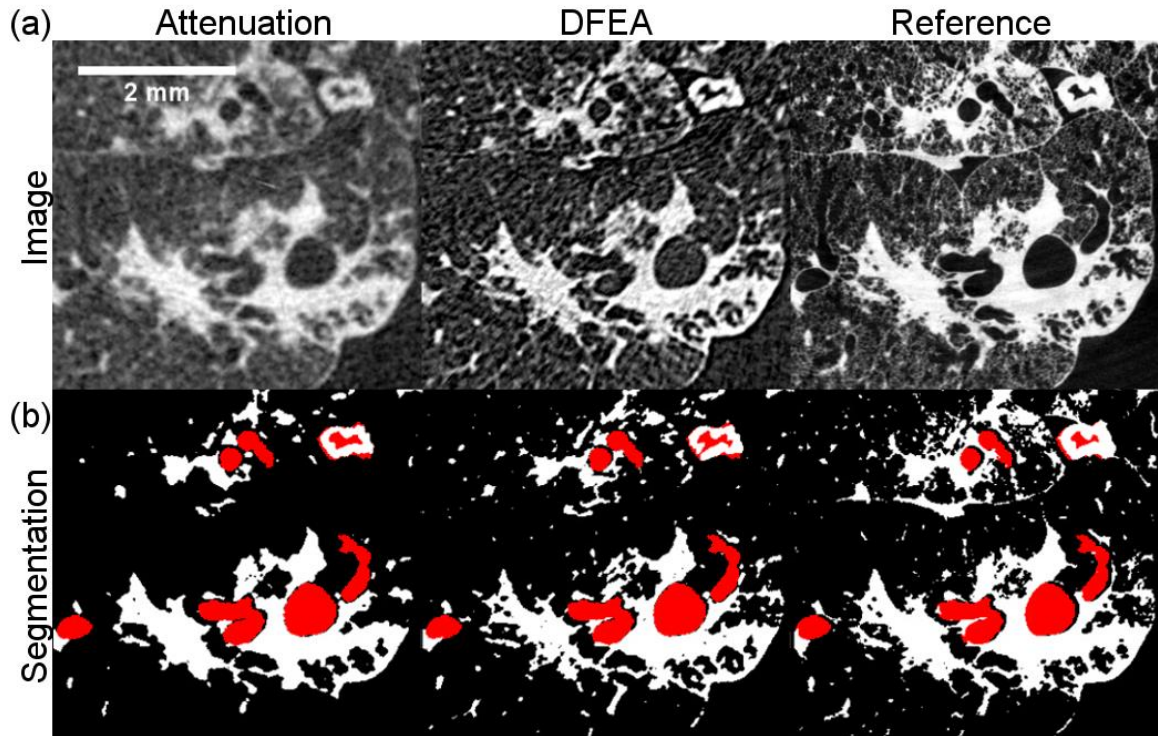


**Figure 6.3** Comparison of intensity-based threshold segmentation between attenuation (left) and dark-field enhanced attenuation (center) against co-registered reference 5  $\mu\text{m}$  voxel micro-CT (right). **Top:** Representative image patches of all three images are shown at the same display settings, min/max: 0/0.03  $\text{mm}^{-1}$ . In this patch reticular fibrosis and honeycombing is present around the large airways. **Bottom:** Threshold-based intensity segmentations with thresholds determined automatically via minimum error thresholding applied to the whole volume histogram. Exclusion mask shown in red.

To quantitatively assess agreement with the 5  $\mu\text{m}$  reference scan all 80 patches were segmented using an intensity threshold determined automatically via minimum error thresholding from the global histogram of each image series. From these segmentations tissue area fraction was measured and presented as a Bland-Altman plot (**Figure 6.4**) where the ratio of the mean tissue area fraction relative to that of the reference measure for each patch is plotted against the mean between both measurements<sup>117</sup>. Using the ratio rather than the absolute difference accounted for a negative proportionality observed in both experimental measurements. This observation was due to the reticular nature of fibrosis and presence of honeycombing in large fibrotic loci of the mouse model where small spindly structures are in greater abundance in higher tissue fraction patches and lost in the segmentation. This transformation corrects for this proportionality and better demonstrates

agreement in lower tissue fraction patches more representative of early-stage fibrotic loci. From this we observed an improved agreement ratio in the dark-field enhanced attenuation (DFEA) images from 0.374 to 0.544 along with a reduction in the 95% limits of agreement describing the measurement spread (summarized in **Table 6.1**).

At higher tissue fractions, representing more severe local fibrosis, we observed the agreement of DFEA to approach that of the original attenuation image. Here the relative influence of restoring small features and edges is less pronounced when fibrotic loci become larger and more solid masses. On the contrary, at lower tissue fractions, more representative of early fibrosis, DFEA images show much improvement over original attenuation images in terms of agreement with reference standard. Both techniques show underestimation of tissue fraction compared to reference standard acquired with 5  $\mu\text{m}$  resolution. However, attenuation images show more proportional dependence on tissue fraction, where there is greater underestimation at lower tissue fractions. On the other hand, DFEA shows less dependence on tissue fraction, with more consistent underestimation (bias). Once measured, this bias could then be corrected for in practice. These results demonstrate improved agreement with the reference 5  $\mu\text{m}$  scan by incorporating dark-field information containing unresolved edge information into attenuation images acquired on a lower resolution 60  $\mu\text{m}$  interferometer scan.

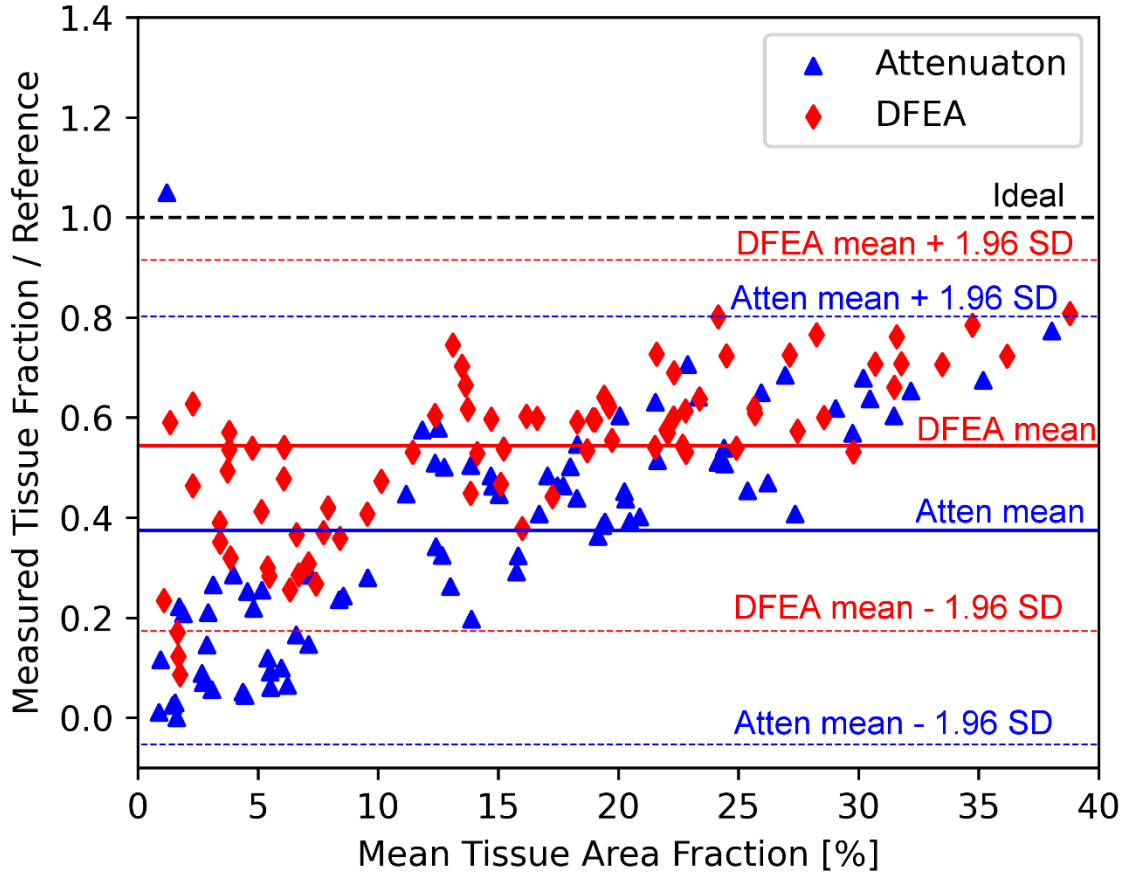


**Figure 6.4** Bland-Altman plot of tissue area fractions measured on a low resolution 60  $\mu\text{m}$  voxel grating interferometer CT system compared to an approximate ground truth high resolution 5  $\mu\text{m}$  voxel reference micro-CT. The contribution of dark-field enhanced attenuation (DFEA) with greater contribution of dark-field information to improve segmentation accuracy in terms of closeness to the reference scan is shown. The thick dashed black line shows an ideal measurement with no bias from the reference measure for an agreement ratio of 1. Red and blue solid lines correspond to the mean agreement ratios, while the corresponding thin dashed lines are the 95% limits of agreement calculated as  $\pm 1.96$  times the standard deviation of the ratios<sup>117</sup>.

**Table 6.1** Summary of Bland-Altman results plotted in Error! Reference source not found.. The agreement ratio is defined as the measured tissue area fraction divided by the reference measurement and the 95% limits of agreement correspond to 1.96 times the standard deviation of the agreement ratios from the measured patches.

Series (x)	Relative to Reference $x/\text{ref}$ [ $\mp 95\%$ ]
<b>Attenuation</b>	0.374 [-0.054 0.802]
<b>DFEA</b>	0.544 [0.173 0.915]

## 6.4 Discussion

High resolution micro-CT is capable of quantifying pulmonary fibrosis extent with greater accuracy and precision than histology or biochemical assays<sup>22</sup>. However, the requirements of long scan times due to x-ray source output limitations and small fields of view due to detector size restrictions limits its applicability to *ex vivo* organ imaging. Meanwhile, the feasibility of x-ray dark-field for *in vivo* whole body CT imaging has already been demonstrated<sup>30,106</sup>. While the quantitative value of using dark-field alone when measured on laboratory-based grating interferometers is limited due to its spatial resolution sensitivity<sup>42</sup>, in this work we presented a means of leveraging dark-field to enhance sharpness and contrast of attenuation images. This method is based on the assumptions of dark-field primarily deriving from intra-pixel phase gradients and on the proportionality between attenuation and phase coefficients in biological tissues at relevant x-ray energies. Using a bleomycin mouse model of pulmonary fibrosis, we showed that this dark-field enhanced attenuation technique was able to restore edges and small features while increasing parenchyma contrast. By using a fixated *ex vivo* lung we were able to reproducibly scan the same specimen to get a ground truth approximation of the lung structure using a high-resolution reference micro-CT to confirm the restoration of small features. Performance in quantifying fibrosis was evaluated against the original interferometer attenuation images in terms of agreement with the reference scan in tissue area fraction measured in 80 randomly sample patches from the lung. Using Bland-Altman plot analysis we found that incorporating the dark-field edge information improved agreement with the high-resolution reference scan in terms of reduced bias and a reduction in spread due to the increased histogram separation between the air and tissue voxel peaks. Determining the acceptable limits of agreement are application specific and are beyond the scope of this work but use of image denoising is one potential means of further decreasing these limits of agreement.

The limitations of this study include the limited sample size and potential registration errors of the reference scan with the interferometer data. During the fixation process some samples did not fully inflate while air-drying and were excluded from the study. Errors in the registration arose from rescanning the lungs on a different scanner where small

deformations could have occurred in the mounting process. While registration was performed automatically and was validated by visual inspection some errors could be present that could account for additional sources of bias when assessing agreement. However, this bias is equivalent for both experimental scans being compared as they derive from the same raw data. Future work remains to increase the sample size by imaging more lung samples and further validate the method with task independent image quality assessment.

Previous works have largely focused on the use of dark-field alone for the detection of lung diseases<sup>23,25,27,29</sup>. However, some studies have leveraged the attenuation information simultaneously acquired in grating interferometer scans, notably normalized scatter where the penetration depth dependence of dark-field radiographs is removed via pixel-wise division with the attenuation image<sup>24,118,119</sup>. This work differs by focusing on how dark-field's correlation with sharp edges and phase gradients in the lung can be used to improve the sharpness and parenchyma contrast in the attenuation image, improving the conspicuity and segmentation performance of small structures with existing detectors and sources.

## **6.5 Conclusions**

Intra-pixel phase gradients are the predominant source of dark-field signal in laboratory-based x-ray grating interferometers. Here we have shown how this gradient information in dark-field images can be used to improve quantifiable characterizations of the lung using dark-field enhanced attenuation (DFEA). An *ex vivo* mouse lung model of pulmonary fibrosis was used to demonstrate the ability of this new technique at improving resolution of small structures and enhancing parenchymal contrast. Improved performance at quantifying fibrosis was demonstrated in terms of improved agreement with a high-resolution reference micro-CT scan.

## **6.6 Accomplishments**

The work described in this specific aim has produced one peer-reviewed journal article:

1. Complementary Use of X-Ray Dark-Field and Attenuation Computed Tomography in Quantifying Pulmonary Fibrosis in a Mouse Model. *Journal of Medical Imaging* (In Preparation)

# CHAPTER 7

---

## Summary and Conclusions

### 7.1 Summary of Research

This thesis addressed two challenges associated with the use of x-ray grating interferometry and x-ray dark-field contrast for small animal lung imaging. First, that the grating optics introduce image artifacts related to beam hardening, and second, that dark-field signal is dependent on the system spatial resolution relative to the size of structures in the imaged sample.

**Chapter 2** introduced the physics behind x-ray attenuation, phase, and dark-field, including the steps involved in their image formation. Phase and dark-field contrasts are accessible through interferometry, which is the use of x-ray interference to measure phase differences in materials. All three contrasts accumulate as line integrals and thus can be reconstructed as cross-sectional images via computed tomography. This chapter also discussed tradeoffs associated with spatial resolution which is often a limiting factor in lung imaging as it reduces sensitivity to small scale structural changes due to attenuation partial volume averaging. These same blurring effects contribute to dark-field signal which motives the central hypothesis of this work that x-ray dark-field and attenuation contrasts can be used in a complementary fashion for lung imaging.

**Chapter 3** described the Talbot-Lau grating interferometer micro-CT imaging system built for small animal *ex vivo* lung imaging and the preprocessing steps involved for **Aim 1** of this thesis. A Talbot-Lau grating interferometer was chosen as it is the most common system for measuring x-ray phase and dark-field contrasts because the grating optics enable use of standard large focal spot x-ray sources and large detectors in a compact geometry.

**Chapter 4** introduced the special challenge of beam hardening associated with using grating optics with standard x-ray sources with broad x-ray spectra. These beam hardening artifacts are spatially heterogenous reflecting varying partial transmission through the

gratings. This chapter introduced an algorithmic correction strategy, Empirical Beam Hardening Correction for Grating Interferometry (EBHC-GI) as a part of thesis **Aim 2** to address these grating-derived beam hardening artifacts. EBHC-GI used the reference attenuation, phase, and visibility signals of the interferometer to encode the spatial heterogeneity of beam hardening in a polynomial correction. In a water phantom, the correction reduced standard deviation from ring artifacts in attenuation CT images by 57% and in dark-field images by 66%. When applied to images of the lungs EBHC-GI was shown to visibly remove ring artifacts.

**Chapter 5** introduced a means for the complementary use of attenuation and dark-field images using a new method called dark-field enhanced attenuation (DFEA) as part of **Aim 3** of the thesis. DFEA subtracts the edge information of dark-field from attenuation to restore edges and improve contrast with unresolved structures. Phantom studies using radial edge spread functions showed that DFEA improved spatial resolution in terms of better approximating the modulation transfer function (MTF) response for an ideal edge at all spatial frequencies measured. ROI measurements in a phantom of different attenuation inserts and non-attenuating inserts with different porosity showed that DFEA maintains quantitative accuracy of attenuation coefficients in large attenuating materials while improving contrast with unresolvable structures. The qualitative impact of these image quality enhancements on imaging lung structure and pathology were then evaluated using an *ex vivo* mouse model pulmonary fibrosis. The model involves administering bleomycin via the trachea and is common in the study of mechanisms and interventions to pulmonary fibrosis. Fixation via tracheal instillation of a formalin and PEG400 solution followed by air inflation enabled repeatable scanning free of respiratory or cardiac motion. Viewing these fixed lungs with DFEA revealed improved definition of small airways and micro-honeycombing in fibrotic loci compared to when viewed with attenuation or dark-field alone.

**Chapter 6** expanded investigations of DFEA for lung imaging with a quantitative assessment on the impact of DFEA for measuring the extent of pulmonary fibrosis to conclude **Aim 3**. Fibrosis extent was defined as the area fraction of soft tissue segmented via automated histogram-based methods. The histogram-based segmentation automatically

selects an attenuation threshold to separate the lung images into air and tissue pixels. Under conditions of insufficient spatial resolution, as observed in the attenuation images, this segmentation approach underestimated the tissue fraction due to partial volume averaging effects that reduce contrast in thin structures to fall beneath this threshold. By restoring blurred edges and enhancing contrast with the unresolved lung parenchyma background, DFEA yielded improved estimates of tissue fractions relative to a dedicated high-resolution micro-CT used as a reference standard. Compared to this high-resolution reference, DFEA images had reduced bias and variance compared to the attenuation images.

## 7.2 Future Research Directions

Future work remains to optimize and further characterize the methods introduced in this thesis to use dark-field and attenuation together in a complementary manner. Images used to generate DFEA were acquired at a single spatial resolution. Later investigations will acquire images with different focal spot sizes, detector pixel sizes, and system geometries of different Talbot order to evaluate their impact on DFEA image quality and on the chosen  $\alpha$  value controlling the relative influence of dark-field.

Furthermore, in this thesis  $\alpha$  in DFEA (**Eq. 5.2**) was chosen empirically based on the ratio measured attenuation and phase values in the material of interest. Further refinements of the approach will optimize the selection of  $\alpha$  through methods such as minimizing the histogram entropy in the lung. Entropy increases when the width of a distribution increases and is inversely related to the performance of the histogram-based segmentation. Thus by selecting  $\alpha$  based on this objective function, DFEA images can be better optimized for fibrosis quantification task.

Other improvements include incorporating a minimum threshold to dark-field images before being subtracted in DFEA to reduce the noise amplification with  $\alpha$  as observed in **Figure 5.6**.

Additionally, further characterization of DFEA with more comprehensive image quality metrics such as noise power spectrum (NPS) and detective quantum efficiency (DQE) are necessary to better assess the tradeoffs associated with using attenuation and dark-field

contrasts together. These tradeoffs include the reduce x-ray dose efficiency of using grating optics which absorb more than half of the output from the x-ray source. This combined with the geometry restrictions associated with grating interferometers to operate at specific Talbot distances (**Eq. 2.7**) means that scan times are that much longer as x-ray intensity diminishes quadratically with distance. Despite the improved spatial resolution and contrast benefits demonstrated by DFEA, further comparisons remain to confirm whether these relative benefits remain in comparison to dedicated micro-CT systems not restricted by grating geometry and dose efficiency limitations.

### **7.3 Conclusions**

X-ray dark-field is a promising technique to access signal from unresolved small structures that is particularly well suited for lung imaging which is spatial resolution limited. This is supported by the continued development of clinical prototypes for human-scale dark-field lung radiography<sup>34,120,121</sup> and CT<sup>36</sup>. However, given the importance of quantitative measurements in attenuation CT characterization of lung diseases<sup>47,110</sup>, it is necessary to also understand and account for any sources of bias and artifact in dark-field images. The work presented in this thesis addressed specific challenges associated with using x-ray dark-field quantitatively which include beam hardening from the interferometer gratings and the dependence on dark-field signal magnitude to system spatial resolution relative to the size of the imaged object.

The results presented in this thesis were found to support the central hypothesis that x-ray dark-field and attenuation information can be used together synergistically to leverage the strength of each contrast. Key to this is that the blurring processes that reduce contrast in attenuation images of the lungs contribute to the dark-field signal. While dark-field is particularly sensitive to unresolved edges, it is of limited quantitative value as dark-field signal magnitude is not constant for a given sample but can change with a different point spread function affecting spatial resolution<sup>41,42</sup>. However, by scaling and subtracting the dark-field image from simultaneously acquired attenuation image we observed an improvement in spatial resolution and enhancement in contrast with unresolved structures

as demonstrated by both qualitative and quantitative assessments in phantoms and fixed lung samples.

## 7.4 Accomplishments

The work described in this thesis has produced two journal articles (including those under review and in preparation), two conference proceedings, four conference abstracts and presentations, and one student award which have been listed in the accomplishments sections in chapters 4-6.

Work not directly related to this thesis work but that I authored or contributed in my Ph.D. training include five peer-reviewed journals, one conference proceedings, and five conference abstracts listed in the following sections.

### 7.4.1 Peer-Reviewed Journal Papers

Peer-reviewed papers that I authored or co-authored not directly related to this thesis are listed below

1. **Nelson BJ**, Gomez-Cardona D, Michalak GJ, et al. Multiple kernel synthesis of head CT using a convolutional neural network with a task-based loss function. *Medical Physics* (Under review).
2. Inoue A, Diehn FE, Nagelschneider AA, Passe, Theodore J., DeLone, David R., **Nelson, BJ**, et al. The feasibility of replacing multi-series conventional head CT images with a single series of thin-slice, low-noise images created using a multi-kernel synthesis method. *American Journal of Neuroradiology* (Under review).
3. Sung Y, **Nelson BJ**, Shanblatt ER, Gupta R, McCollough CH, Graves WS. Wave optics simulation of grating-based X-ray phase-contrast imaging using 4D Mouse Whole Body (MOBY) phantom. *Medical Physics*. 2020;47(11):5761-5771. doi:<https://doi.org/10.1002/mp.14479>
4. Shanblatt ER, Sung Y, Gupta R, **Nelson BJ**, et al. Forward model for propagation-based x-ray phase contrast imaging in parallel- and cone-beam geometry. *Opt Express*, OE. 2019;27(4):4504-4521. doi:10.1364/OE.27.004504

5. Sung Y, Gupta R, **Nelson BJ**, Leng S, McCollough CH, Graves WS. Phase-contrast imaging with a compact x-ray light source: system design. *JMI*. 2017;4(4):043503. doi:10.1117/1.JMI.4.4.043503

#### **7.4.2 Conference Proceedings**

Below are listed conference proceedings and presentations that I contributed to that are not directly related this thesis work

1. Shanblatt ER, **Nelson BJ**, Tao S, Leng S, McCollough CH. Demonstration of phase-assisted material decomposition with a Talbot-Lau interferometer using a single x-ray tube potential. In: *Medical Imaging 2019: Physics of Medical Imaging*. Vol 10948. International Society for Optics and Photonics; 2019:109482W. doi:[10.1117/12.2511806](https://doi.org/10.1117/12.2511806)

#### **7.4.3 Conference Abstracts**

Below are listed conference abstracts and presentations that I authored that are not directly related this thesis work

1. Oral Presentation, “Task-Based Loss Function for Convolutional Neural Network Image Denoising”, AAPM 2021 Virtual July 12-16, 2020
2. Poster Presentation, “CNR Dependence on Spatial Resolution and Subject Contrast in Phase Contrast CT”, Joint AAPM/COMP Meeting, Vancouver, BC (virtual) Feb. 16-21, 2019
3. Poster Presentation, “Visibility Guided Phase Contrast Denoising”, SPIE Medical Imaging Conference 2019, San Diego, CA Oct. 17-29, 2018
4. Poster Presentation, “Methods for Generating and Viewing CT Images Containing Multiple Kernels, Slice Thicknesses, and Display Settings”, Biomedical Engineering Society, Atlanta, GA May 20-23, 2018
5. Poster Presentation, “Simulation of a Propagation-Based Phase-Contrast Imaging system with a compact x-ray light source”, International Conference on Image Formation in X-ray Computed Tomography, Salt Lake City, Utah

# REFERENCES

---

1. Raghu G, Collard HR, Egan JJ, et al. An Official ATS/ERS/JRS/ALAT Statement: Idiopathic Pulmonary Fibrosis: Evidence-based Guidelines for Diagnosis and Management. *Am J Respir Crit Care Med*. 2011;183(6):788-824. doi:10.1164/rccm.2009-040GL
2. Kim HJ, Perlman D, Tomic R. Natural history of idiopathic pulmonary fibrosis. *Respir Med*. 2015;109(6):661-670. doi:10.1016/j.rmed.2015.02.002
3. Demedts M, Wells AU, Anto JM, et al. Interstitial lung diseases: an epidemiological overview. :15.
4. Martinez FJ, Collard HR, Pardo A, et al. Idiopathic pulmonary fibrosis. *Nat Rev Dis Primer*. 2017;3(1):1-19. doi:10.1038/nrdp.2017.74
5. Hansell DM, Bankier AA, MacMahon H, McLoud TC, Müller NL, Remy J. Fleischner Society: Glossary of Terms for Thoracic Imaging. *Radiology*. 2008;246(3):697-722. doi:10.1148/radiol.2462070712
6. Iwasawa T, Asakura A, Sakai F, et al. Assessment of Prognosis of Patients With Idiopathic Pulmonary Fibrosis by Computer-aided Analysis of CT Images. *J Thorac Imaging*. 2009;24(3):216-222. doi:10.1097/RTI.0b013e3181a6527d
7. Jacob J, Bartholmai BJ, Rajagopalan S, et al. Automated Quantitative Computed Tomography Versus Visual Computed Tomography Scoring in Idiopathic Pulmonary Fibrosis: Validation Against Pulmonary Function. *J Thorac Imaging*. 2016;31(5):304-311. doi:10.1097/RTI.0000000000000220
8. Hutchinson JP, Fogarty AW, McKeever TM, Hubbard RB. In-hospital mortality following surgical lung biopsy for interstitial lung disease in the USA: 2000-2011. *Am J Respir Crit Care Med*. 2015;193(10). doi:10.1164/rccm.201508-1632OC
9. Chung JH, Goldin JG. Interpretation of HRCT Scans in the Diagnosis of IPF: Improving Communication Between Pulmonologists and Radiologists. *Lung*. 2018;196(5):561-567. doi:10.1007/s00408-018-0143-5
10. Hoffman EA, Reinhardt JM, Sonka M, et al. Characterization of the interstitial lung diseases via density-based and texture-based analysis of computed tomography images of lung structure and function1. *Acad Radiol*. 2003;10(10):1104-1118. doi:10.1016/S1076-6332(03)00330-1
11. Xu Y, van Beek EJR, Hwanjo Y, Guo J, McLennan G, Hoffman EA. Computer-aided Classification of Interstitial Lung Diseases Via MDCT: 3D Adaptive Multiple Feature Method (3D AMFM). *Acad Radiol*. 2006;13(8):969-978. doi:10.1016/j.acra.2006.04.017
12. Wells AU, Kokosi MA. Subclinical Interstitial Lung Abnormalities: Toward the Early Detection of Idiopathic Pulmonary Fibrosis? *Am J Respir Crit Care Med*. 2016;194(12):1445-1446. doi:10.1164/rccm.201607-1363ED

13. Bartlett DJ, Koo CW, Bartholmai BJ, et al. High-Resolution Chest Computed Tomography Imaging of the Lungs: Impact of 1024 Matrix Reconstruction and Photon-Counting Detector Computed Tomography. *Invest Radiol.* 2019;54(3):129-137. doi:10.1097/RLI.0000000000000524
14. Inoue A. Impact of photon-counting CT on reader confidence in diagnosis of usual interstitial pneumonia. Oral presented at: Radiological Society of North America; November 28, 2021; Chicago.
15. Webb WR. Thin-Section CT of the Secondary Pulmonary Lobule: Anatomy and the Image—The 2004 Fleischner Lecture. *Radiology.* 2006;239(2):322-338. doi:10.1148/radiol.2392041968
16. Ritman EL. Micro-Computed Tomography of the Lungs and Pulmonary-Vascular System. *Proc Am Thorac Soc.* 2005;2(6):477-480. doi:10.1513/pats.200508-080DS
17. Pfeiffer F, Weitkamp T, Bunk O, David C. Phase retrieval and differential phase-contrast imaging with low-brilliance X-ray sources. *Nat Phys.* 2006;2(4):258-261. doi:10.1038/nphys265
18. Pfeiffer F, Bech M, Bunk O, et al. Hard-X-ray dark-field imaging using a grating interferometer. *Nat Mater.* 2008;7(2):134-137. doi:10.1038/nmat2096
19. Michel T, Rieger J, Anton G, et al. On a dark-field signal generated by micrometer-sized calcifications in phase-contrast mammography. *Phys Med Biol.* 2013;58(8):2713-2732. doi:10.1088/0031-9155/58/8/2713
20. Ritman EL. Small-animal CT - Its Difference from, and Impact on, Clinical CT. *Nucl Instrum Methods Phys Res Sect Accel Spectrometers Detect Assoc Equip.* 2007;580(2):968-970. doi:10.1016/j.nima.2007.06.040
21. Cavanaugh D, Travis EL, Price RE, et al. Quantification of Bleomycin-Induced Murine Lung Damage In Vivo With Micro-Computed Tomography. *Acad Radiol.* 2006;13(12):1505-1512. doi:10.1016/j.acra.2006.08.011
22. Scotton CJ, Hayes B, Alexander R, et al. Ex vivo micro-computed tomography analysis of bleomycin-induced lung fibrosis for preclinical drug evaluation. *Eur Respir J.* 2013;42(6):1633-1645. doi:10.1183/09031936.00182412
23. Meinel FG, Schwab F, Schleede S, et al. Diagnosing and Mapping Pulmonary Emphysema on X-Ray Projection Images: Incremental Value of Grating-Based X-Ray Dark-Field Imaging. *PLOS ONE.* 2013;8(3):e59526. doi:10.1371/journal.pone.0059526
24. Meinel FG, Yaroshenko A, Hellbach K, et al. Improved Diagnosis of Pulmonary Emphysema Using In Vivo Dark-Field Radiography. *Invest Radiol.* 2014;49(10):653-658. doi:10.1097/RLI.0000000000000067
25. Hellbach K, Yaroshenko A, Meinel FG, et al. In Vivo Dark-Field Radiography for Early Diagnosis and Staging of Pulmonary Emphysema. *Invest Radiol.* 2015;50(7):430-435. doi:10.1097/RLI.0000000000000147
26. Hellbach K, Meinel FG, Conlon TM, et al. X-Ray Dark-field Imaging to Depict Acute Lung Inflammation in Mice. *Sci Rep.* 2018;8(1):2096. doi:10.1038/s41598-018-20193-8

27. Hellbach K, Yaroshenko A, Willer K, et al. Facilitated Diagnosis of Pneumothoraces in Newborn Mice Using X-ray Dark-Field Radiography. *Invest Radiol.* 2016;51(10):597-601. doi:10.1097/RLI.0000000000000285
28. Scherer K, Yaroshenko A, Bölükbas DA, et al. X-ray Dark-field Radiography - In-Vivo Diagnosis of Lung Cancer in Mice. *Sci Rep.* 2017;7(1):402. doi:10.1038/s41598-017-00489-x
29. Yaroshenko A, Hellbach K, Yildirim AÖ, et al. Improved In vivo Assessment of Pulmonary Fibrosis in Mice using X-Ray Dark-Field Radiography. *Sci Rep.* 2015;5:17492. doi:10.1038/srep17492
30. Velroyen A, Yaroshenko A, Hahn D, et al. Grating-based X-ray Dark-field Computed Tomography of Living Mice. *EBioMedicine.* 2015;2(10):1500-1506. doi:10.1016/j.ebiom.2015.08.014
31. Tapfer A, Bech M, Pauwels B, et al. Development of a prototype gantry system for preclinical x-ray phase-contrast computed tomography. *Med Phys.* 2011;38(11):5910-5915. doi:https://doi.org/10.1118/1.3644844
32. Tapfer A, Bech M, Velroyen A, et al. Experimental results from a preclinical X-ray phase-contrast CT scanner. *Proc Natl Acad Sci.* 2012;109(39):15691-15696. doi:10.1073/pnas.1207503109
33. Umkehrer S, Birnbacher L, Burkhardt R, et al. Optimization of in vivo murine X-ray dark-field computed tomography. *Rev Sci Instrum.* 2019;90(10):103103. doi:10.1063/1.5115436
34. Willer K, Fingerle AA, Noichl W, et al. X-ray dark-field chest imaging for detection and quantification of emphysema in patients with chronic obstructive pulmonary disease: a diagnostic accuracy study. *Lancet Digit Health.* 2021;3(11):e733-e744. doi:10.1016/S2589-7500(21)00146-1
35. Gromann LB, De Marco F, Willer K, et al. In-vivo X-ray Dark-Field Chest Radiography of a Pig. *Sci Rep.* 2017;7(1):4807. doi:10.1038/s41598-017-05101-w
36. Viermetz M, Gustschin N, Schmid C, et al. Dark-field computed tomography reaches the human scale. *Proc Natl Acad Sci.* 2022;119(8). doi:10.1073/pnas.2118799119
37. Lynch SK, Pai V, Auxier J, et al. Interpretation of dark-field contrast and particle-size selectivity in grating interferometers. Published online 2012:20.
38. Chabior M, Donath T, David C, et al. Beam hardening effects in grating-based x-ray phase-contrast imaging. *Med Phys.* 2011;38(3):1189-1195. doi:https://doi.org/10.1118/1.3553408
39. Engelhardt M, Kottler C, Bunk O, et al. The fractional Talbot effect in differential x-ray phase-contrast imaging for extended and polychromatic x-ray sources. *J Microsc.* 2008;232(1):145-157. doi:https://doi.org/10.1111/j.1365-2818.2008.02072.x
40. Yashiro W, Vagovič P, Momose A. Effect of beam hardening on a visibility-contrast image obtained by X-ray grating interferometry. *Opt Express.* 2015;23(18):23462-23471. doi:10.1364/OE.23.023462
41. Yashiro W, Momose A. Effects of unresolvable edges in grating-based X-ray differential phase imaging. *Opt Express.* 2015;23(7):9233. doi:10.1364/OE.23.009233

42. Koenig T, Zuber M, Trimborn B, et al. On the origin and nature of the grating interferometric dark-field contrast obtained with low-brilliance x-ray sources. *Phys Med Biol.* 2016;61(9):3427-3442. doi:10.1088/0031-9155/61/9/3427
43. Schleede S, Meinel FG, Bech M, et al. Emphysema diagnosis using X-ray dark-field imaging at a laser-driven compact synchrotron light source. *Proc Natl Acad Sci.* 2012;109(44):17880-17885. doi:10.1073/pnas.1206684109
44. Bravin A, Coan P, Suortti P. X-ray phase-contrast imaging: from pre-clinical applications towards clinics. *Phys Med Biol.* 2013;58(1):R1-R35. doi:10.1088/0031-9155/58/1/R1
45. Gotway MB, Reddy GP, Webb WR, Elicker BM, Leung JWT. High-Resolution CT of the Lung: Patterns of Disease and Differential Diagnoses. *Radiol Clin North Am.* 2005;43(3):513-542. doi:10.1016/j.rcl.2005.01.010
46. Walsh S, Hansell D. High-Resolution CT of Interstitial Lung Disease: A Continuous Evolution. *Semin Respir Crit Care Med.* 2014;35(01):129-144. doi:10.1055/s-0033-1363458
47. Mascalchi M, Camiciottoli G, Diciotti S. Lung densitometry: why, how and when. *J Thorac Dis.* 2017;9(9). doi:10.21037/jtd.2017.08.17
48. Graetz J, Balles A, Hanke R, Zabler S. Review and experimental verification of x-ray dark-field signal interpretations with respect to quantitative isotropic and anisotropic dark-field computed tomography. *Phys Med Biol.* 2020;65(23):235017. doi:10.1088/1361-6560/abb7c6
49. Punnoose J, Xu J, Sisniega A, Zbijewski W, Siewerdsen JH. Technical Note: spektr 3.0-A computational tool for x-ray spectrum modeling and analysis. *Med Phys.* 2016;43(8):4711. doi:10.1118/1.4955438
50. Hecht E. *Optics*. 5th edition. Pearson; 2015. <https://drive.google.com/file/d/1GylU-UXQkAdC4O6bU6rlcBJkh9xgbexN/view?usp=sharing>
51. Hsieh J. *Computed Tomography: Principles, Design, Artifacts, and Recent Advances*. 3rd edition. Society of Photo Optical; 2015. <https://drive.google.com/file/d/1Po4EdqtnPhFDMo4hjhnok3wljka9tu2g/view?usp=sharing>
52. Momose A. X-ray phase imaging reaching clinical uses. *Phys Med.* 2020;79:93-102. doi:10.1016/j.ejmp.2020.11.003
53. Attwood D, Sakdinawat A. *X-Rays and Extreme Ultraviolet Radiation: Principles and Applications*. Cambridge Core. doi:10.1017/CBO9781107477629
54. NIST X-Ray Form Factor, Atten. Scatt. Tables Form Page. Accessed January 26, 2022. <https://physics.nist.gov/PhysRefData/FFast/html/form.html>
55. CXRO X-Ray Interactions With Matter. Accessed January 25, 2022. [https://henke.lbl.gov/optical\\_constants/](https://henke.lbl.gov/optical_constants/)
56. Weitkamp T, Diaz A, David C, et al. X-ray phase imaging with a grating interferometer. *Opt Express.* 2005;13(16):6296-6304. doi:10.1364/opex.13.006296
57. Talbot H Fox. Facts relating to optical science. *Philos Mag.* No. IV(9).

58. Wang ZT, Kang KJ, Huang ZF, Chen ZQ. Quantitative grating-based x-ray dark-field computed tomography. *Appl Phys Lett*. 2009;95(9):094105. doi:10.1063/1.3213557
59. Gao PF, Lei G, Huang CZ. Dark-Field Microscopy: Recent Advances in Accurate Analysis and Emerging Applications. *Anal Chem*. 2021;93(11):4707-4726. doi:10.1021/acs.analchem.0c04390
60. Strobl M. General solution for quantitative dark-field contrast imaging with grating interferometers. *ArXiv13120473 Cond-Mat*. Published online December 2, 2013. Accessed June 4, 2021. <http://arxiv.org/abs/1312.0473>
61. Bech M, Bunk O, Donath T, Feidenhans'l R, David C, Pfeiffer F. Quantitative x-ray dark-field computed tomography. *Phys Med Biol*. 2010;55(18):5529-5539. doi:10.1088/0031-9155/55/18/017
62. Chen GH, Bevins N, Zambelli J, Qi Z. Small-angle scattering computed tomography (SAS-CT) using a Talbot-Lau interferometer and a rotating anode x-ray tube: theory and experiments. *Opt Express*. 2010;18(12):12960-12970. doi:10.1364/OE.18.012960
63. Grimmer R, Fahrig R, Hinshaw W, Gao H, Kachelriess M. Empirical cupping correction for CT scanners with primary modulation (ECCP). *Med Phys*. 2012;39(2):825-831. doi:10.1118/1.3676180
64. Glover GH, Pelc NJ. Nonlinear partial volume artifacts in x-ray computed tomography. *Med Phys*. 1980;7(3):238-248. doi:10.1118/1.594678
65. Langhe ED, Velde GV, Hostens J, et al. Quantification of Lung Fibrosis and Emphysema in Mice Using Automated Micro-Computed Tomography. *PLOS ONE*. 2012;7(8):e43123. doi:10.1371/journal.pone.0043123
66. Yang Y, Tang X. The second-order differential phase contrast and its retrieval for imaging with x-ray Talbot interferometry. *Med Phys*. 2012;39(12):7237-7253. doi:10.1118/1.4764901
67. Yashiro W, Noda D, Kajiwara K. Effect of insufficient temporal coherence on visibility contrast in X-ray grating interferometry. *Opt Express*. 2018;26(2):1012-1027. doi:10.1364/OE.26.001012
68. Bech M. X-ray imaging with a grating interferometer.
69. Mohr J, Grund T, Kunka D, et al. High aspect ratio gratings for X-ray phase contrast imaging. *AIP Conf Proc*. 2012;1466(1):41-50. doi:10.1063/1.4742267
70. Kafri O, Glatt I. *The Physics of Moire Metrology*. 1st edition. Wiley-Interscience; 1990.
71. Teuffenbach M von, Koehler T, Fehringer A, et al. Grating-based phase-contrast and dark-field computed tomography: a single-shot method. *Sci Rep*. 2017;7(1):7476. doi:10.1038/s41598-017-06729-4
72. Köhler T, Engel KJ, Roessl E. Noise properties of grating-based x-ray phase contrast computed tomography. *Med Phys*. 2011;38(S1):S106-S116. doi:<https://doi.org/10.1118/1.3532396>

73. Chen GH, Zambelli J, Li K, Bevins N, Qi Z. Scaling law for noise variance and spatial resolution in differential phase contrast computed tomography. *Med Phys.* 2011;38(2):584-588. doi:https://doi.org/10.1118/1.3533718
74. Trimborn B, Meyer P, Kunka D, et al. Imaging properties of high aspect ratio absorption gratings for use in preclinical x-ray grating interferometry. *Phys Med Biol.* 2016;61(2):527-541. doi:10.1088/0031-9155/61/2/527
75. Hsieh J, Gurmen OE, King KF. Investigation of a solid-state detector for advanced computed tomography. *IEEE Trans Med Imaging.* 2000;19(9):930-940. doi:10.1109/42.887840
76. Feldkamp LA, Davis LC, Kress JW. Practical cone-beam algorithm. *JOSA A.* 1984;1(6):612-619. doi:10.1364/JOSAA.1.000612
77. Biguri A, Dosanjh M, Hancock S, Soleimani M. TIGRE: a MATLAB-GPU toolbox for CBCT image reconstruction. *Biomed Phys Eng Express.* 2016;2(5):055010. doi:10.1088/2057-1976/2/5/055010
78. Thüring T, Modregger P, Pinzer BR, Wang Z, Stampanoni M. Non-linear regularized phase retrieval for unidirectional X-ray differential phase contrast radiography. *Opt Express.* 2011;19(25):25545-25558. doi:10.1364/OE.19.025545
79. Glover GH, Pelc NJ. An algorithm for the reduction of metal clip artifacts in CT reconstructions. *Med Phys.* 1981;8(6):799-807. doi:10.1118/1.595032
80. Brooks RA, Di Chiro G. Beam hardening in x-ray reconstructive tomography. *Phys Med Biol.* 1976;21(3):390-398. doi:10.1088/0031-9155/21/3/004
81. Pelzer G, Anton G, Horn F, et al. A beam hardening and dispersion correction for x-ray dark-field radiography. *Med Phys.* 2016;43(6):2774-2779. doi:10.1118/1.4948671
82. Munro PRT, Olivo A. X-ray phase-contrast imaging with polychromatic sources and the concept of effective energy. *Phys Rev A.* 2013;87(5):053838. doi:10.1103/PhysRevA.87.053838
83. Gao H, Zhang L, Grimmer R, Fahrig R. Physics-based spectral compensation algorithm for x-ray CT with primary modulator. *Phys Med Biol.* 2019;64(12):125006. doi:10.1088/1361-6560/ab1ad0
84. Yan A, Wu X, Liu H. Beam hardening correction in polychromatic x-ray grating interferometry. *Opt Express.* 2017;25(20):24690-24704. doi:10.1364/OE.25.024690
85. Kachelriess M, Sourbelle K, Kalender WA. Empirical cupping correction: a first-order raw data pre-correction for cone-beam computed tomography. *Med Phys.* 2006;33(5):1269-1274. doi:10.1118/1.2188076
86. Otsu N. A Threshold Selection Method from Gray-Level Histograms. *IEEE Trans Syst Man Cybern.* 1979;9(1):62-66. doi:10.1109/TSMC.1979.4310076
87. Langner O, Karolczak M, Rattmann G, Kalender WA. Bar and Point Test Patterns Generated by Dry-Etching for Measurement of High Spatial Resolution in Micro-CT. In: Dössel O, Schlegel WC, eds. *World Congress on Medical Physics and Biomedical Engineering, September 7 - 12, 2009, Munich, Germany.* IFMBE Proceedings. Springer; 2009:428-431. doi:10.1007/978-3-642-03879-2\_121

88. Hsieh J, Molthen RC, Dawson CA, Johnson RH. An iterative approach to the beam hardening correction in cone beam CT. *Med Phys.* 2000;27(1):23-29. doi:10.1118/1.598853
89. Joseph PM, Spital RD. A method for correcting bone induced artifacts in computed tomography scanners. *J Comput Assist Tomogr.* 1978;2(1):100-108. doi:10.1097/00004728-197801000-00017
90. Luo S, Wu H, Sun Y, Li J, Li G, Gu N. A fast beam hardening correction method incorporated in a filtered back-projection based MAP algorithm. *Phys Med Biol.* 2017;62(5):1810-1830. doi:10.1088/1361-6560/aa56b5
91. Münch B, Trtik P, Marone F, Stampanoni M. Stripe and ring artifact removal with combined wavelet--Fourier filtering. *Opt Express.* 2009;17(10):8567-8591. doi:10.1364/oe.17.008567
92. Hauke C, Bartl P, Leghissa M, et al. A preclinical Talbot-Lau prototype for x-ray dark-field imaging of human-sized objects. *Med Phys.* 2018;45(6):2565-2571. doi:10.1002/mp.12889
93. Horn F, Leghissa M, Kaeppler S, et al. Implementation of a Talbot-Lau interferometer in a clinical-like c-arm setup: A feasibility study. *Sci Rep.* 2018;8(1):2325. doi:10.1038/s41598-018-19482-z
94. Wang Z, Hauser N, Kubik-Huch RA, D'Isidoro F, Stampanoni M. Quantitative volumetric breast density estimation using phase contrast mammography. *Phys Med Biol.* 2015;60(10):4123-4135. doi:10.1088/0031-9155/60/10/4123
95. Armstrong JD, Sorenson JA, Nelson JA, et al. Clinical evaluation of unsharp masking and slit scanning techniques in chest radiography. *Radiology.* 1983;147(2):351-356. doi:10.1148/radiology.147.2.6340155
96. Schaefer CM, Greene R, Llewellyn HJ, et al. Interstitial lung disease: impact of postprocessing in digital storage phosphor imaging. *Radiology.* 1991;178(3):733-738. doi:10.1148/radiology.178.3.1994410
97. Sorenson JA, Niklason LT, Nelson JA. Photographic unsharp masking in chest radiography. *Invest Radiol.* 1981;16(4):281-288. doi:10.1097/00004424-198107000-00007
98. Sperl JI, Bequé D, Kudielka GP, Mahdi K, Edic PM, Cozzini C. A Fourier-domain algorithm for total-variation regularized phase retrieval in differential X-ray phase contrast imaging. *Opt Express.* 2014;22(1):450-462. doi:10.1364/OE.22.000450
99. Bech M, Jensen TH, Feidenhans'l R, Bunk O, David C, Pfeiffer F. Soft-tissue phase-contrast tomography with an x-ray tube source. *Phys Med Biol.* 2009;54(9):2747-2753. doi:10.1088/0031-9155/54/9/010
100. Haas W, Bech M, Bartl P, et al. Phase-unwrapping of differential phase-contrast data using attenuation information. In: *Medical Imaging 2011: Image Processing.* Vol 7962. International Society for Optics and Photonics; 2011:79624R. doi:10.1117/12.877945

101. Epple FM, Potdevin G, Thibault P, et al. Unwrapping differential x-ray phase-contrast images through phase estimation from multiple energy data. *Opt Express*. 2013;21(24):29101-29108. doi:10.1364/OE.21.029101
102. Richard S, Husarik DB, Yadava G, Murphy SN, Samei E. Towards task-based assessment of CT performance: system and object MTF across different reconstruction algorithms. *Med Phys*. 2012;39(7):4115-4122. doi:10.1118/1.4725171
103. Knust J, Ochs M, Gundersen HJG, Nyengaard JR. Stereological estimates of alveolar number and size and capillary length and surface area in mice lungs. *Anat Rec Hoboken NJ* 2007. 2009;292(1):113-122. doi:10.1002/ar.20747
104. Jenkins RG, Moore BB, Chambers RC, et al. An Official American Thoracic Society Workshop Report: Use of Animal Models for the Preclinical Assessment of Potential Therapies for Pulmonary Fibrosis. *Am J Respir Cell Mol Biol*. 2017;56(5):667-679. doi:10.1165/rcmb.2017-0096ST
105. Vasilescu DM, Gao Z, Saha PK, et al. Assessment of morphometry of pulmonary acini in mouse lungs by nondestructive imaging using multiscale microcomputed tomography. *Proc Natl Acad Sci*. 2012;109(42):17105-17110. doi:10.1073/pnas.1215112109
106. Burkhardt R, Gora T, Fingerle AA, et al. In-vivo X-ray dark-field computed tomography for the detection of radiation-induced lung damage in mice. *Phys Imaging Radiat Oncol*. 2021;20:11-16. doi:10.1016/j.phro.2021.09.003
107. Yu D, Qu W, Xia H, et al. Comparison of the gas-liquid dual support fixation and Heitzman fixation techniques for preparing lung specimens. *Exp Ther Med*. 2017;14(1):825-830. doi:10.3892/etm.2017.4563
108. Hsia CCW, Hyde DM, Ochs M, Weibel ER. An Official Research Policy Statement of the American Thoracic Society/European Respiratory Society: Standards for Quantitative Assessment of Lung Structure. *Am J Respir Crit Care Med*. 2010;181(4):394-418. doi:10.1164/rccm.200809-1522ST
109. Jabri KN, Wilson DL. Quantitative assessment of image quality enhancement due to unsharp-mask processing in x-ray fluoroscopy. *J Opt Soc Am A Opt Image Sci Vis*. 2002;19(7):1297-1307. doi:10.1364/josaa.19.001297
110. Bartholmai BJ, Raghunath S, Karwoski RA, et al. Quantitative Computed Tomography Imaging of Interstitial Lung Diseases. *J Thorac Imaging*. 2013;28(5):298-307. doi:10.1097/RTI.0b013e3182a21969
111. Burkhardt R, Gora T, Fingerle AA, et al. Early detection of radiation-induced lung damage with X-ray dark-field radiography in mice. *Eur Radiol*. 2021;31(6):4175-4183. doi:10.1007/s00330-020-07459-4
112. Ochs M. A brief update on lung stereology. *J Microsc*. 2006;222(3):188-200. doi:https://doi.org/10.1111/j.1365-2818.2006.01587.x
113. Scotton CJ, Chambers RC. Bleomycin revisited: towards a more representative model of IPF? *Am J Physiol-Lung Cell Mol Physiol*. 2010;299(4):L439-L441. doi:10.1152/ajplung.00258.2010
114. ImageJ. Accessed January 12, 2022. <https://imagej.nih.gov/ij/>

115. Kittler J, Illingworth J. Minimum error thresholding. *Pattern Recognit.* 1986;19(1):41-47. doi:10.1016/0031-3203(86)90030-0
116. Expert Automated Registration — 3D Slicer documentation. Accessed August 23, 2021.  
[https://slicer.readthedocs.io/en/latest/user\\_guide/modules/expertautomatedregistration.html](https://slicer.readthedocs.io/en/latest/user_guide/modules/expertautomatedregistration.html)
117. Bland JM, Altman DG. Measuring agreement in method comparison studies. *Stat Methods Med Res.* 1999;8(2):135-160. doi:10.1177/096228029900800204
118. Ludwig V, Seifert M, Hauke C, et al. Exploration of different x-ray Talbot–Lau setups for dark-field lung imaging examined in a porcine lung. *Phys Med Biol.* 2019;64(6):065013. doi:10.1088/1361-6560/ab051c
119. Wang Z, Stampanoni M. Quantitative x-ray radiography using grating interferometry: a feasibility study. *Phys Med Biol.* 2013;58(19):6815-6826. doi:10.1088/0031-9155/58/19/6815
120. Gassert FT, Urban T, Frank M, et al. X-ray Dark-Field Chest Imaging: Qualitative and Quantitative Results in Healthy Humans. 2021;000(0):7.
121. Zimmermann GS, Fingerle AA, Renger B, et al. Dark-field chest x-ray imaging: first experience in patients with alpha1-antitrypsin deficiency. *Eur Radiol Exp.* 2022;6(1):9. doi:10.1186/s41747-022-00263-3